# IMPROVEMENTS TO THE CALCULATION OF INDIRECT SIGNALS OF DIFFUSE GAMMA-RAYS AND NEUTRINOS FROM DARK MATTER ANNIHILATION

A Dissertation

by

SHELDON SCOTT CAMPBELL

Submitted to the Office of Graduate Studies of
Texas A&M University
in partial fulfillment of the requirements for the degree of

DOCTOR OF PHILOSOPHY

August 2012

Major Subject: Physics

Improvements to the Calculation of Indirect Signals of

Diffuse Gamma-rays and Neutrinos from Dark Matter Annihilation

# IMPROVEMENTS TO THE CALCULATION OF INDIRECT SIGNALS OF DIFFUSE GAMMA-RAYS AND NEUTRINOS FROM DARK MATTER ANNIHILATION

A Dissertation

by

SHELDON SCOTT CAMPBELL

Submitted to the Office of Graduate Studies of
Texas A&M University
in partial fulfillment of the requirements for the degree of

DOCTOR OF PHILOSOPHY

Approved by:

| | |
|---|---|
| Chair of Committee, | Bhaskar Dutta |
| Committee Members, | Richard Arnowitt |
| | Teruki Kamon |
| | Stephen Fulling |
| Head of Department, | George Welch |

August 2012

Major Subject: Physics

# ABSTRACT

Improvements to the Calculation of Indirect Signals of Diffuse Gamma-rays and Neutrinos from Dark Matter Annihilation. (August 2012)
Sheldon Scott Campbell, B.S., University of Alberta; M.S., University of Alberta
Chair of Advisory Committee: Dr. Bhaskar Dutta

A new formalism is presented for calculating the mean intensity spectrum and angular power spectrum of gamma-rays or neutrinos from extragalactic annihilating dark matter, taking into account the dependence of the relative motions of the annihilating particles on the annihilation cross section.

To model the large scale dark matter distribution of mass and relative velocities, the halo distribution model is comprehensively summarized, and extended to include a universal radial profile of the particles' velocity variance, based on results from N-body computer simulations of dark matter halos. A velocity variance profile, associated with the NFW density profile, is proposed by enforcing a power-law profile of the pseudo phase-space density. This allows the large-scale velocity distribution to be described by virialized, gravitationally bound dark matter halos, as opposed to thermal motions used to describe the velocity distribution in the early Universe. The recent particle motion history of the Universe is presented for the described model.

Sample extragalactic gamma-ray intensities from dark matter annihilation are shown for dark matter annihilating with p-wave, according to a relative-velocity-weighted annihilation cross section $\sigma v = a + bv^2$, for constants $a$ and $b$, with examples taken from supersymmetric models. For thermally produced dark matter, the p-wave suppresses the signal intensity. If $b/a \gtrsim 10^6$, the p-wave hardens the intensity spectrum by an estimated factor of $1 + (6b/a)\Delta_I(E_\gamma)$, and increases the angular power spectrum by a factor also depending on new coefficients $\overline{\Delta^{(1)}_{C_\ell}}(E_\gamma)$ and $\overline{\Delta^{(2)}_{C_\ell}}(E_\gamma)$. The energy-dependence of the new p-wave coefficients $\Delta_I$, $\overline{\Delta^{(1)}_{C_\ell}}$, and $\overline{\Delta^{(2)}_{C_\ell}}$ are shown for various annihilation spectra. Sample

intensity spectra are also presented for Sommerfeld-enhanced annihilation.

The intensity of neutrinos from dark matter annihilation is also considered. The variations between the dark matter annihilation signals for different particle phenomenologies suggest that particle physics constraints are possible from an observed indirect detection signal.

Calculations of the annihilation signal from the galactic halo are also shown. The extragalactic signal's intensity is found to be consistent in magnitude with the galactic intensity—within the uncertainty of the models of the dark matter distribution—when looking out from the galactic plane. This suggests that the total cosmic signal may have significant contributions from both components.

# DEDICATION

To my parents who provided an environment that encouraged me to be curious and to pursue my own interests,

To my grandparents for showing me how fulfilling the world can be,

To my brothers who challenge my perspectives on Life, the Universe, and Everything,

To Bhaskar for challenging my efforts, and creating a healthy climate for productive work,

To my friends who challenge my lifestyle and encourage time for play,

To Kelly who rejuvenated my joy in life, work, and play.

This work is a product of the balance made possible by these, for whom I am eternally grateful.

# ACKNOWLEDGMENTS

I am grateful to Bhaskar Dutta for constant discussions, feedback, ideas, and encouragement. He deserves the bulk of the credit for the fact that my postgraduate experience at Texas A&M University was such a positive one.

The idea for my dissertation project arose from the work of Shin'ichiro Ando and Eiichiro Komatsu, and from discussions with Eiichiro Komatsu, Richard Arnowitt, and Bhaskar Dutta. The ideas for considering neutrino production from dark matter annihilations arose from discussions with Rouzbeh Allahverdi and Bhaskar Dutta.

I thank Shin'ichiro Ando for kindly taking the time to compare numerical results with early versions of my programs, thereby providing crucial assistance with the debugging of the code. I am grateful to Eiichiro Komatsu for agreeing to collaborate on the early stages of this project, and helping to justify that the suggested generalizations to the halo model of large scale structure are reasonable with current scientific knowledge. Thank you to Carsten Rott for helpful discussions about the detection of neutrinos by IceCube, and about the atmospheric neutrino background.

During my time as a doctoral student, I have many memories of receiving assistance from many good friends–many acts of kindness, too few of which I have been able to properly return. These who have positively affected my life have all contributed in their own way to the completion of this work. For this I wish to humbly thank Jonathan Asaadi, Karie Badgley, Bill Bassichis, Kris and Jessica Byboth, Matt Cervantes, Michael Cone, Daniel Cruz, Kelly Dilworth, Sean Downes, Jim and Kim Ferguson, Ellie Figueroa, Melissa Fuller, Sam Gooding, Alfredo Gurrola, Mark Hickey, Teruki Kamon, Abram Krislock, Tristan Leggett, Lauren Light, David Maffei, Jude Magaro, Angela Marotta, Dan Melconian, Roy Montalvo, Tyler Morrison, Tim Mottershead, Abid Mujtaba, Melanie Ness, Jim and Melanie Pivarski, Nate and Kim Pogue, Kelley Reaves, Kevin Resil, MT Reynolds, Sandi Smith, Matthew Sears, Enrico Sessolo, Elizabeth Sooby, Ty Stiegler, Vaikunth

Thukral, Mike VanDyke, Andy and Kari Wagers, and Kechen Wang.

I thank Abram Krislock for sharing his document formatting files used to meet the thesis office guidelines.

Finally, a big thank you to Lyn Campbell for her gigantic, tireless effort in proofreading this dissertation. I am deeply indebted and grateful.

TABLE OF CONTENTS

Page

Page

# LIST OF FIGURES

Page

Page

# LIST OF TABLES

# 1 INTRODUCTION

The existence of dark matter in the Universe consistently explains many astronomical observations over a huge range of distance scales. The light-to-mass ratios of dwarf galaxies [1], as well as the velocities of stars within spiral galaxies [2] and elliptical galaxies [3], suggest there is much more matter within the galaxies than can be observed from the radiation they emit. Results are similar for the speeds of galaxies within galaxy clusters [4]. The distribution of this dark mass throughout space can be indirectly observed from the weak lensing of light propagating from far away galaxies. The masses of galaxies and galaxy clusters determined dynamically from velocity dispersions have been verified independently by gravitational lensing. This has been done for individual galaxies [5] and for galaxy clusters [6]. The physical spatial separation of the light and mass of colliding galaxy clusters, such as observed with the Bullet Cluster, shows that the excess mass does not come from radiating matter [7]. Weak gravitational lensing has also made possible the construction of dark matter maps over extended regions of space [8] which are consistent with the properties of the distribution of dark matter generated from large scale simulations of matter undergoing gravitational collapse [9].

The presence of a large component of dark matter is also evident in the cosmic microwave background (CMB) [10–12], where the lensing effects of the dark matter on primordial light emitted from the sphere-of-last-scattering (the time when atoms form and the Universe becomes transparent) are imprinted in the fluctuations in the CMB. Acoustic vibrations in the early Universe are also imprinted in the distribution of galaxies today. This so-called baryon acoustic oscillation has been measured by the Sloan Digital Sky Survey and 2dF Galaxy Redshift Survey [13], and is consistent with a significant non-baryonic matter content. Observations of high-redshift type-Ia supernovae have been able to measure the speeds of galaxies at large distances and have discovered the acceleration of the Universe [14].

---

This dissertation follows the style of Physical Review D.

All of these observations provide a consistent picture, which has led to the standard model of cosmology which posits that the current energy fraction of baryons in the Universe is only about 4%, dark matter is 23%, and the remaining energy of the Universe is due to dark energy, responsible for the observed acceleration of the Universe.

This low energy density of baryons in the Universe is also consistent with independent observations of the abundance of elements, such as deuterium, in primordial cosmic gas. This abundance depends on the baryon density, according to the standard theory of Big Bang Nucleosynthesis (BBN), which explains the production of deuterium, helium-4, helium-3, and lithium-7 during the Big Bang at the beginning of the Universe. The abundances of D, $^4$He, and $^3$He are in agreement with the observations for a low energy density of baryons [15], although presently, there is a discrepancy with the $^7$Li abundance (some proposals to account for this discrepancy are reviewed in [16]). Thus, it is well established that the majority of matter and energy in the Universe is not baryonic.

Simulations of galaxy formation also appear to require a certain amount of cold (that is, non-relativistic) dark matter, in order for gravitational clustering of matter to begin early enough to generate structure that is consistent with the observed distribution of galaxies and galaxy clusters [17]. On scales of tens of megaparsecs, the matter is seen to collapse into a cosmic web of intersecting planes and filaments. The densest regions are found at the cores of halos of dark matter. Halos containing clusters of galaxies can be as large as about $10^{15} M_\odot$, and the Milky Way halo is thought to have a mass of $2 \times 10^{12} M_\odot$.

It has been postulated that the dark matter could be cold, baryonic material whose radiations are too dim to be observed. As explained above, this is at odds with the results of the BBN. In addition, observations of high-redshift light from QSOs shows absorption features known as the Ly$\alpha$ forest, due to interaction with H I gas in the intergalactic medium (IGM). These absorption features are consistent with the same low baryon density seen in the other experiments, enforcing a small dark baryon content in the IGM [18]. In galaxy clusters, the IGM becomes very hot at

the center of the cluster and emits X-rays. Observations of these X-rays establish that the baryons in the cluster account for a small portion of the total mass of the cluster, determined from virial motions of the galaxies or from gravitational lensing by the cluster [19]. It was previously thought that a significant portion of the halo mass could be due to massive compact halo objects (called MACHOs), such as brown dwarfs, red dwarfs, white dwarfs, quiescent neutrons stars, and black holes. The EROS 2 experiment searched for these objects in our own halo by observing events caused by their passage in front of a star in the Large Magellanic Cloud. The results showed conclusively that MACHOs make up a very small portion of our dark matter halo [20].

Dark matter must be electrically neutral because it does not radiate. The only stable, neutral candidate matter remaining in the standard model are the neutrinos. However, the particle masses are too light to contribute significantly to the energy content of the Universe [21], and this matter is too relativistic to create the structure needed to form galaxies in the Universe, according to the cosmological simulations [22]. One is left with the conclusion that dark matter is a new form of matter beyond the standard model of particle physics. As seen from the Bullet Cluster, the dark matter has very low viscosity, and hence interacts very weakly with baryonic matter.

One theoretical paradigm that may account for dark matter is that of the thermally produced weakly interacting massive particle (WIMP). Here, dark matter is one or more new stable particles beyond the standard model. These particles are produced and annihilated in thermal equilibrium in the Big-Bang plasma of the early Universe. As the Universe expands and cools, it eventually becomes too cool to produce new dark matter particles efficiently. These particles continue to annihilate until the rate of annihilation becomes smaller than the expansion rate of the Universe, at which point annihilations become rare and the dark matter content of the Universe freezes out. This theory accounts for the observed density of dark matter if, at the moment of freeze-out, the average velocity-weighted dark matter annihilation cross section is $\overline{\sigma v} \approx 10^{-36}\text{cm}^2$ in unit light speed units. The strength of these interactions would then be of the same

magnitude as the strength of the weak nuclear interactions, suggesting a tantalizing connection between the electroweak theory of the standard model and the new physics that accounts for the dark matter sector.

Modern experimental efforts to determine the properties of dark matter fall into one of three categories: collider, direct detection, and indirect detection. These three methods are complementary to each other because they probe different sectors of the dark matter interactions with standard model particles.

In collider experiments, standard model particles are collided with one another at high energy in order to produce dark matter particles, which will be lost in the experiment, resulting in a measurement of missing transverse energy. If the products of these decays are captured by the experiment's detectors, it may be possible to reconstruct the correct particle theory and determine the nature of the dark matter particle.

Direct detection experiments attempt to detect cosmic dark matter scattering off of a nucleon in a lab detector. These experiments constrain the scattering cross section for different particle masses, and they appear to be at tension with one another. The noble gas detector XENON100 experiment has observed no signal [23]. The CDMS-II experiment observed an excess of 2 events in its signal region [24]. The CRESST-II experiment also detected excess signal events [25]. The DAMA/NaI, DAMA/LIBRA [26], and CoGeNT [27] experiments have observed annual modulations in their event rates, that appear to be consistent [28], and could be interpreted as a change in dark matter flux through the detector as the Earth's orbit travels through the dark matter halo of our galaxy [29]. However, these different signals prefer different regions of parameter space, all of which would be expected to have been detected already by the XENON experiments, if one assumes standard dark matter interactions, and standard models of local phase space distribution in our solar system. As detector and experimental technology improves, the observed anomalies can be independently verified, and their causes zeroed in upon.

Indirect detection of dark matter entails the detection of products from annihilating cosmic dark matter. Experiments looking for signs of annihilating dark matter in the high energy gamma-rays are the Fermi Gamma-ray Space Telescope (FGST) [30], and atmospheric cherenkov telescope arrays such as HESS [31] and VERITAS [32]. High energy cosmic neutrino products of dark matter are searched for by experiments such as IceCube [33], AMANDA-II [34], and ANTARES [35]. Novel charged cosmic rays include positrons, antiprotons, antideuterium, and so on. Currently, these are being actively sought by the AMS-02 [36], PAMELA [37], and ATIC [38] experiments, among others. The FGST has also accomplished using its calorimeter, while using the Earth as a shadow and magnetic source, to make measurements of cosmic rays competitive with PAMELA [39].

Annihilations occur more often in regions of space where the dark matter is denser. The intensity of products is also higher when closer to the source. With this in mind, there are a number of sources most often considered when looking for indirect dark matter signals. These include the Sun, nearby dwarf galaxies orbiting the Milky Way, the Milky Way halo and galactic core, and the extragalactic halo cores (such as from galaxy clusters) and subhalos.

In the Sun, dark matter particles may scatter off a solar nucleus and be captured gravitationally, eventually collecting at the Sun's core. Annihilation of these particles may result in a population of high energy neutrinos being emitted from the Sun. Current constraints on this signal are placed by the IceCube and AMANDA-II experiments [40]. Nearby dwarf galaxies have very small light-to-mass ratios, providing verified large dark matter densities in relatively close proximity. Observations of dwarf galaxies by the Fermi Large Area Telescope (LAT) aboard the FGST have not observed any excess gamma-rays, providing some of the most stringent constraints on the annihilation properties of dark matter [41]. From these results, it is apparent that the dark matter annihilation signal will not be bright, and may need to be extracted from among other background astrophysical sources of radiation by carefully designed precision experiments.

It is pertinent to also consider radiation from diffuse dark matter within the halo

that our galaxy resides in. While gamma-rays and neutrinos can be traced back to their sources, charged cosmic rays follow chaotic paths within the interstellar medium. The PAMELA experiment detected a larger than expected positron fraction in the energy range of 60–100 GeV [37], which has recently been verified by the FGST [39]. If this excess were produced by dark matter annihilation within our halo, it would require quite a large annihilation cross section, at odds with the Sun and dwarf galaxy experiments. It is therefore more likely that this excess will be understood from improved models of emissions from other astrophysical phenomena, such as supernova remnants and pulsar wind nebulae [42].

Since the halo is most dense at the galactic core, it may be a good strategy for gamma-ray and neutrino detectors to focus there. Unfortunately, that region is a very bright gamma-ray source, and it would be difficult to extract an annihilation signal from there, but the neutrinos do not suffer such backgrounds. In fact, the dominant neutrino source at energies on the order of 100 GeV are atmospheric neutrinos due to decays of muons produced from cosmic rays interacting with the atmosphere [43].

It has been suggested that perhaps the brightest source of dark matter annihilation may be subhalos within our galactic halo (including dwarf galaxies) [44]. The distribution of these subhalos would be quite different from other gamma-ray sources in the galaxy, and therefore would give a distinct anisotropy modulation, seen in the gamma-ray angular power spectrum [45]. Unfortunately, this may be difficult to predict: the abundance of galactic subhalos predicted by halo simulations has not been observed [46]. While some subhalos may be too dim to be discovered (having too few baryons and/or being too distant), it is also possible that the simulations are not yet accurate in this regard. However, detection of a distinct modulation in the angular power spectrum due to these subhalos would provide constraints, not only on the dark matter particle properties, but also on the galactic subhalo population.

It may be that the annihilation signal due to extragalactic dark matter halos is more predictive. The distribution of dark matter halos is consistent across a variety

of independent simulations [47], and is in reasonable agreement with the observed distribution of galaxies and galaxy clusters [48]. The fact that relaxed halos have universal density profiles [49, 50] has allowed the development of a simple semi-analytic model for the distribution of dark matter, known as the halo model. This allows, in principle, the calculation of both the mean intensity and the angular power spectrum of gamma-rays or neutrinos from extragalactic dark matter annihilation for any theory of annihilation. Charged cosmic rays would be blocked by the intergalactic medium. This extragalactic source has the advantage that the annihilation signal would also have a distinct angular signature in the gamma-ray sky, perhaps making it easier to extract, if it is dim when compared with other gamma-ray sources. It is therefore important to consider improvements to the theoretical predictions of these extragalactic signals. If such a signal were to be observed, it would not only provide constraints on the particle nature of dark matter, but also on the large-scale distribution of matter in the Universe.

Estimates of the extragalactic gamma-rays from annihilating dark matter have been carried out [51, 52], using the spherical halo model to describe the distribution of dark matter [53], and assuming the annihilation properties do not depend on the relative momentum of the annihilating particles. However, there are many realistic models of dark matter for which the rate of annihilation (determined from the annihilation cross section) changes with the energy of interaction. In order to probe these models of dark matter with extragalactic indirect detection, predictions of the signals need to be determined and compared against the observed gamma-ray data.

Presented in this dissertation is a framework for estimating the mean intensity spectrum of gamma rays from velocity-dependent annihilating dark matter, and the angular power spectrum of this radiation. To do this, a model of the velocity distribution of matter is incorporated into the spherical halo model using information from the latest high-resolution simulations of dark matter halos. The development and generalization of the halo model is explained in Section 2. In Section 2.1, the Friedmann-Lemaître-Robertson-Walker (FLRW) cosmology is reviewed to establish its basic notations. On large scales, structure formation is described by linear equations. The justification for these equations, their solution

via the linear growth factor, the power spectrum of linear fluctuations, and the variance of matter on linear scales are reviewed in Section 2.2.

The halo model is used to describe matter in the non-linear regime. Its development begins by reviewing the lessons from spherical collapse of matter in Section 2.3, where we come to understand the conditions for an isotropic density of matter to collapse gravitationally on itself. In Section 2.4, the formalism of excursion of sets is reviewed to see how it is used to derive the halo mass function. The mass function provides a one-point statistic of the distribution of halos. The model of linear halo bias is described in Section 2.5, and it provides information about the two-point statistics of the halo distribution. Each halo is described by its universal profiles.

In Section 2.6, the observed universal halo profiles of halo density are reviewed. Newly introduced to the halo model here is the application of the universal pseudo-phase-space density profile observed in halo simulations. When a universal pseudo-phase-space density profile is postulated for a collisionless gravitational system, a closed set of equations determines a family of density profiles and associated universal profiles of the particle velocity variance at each position in the halo. This fact is exploited to develop a new method for determining affiliated universal velocity variance profiles from any given universal density profile. From the velocity variance profile, a universal halo profile of relative particle velocities can be determined.

All of the ideas of this section are brought together in Section 2.7 to define the simplest spherical halo model of large scale structure with rigid, disjoint, relaxed, spherical halos whose properties depend only on the halo's mass and observed redshift. Central to this model is the distribution of halo concentrations with halo mass and redshift. Although the sample calculations done in this dissertation neglect the effects of halo substructure on the dark matter annihilation signals, studies show that they are important to the signal. Thus, some results about the distribution of halo substructure are shared in Section 2.7.5, in order to inform later discussion of its effects on the extragalactic indirect detection signals. Some

properties of the large scale structure described by the simple halo model are presented in Section 2.8.

This framework for describing the large-scale structure of matter is used to quantify the effects of the velocity-dependence of dark matter annihilation on cosmic annihilation signals for a variety of dark matter phenomenologies. The contributions of particle physics to these cosmic signals is discussed in Section 3. In Section 3.1, the necessary particle physics quantities are introduced, including the dark matter mass, annihilation spectrum, and annihilation cross section. Different phenomenologies that give rise to a dependence of the annihilation cross section on the annihilating particles' relative velocity in the non-relativistic regime are explained in Section 3.2. Section 3.2.1 discusses p-wave annihilation, Section 3.2.2 explains Sommerfeld-enhanced annihilation and Sommerfeld resonances, and Section 3.2.3 examines interesting scenarios of dark matter annihilating through a Breit-Wigner resonance.

The large scale structure of dark matter and its particle physics properties are brought together in Section 4 to calculate the intensity of cosmic dark matter annihilation radiation. Section 4.1 explains how to calculate new expressions for the angular distribution of the intensity spectrum of gamma rays from dark matter annihilation for any specified phase space distribution of the dark matter, and for any theory of annihilation. This result is then used to derive the mean annihilation gamma-ray intensity in Section 4.2, and the gamma-ray angular power spectrum in Section 4.3, in the context of the universal halo model of large scale structure. The effects of the velocity dependence of the annihilation cross section are considered in the new formulations. The formalism in this section provided the basis for a new computer program that I developed to calculate predictions numerically for the annihilation observables.

Results from the calculations of extragalactic annihilation gamma-rays are presented in Section 5. In Section 5.1, specific particle physics models for which calculations were carried out are described. Results for s-wave and p-wave annihilation are presented in Section 5.2, and results for Sommerfeld-enhanced

annihilation appear in Section 5.3.

In Section 6, the strengths of the extragalactic intensity spectra are compared to the strengths of the intensities from annihilations in the Milky Way smooth component of the dark matter, and the calculation tools are then applied to calculate signals of neutrino radiation. The intensity formula derived in Section 4.1 is applied to the galactic halo, and the standard formulae for the angular distribution of the galactic annihilation signal are reproduced in Section 6.1. Section 6.2 contains comparisons of the predicted extragalactic and galactic gamma-ray annihilation signals and explores the question of which signal is dominant. Since the dark matter annihilation models considered in Section 5 also produce neutrinos, it is interesting to consider the predicted neutrino radiation from dark matter annihilation. These results are presented in Section 6.3.

The results and conclusions of this dissertation are summarized in Section 7.

Some supplemental material is provided in two appendices. Appendix A outlines numerical algorithms developed to calculate Fourier transforms of universal halo functions, needed for calculation of the angular power spectrum of the extragalactic dark matter annihilation radiation. Appendix B explains the method used to calculate galactic intensities of the annihilation radiation from observation cones centered on the galactic center, in the case where it contains a Navarro-Frenk-White cusp.

# 2 LARGE SCALE STRUCTURE OF MATTER AND THE SPHERICAL HALO MODEL

The distribution of the production of radiation from extragalactic dark matter annihilation depends on the phase space distribution of the dark matter. Making a successful prediction of an extragalactic indirect detection signal of dark matter requires a reasonably realistic description of the distribution of dark matter in our Universe. An important aspect of this work is determining those aspects of the large scale structure that are most important to understand for a robust determination of annihilation radiation.

Much of the detailed information of large scale structure comes from N-body cosmological simulations. It is important to remember that the results of the simulations must be compared against astrophysical observations, in order for their validity to be verified. In fact, extragalactic dark matter annihilation radiation may provide new observational constraints on large scale structure, if this radiation is observed. When cold dark matter is simulated in a simple cosmology consistent with observations, the matter collapses into huge structures–filaments and planes that form a cosmic web. These large structures are made up of smaller dark matter halos, spherical or ellipsoidal gravitationally bound collections of dark matter. Structure formation is hierarchical with small halos forming initially, and then merging to form larger halos. This is consistent with observations of galaxies that suggest that each galaxy is enveloped in a dark matter halo. The distribution of halos in simulations is consistent with the observed distribution of galaxies in our Universe. The accuracy of cosmological simulations is inferred from the comparison of independently developed simulation algorithms and codes [47]. The detailed results of these different programs agree amazingly well with one another. These results give us reason to rely on simulated distributions to describe the large scale structure of the Universe, though this needs to be done with an eye toward observational verification of the important results.

One method for predicting an extragalactic dark matter annihilation signal would

be to integrate directly over the distribution from a large scale simulation. This has the benefit of precisely accounting for all aspects of simulated results. This idea was carried out for the results of the Millennium-II simulation, for an s-wave annihilating dark matter [54]. Calculations of this type are very important to provide a baseline for annihilation signal predictions. However, they do have a number of drawbacks.

- The simulations have limited resolution and volume, and therefore effects at higher resolution or at scales larger than the simulation volume must be modeled.
- The simulation is done with a fixed set of cosmological parameters. To see data with different parameters requires that a new, costly simulation be run.
- It is difficult to quantify the importance of specific aspects of the large scale structure on the annihilation signal with this method. For example, removing halo substructure to determine the effect the substructure has for that particular simulated distribution.

To this end, it makes a great deal of sense to make use of available semi-analytical models of large scale structure, of which the spherical halo model is an example. These are simplified descriptions of the large scale structure, but should be sophisticated enough to account for the results found from a full simulated distribution. The simplicity of the semi-analytic models allows for fast calculations of predictions, permitting effects of different cosmologies to be compared easily. New effects can be quantified by adding them to the model.

The purpose of this section is to provide a comprehensive review and motivation for the model of large scale structure used in the extragalactic indirect detection calculations. It begins by briefly reviewing cosmological results in Sections 2.1–2.3, introducing the notations used throughout the dissertation, and deriving results used as inputs in the halo model. In Sections 2.4–2.6, I will briefly describe the components of the simplest of realistic semi-analytic models of large scale structure, which is an ensemble of universal, rigid, disjoint, spherical dark matter halos. The

properties of the halos in this model are specified by only their mass and observed redshift. The halo model provides a framework to specify statistical information about the mass distribution of dark matter across the Universe, and has been used in previous research to calculate extragalactic signals of s-wave annihilating dark matter. The intensity of emitted annihilation products scales as the square density, as described in Section 4, and is therefore only contributed to by the densest regions of space. This model provides a realistic annihilation signal produced from the densest regions of the halos—their cores—provided that the halo cores are modeled correctly.

In order to quantify effects of velocity-dependent dark matter annihilation, one needs to model the distribution of 1-point relative velocities of the dark matter particles. In Section 2.6, I explain a method for modeling these relative velocities in the halo model, using results from cosmological simulations. The full halo model of large scale structure used in my analyses is summarized in Section 2.7. Perhaps the most important effect that the model neglects is that of halo substructure. There is much substructure observed within halos by simulations [55, 56], much of it being the cores of absorbed small halos that have remained gravitationally bound. These subhalos also have high densities, and are expected to contribute significantly to extragalactic annihilation signals. Since this has significant consequences for the conclusions of the work in this document, halo substructure is further discussed in Section 2.7.5. This section is concluded by showing some properties of the simple halo model in Section 2.8.

## 2.1 Brief Review of FLRW Cosmology

The cosmology of an isotropic and uniform perfect fluid is now widely attributed to Friedmann, Lemaître, Robertson, and Walker (FLRW) [57]. The hypothesis that our observable Universe is uniform and isotropic is supported by observations of the distribution of galaxies, and the cosmic microwave background. Any uniform and isotropic spacetime metric can be transformed to coordinates such that it is written

as [58, 59]

$$\mathrm{d}s^2 = -\mathrm{d}t^2 + a^2(t)\left[\frac{\mathrm{d}r^2}{1-kr^2} + r^2\mathrm{d}\Omega^2\right], \tag{2.1}$$

where $t$ is known as the comoving time coordinate in natural units with light speed $c = 1$, $r$ is the physical radial coordinate, $\mathrm{d}\Omega$ is the usual solid angle infinitesimal, $a(t)$ is the scale factor, and $k$ specifies the local curvature: if the Universe is positively curved, then $k = 1$; if negatively curved, $k = -1$; and if the Universe is flat, then $k = 0$. Since cosmological observations are consistent with a flat Universe, $k = 0$ is used throughout this work. The comoving coordinates are chosen so that $t = 0$ today and $a(0) = 1$.

The dynamics of the Universe encoded in the scale factor $a(t)$ are determined from the theory of general relativity via solutions of Einstein's equation for appropriate matter fields described by the energy-momentum tensor. When the energy-momentum tensor describes independent perfect fluids enumerated by $i$, each with its own uniform energy density $\rho_i$ and pressure $p_i$, at rest in the comoving rest frame, Einstein's equation can be written as the Friedmann equation and acceleration equation

$$H^2 \equiv \left(\frac{\dot{a}}{a}\right)^2 = \frac{8\pi G}{3}\sum_i \rho_i + \frac{\Lambda}{3}, \tag{2.2}$$

$$\frac{\ddot{a}}{a} = -\frac{4\pi G}{3}\sum_i (\rho_i + 3p_i) + \frac{\Lambda}{3}, \tag{2.3}$$

where the dot in $\dot{a}$ expresses differentiation with respect to comoving time, $H$ is the Hubble function, $\Lambda$ is the cosmological constant, and $G$ is the universal gravitational constant. Important fluids in the lifetime of the universe include photon radiation where $p_r = \rho_r/3$, and matter fields such as baryonic matter, neutrinos, and dark matter, where $p_m = 0$ to excellent approximation for most of the Universe's evolution. The cosmological constant term can equivalently be interpreted as a component of the energy-momentum tensor (contributing to dark energy, and often associated with vaccuum energy) with constant energy density

$$\rho_\Lambda = \Lambda/(8\pi G) \tag{2.4}$$

and pressure $p_\Lambda = -\rho_\Lambda$.

Energy conservation is expressed as the vanishing covariant divergence of the energy-momentum tensor, which becomes the constraint

$$\sum_i \Big[\dot{\rho}_i + 3H(\rho_i + p_i)\Big] = 0. \tag{2.5}$$

If the energy exchange between different fluid components is negligible, then each component $i$ satisfies the constraint separately. Then the energy constraint is separable, and one finds

$$\rho_m(t) \propto a^{-3}(t) \propto t^{-2}, \tag{2.6}$$

$$\rho_r(t) \propto a^{-4}(t) \propto t^{-2}. \tag{2.7}$$

As the Universe expands, the radiation energy density eventually becomes negligible and the Universe becomes matter-dominated. For the purposes of this work, radiation can be neglected throughout. However, in the presence of a small, positive $\Lambda$, $\rho_m$ eventually becomes small with respect to $\rho_\Lambda$ and the Universe becomes dominated by dark energy. This transition does contribute to the calculations in this dissertation, so both matter and dark energy must be taken into account.

Once $a(t)$ is determined, then one could use the value of $a$ to specify cosmic time, with $a = 0$ at the beginning of the Universe, increasing to $a = 1$ today. Another more convenient measure of cosmic time for observational cosmologists is cosmological redshift $z$. As light propagates in an expanding Universe, its wavelength expands with the scale factor and the light becomes redshifted. A photon emitted with wavelength $\lambda_e$ at rest in the comoving frame at some time in the distant past at time t is redshifted to the observed wavelength $\lambda_o$ according to

$$1 + z = \frac{\lambda_o}{\lambda_e} = \frac{a(0)}{a(t)} = \frac{1}{a}. \tag{2.8}$$

Thus, if $a(t)$ is properly understood, then measuring the cosmological redshift of some light determines how long ago it was emitted from its source. The coordinate

distance to the source (recalling $t < 0$, and radial null geodesics satisfy $-\mathrm{d}t^2 + a^2(t)\mathrm{d}r^2 = 0$) is

$$r = \int_{ct}^{0} \mathrm{d}r = \int_{t}^{0} \frac{\mathrm{d}t}{a(t)} = \int_{a}^{1} \frac{a}{\dot{a}} \frac{\mathrm{d}a}{a^2} = \int_{0}^{z} \frac{\mathrm{d}z}{H(z)}. \tag{2.9}$$

An expression for the Hubble function in terms of redshift follows simply from the Friedmann equation. In a flat Universe with no cosmological constant, Equation (2.2) shows that the total energy density of the Universe is the critical energy density, defined as

$$\rho_c \equiv \frac{3H^2}{8\pi G}. \tag{2.10}$$

Denoting the energy content of matter and dark energy today as

$$\Omega_m = \frac{\rho_m(0)}{\rho_c(0)}, \tag{2.11}$$

$$\Omega_\Lambda = \frac{\rho_\Lambda(0)}{\rho_c(0)} = \frac{\Lambda}{3H_0^2}, \tag{2.12}$$

respectively, where $H_0 \equiv H(0)$ is the Hubble constant. The Hubble constant is normally specified by $h$, where

$$H_0 \equiv 100h \text{ km/s/Mpc}. \tag{2.13}$$

The Friedmann equation (2.2), with (2.6), becomes the Hubble function as a function of redshift

$$H(z) = H_0 \sqrt{\Omega_m (1+z)^3 + \Omega_\Lambda}. \tag{2.14}$$

The matter content can be broken into different terms, including baryons $\Omega_b$, cold dark matter $\Omega_c$, neutrinos $\Omega_\nu$, and so on.

It is convenient to use redshift as a time coordinate to describe the evolution of the energy content of the Universe. The time associated with a given redshift is

$$t = -\int_{a}^{1} \frac{\mathrm{d}a}{\dot{a}} = -\int_{0}^{z} \frac{\mathrm{d}z}{(1+z)H(z)}. \tag{2.15}$$

At any redshift, the matter content is

$$\Omega_m(z) = \frac{\rho_m(z)}{\rho_c(z)} = \frac{\Omega_m \cdot (1+z)^3}{\Omega_r \cdot (1+z)^4 + \Omega_m \cdot (1+z)^3 + \Omega_\Lambda}, \tag{2.16}$$

where (2.7) was used to add the appropriate radiation dependence to the Hubble function. Unless redshift dependence of the matter content is explicitly stated by writing $\Omega_m(z)$, writing $\Omega_m$ will always refer to the matter content today at $z = 0$. Similarly,

$$\Omega_r(z) = \frac{\Omega_r \cdot (1+z)^4}{\Omega_r \cdot (1+z)^4 + \Omega_m \cdot (1+z)^3 + \Omega_\Lambda}, \tag{2.17}$$

$$\Omega_\Lambda(z) = \frac{\Omega_\Lambda}{\Omega_r \cdot (1+z)^4 + \Omega_m \cdot (1+z)^3 + \Omega_\Lambda}. \tag{2.18}$$

Current cosmological observations are consistent with this cosmology [12] with $\Omega \equiv \Omega_\Lambda + \Omega_m + \Omega_r \approx 1$, $\Omega_\Lambda \approx 0.725$, and the redshift of matter-radiation equality being $z_{\text{eq}} \approx 3200$. It follows that

$$\Omega_r = \frac{1}{z_{\text{eq}} + 2}(\Omega - \Omega_\Lambda) \approx \frac{\Omega - \Omega_\Lambda}{z_{\text{eq}}} \approx 8.6 \times 10^{-5},$$
$$\Omega_m = \frac{z_{\text{eq}} + 1}{z_{\text{eq}} + 2}(\Omega - \Omega_\Lambda) \approx \left(1 - \frac{1}{z_{\text{eq}}}\right)(\Omega - \Omega_\Lambda) \approx 0.275.$$

Figure 1a plots the energy contents of the Universe on a log scale in $1 + z$, from present day back to the time of matter-radiation equality when the Universe became matter dominated. Today, the radiation content is negligible, but the matter and dark energy contents are still of the same order of magnitude—we are presently in the epoch of transition from matter domination to dark energy domination.

Extrapolation to future times is shown in Figure 1b, on a linear scale in redshift, where $z$ approaches $-1$ as time goes to infinity.

Another important result is with regard to the age of the Universe $t_U$ at redshift $z$.

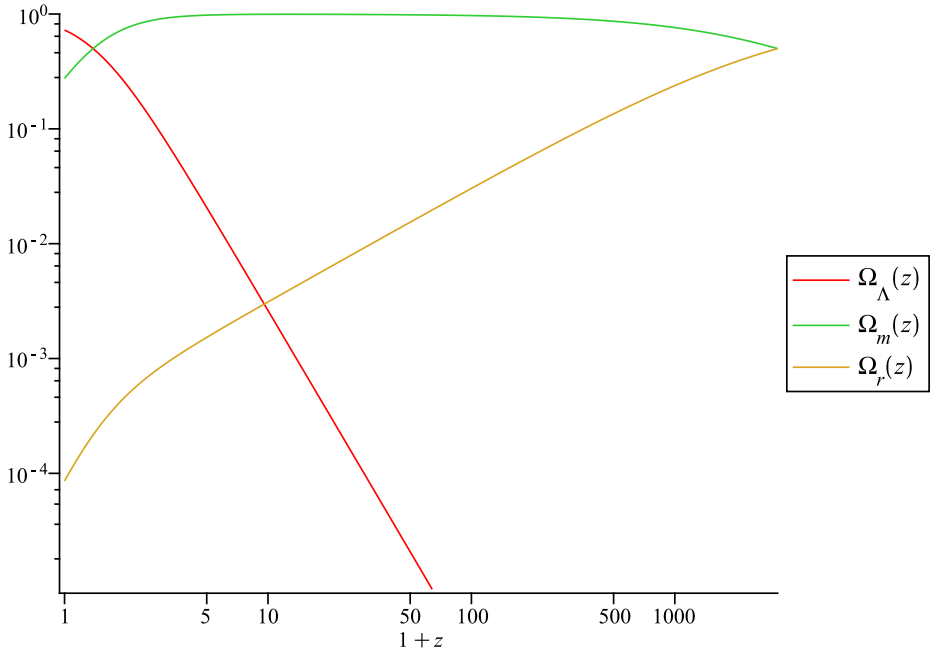


(a)

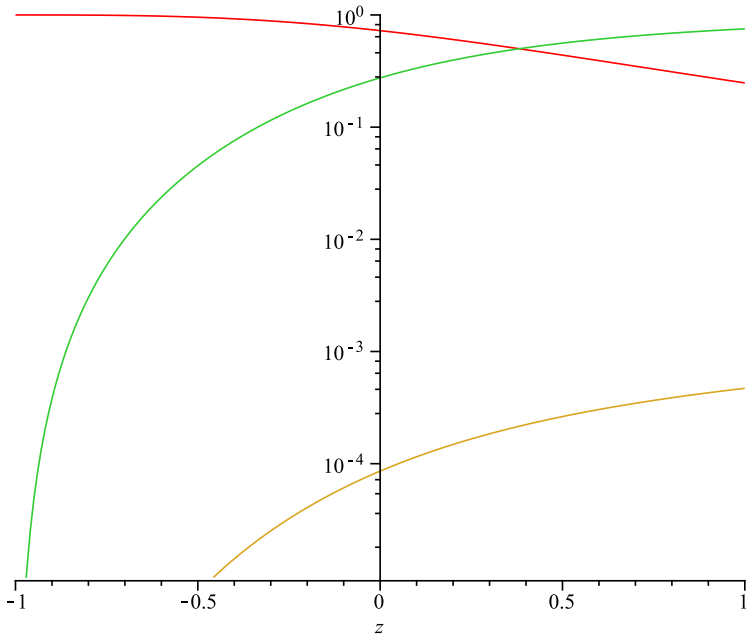


(b)

Figure 1: The energy content of the Universe. (a) The energy content of the Universe from the present to the time of matter-radiation equality, over a log scale in $1+z$. (b) The energy content of the Universe on linear redshift scale, extrapolated to future times at negative redshift, and going back to $z = 1$.

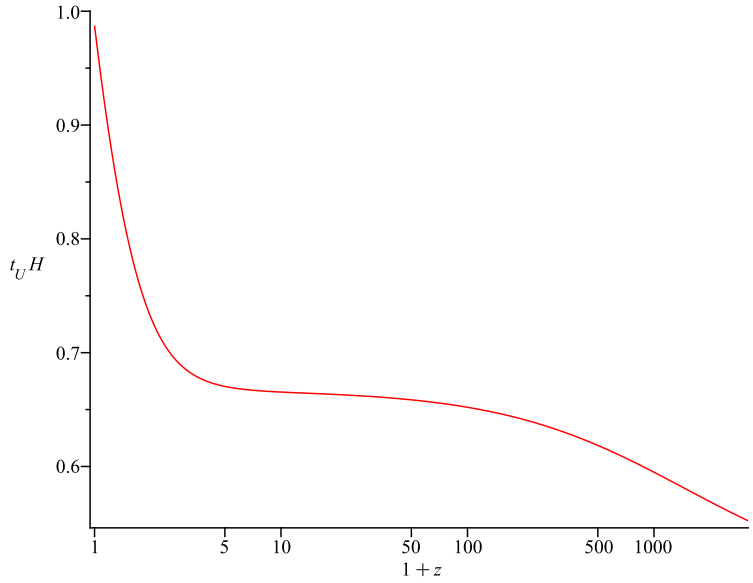


Figure 2: The age of the Universe in units of the inverse Hubble function at redshift $z$.

Beginning with (2.15),

$$t_U(z) = \int_z^\infty \frac{1}{H(z')} \frac{\mathrm{d}z'}{1+z'} = \frac{F(z)}{H(z)}, \tag{2.19}$$
$$F(z) \equiv \int_z^\infty \sqrt{\frac{\Omega_\Lambda + \Omega_m \cdot (1+z)^3 + \Omega_r \cdot (1+z)^4}{\Omega_\Lambda + \Omega_m \cdot (1+z')^3 + \Omega_r \cdot (1+z')^4}} \frac{\mathrm{d}z'}{1+z'} \sim 1$$

for parameters consistent with observations (see Figure 2). Therefore, the Hubble time $H^{-1}$ provides an approximation of the age of the Universe, and the Hubble length $c/H$ estimates the length scale of the observable Universe, or the distance to the horizon of the Universe.

## 2.2 Matter Collapse on Linear Scales

In this section is derived the description of the growth of structure on linear scales. At the beginning of the matter-dominated period, when matter was the dominant energy density in the Universe, fluctuations in the matter density are small. That is, the matter overdensity at each region of space

$$\delta_\rho(\mathbf{r}) \equiv \frac{\rho(\mathbf{r})}{\langle\rho\rangle} - 1 \tag{2.20}$$

has a small value

$$|\delta_\rho| \ll 1, \tag{2.21}$$

where $\langle\rho\rangle$ is the mean density at that epoch, corresponding to $\rho_m$ of the previous subsection. The evolution of these perturbations is described by linear equations. In later times, as matter collapses gravitationally and structures grow, $\delta_\rho$ fluctuates greatly and takes on large values at the dense regions. However, when considering average densities over large volumes of space near the homogeneity scale, $\delta_\rho$ is again small at these scales, and its evolution is described by the linear perturbation equations.

### 2.2.1 The Linear Perturbation Equations

This section largely follows the discussion in [60]. Working under the hypothesis of cold dark matter, it will be assumed that the matter is non-relativistic. Therefore, the discussion can begin with the Newtonian fluid equations. Let $\rho(\mathbf{r}, t)$ be the density at the physical coordinates as defined in Section 2.1. Mass conservation leads to the continuity equation

$$\frac{\partial\rho}{\partial t} + \nabla_r \cdot (\rho\mathbf{u}) = 0, \tag{2.22}$$

where $\mathbf{u} = \mathrm{d}\mathbf{r}/\mathrm{d}t$ is the fluid velocity vector, relative to the origin. Conservation of momentum via Newton's Second Law is known as the Navier-Stokes theorem

$$\frac{\partial \mathbf{u}}{\partial t} + (\mathbf{u} \cdot \nabla_r)\mathbf{u} = -\nabla_r \Phi, \tag{2.23}$$

where fluid pressure and stress are assumed to be negligible, and $\Phi$ is the gravitational potential per unit mass, satisfying

$$\nabla_r^2 \Phi = 4\pi G \rho. \tag{2.24}$$

In the context of an expanding Universe, this description is not very convenient or intuitive. Consider two spatially-separated objects, each at rest according to the comoving coordinates, with distance $R$ between them when the scale factor of the Universe had a value of $a_0$. Due to the expansion, the distance between the objects will increase with the scale factor, $r(t) = Ra(t)/a_0$, even though they are "at rest." An observer at one object's location will measure a speed $u = R\dot{a}/a_0$ for the other object. A description of the objects where they can appear to be at rest with respect to one another can be made in a non-inertial coordinate system that expands in accordance with the Universe. Define the expanding, comoving coordinates today, at $t = 0$ so that $a_0 = 1$ and therefore the expanding, comoving radial coordinate $R$ is defined at all times by

$$R = \frac{r(t)}{a(t)} = \frac{r(a)}{a} = r(z)(1+z), \tag{2.25}$$

as parametrized by time, scale factor, or redshift. A fluid with coordinates $R(t)$ that is in motion with respect to the background has proper velocity $\mathbf{u} = a\dot{\mathbf{R}} + \dot{a}\mathbf{R}$. The first term $\dot{a}\mathbf{R} = H\mathbf{r}$ is the relative motion of "at rest" objects, and is referred to as the Hubble flow. The second term in the proper velocity is the motion with respect to the background in expanding coordinates, and is called the peculiar velocity

$$\mathbf{v} \equiv a\dot{\mathbf{R}}. \tag{2.26}$$

Re-define the density function $\rho(\mathbf{r}, t) = \rho(a(t)\mathbf{R}, t)$ to the function $\rho(\mathbf{R}, t)$ that specifies the density at comoving coordinates $(\mathbf{R}, t)$. To write the gravitational

potential in comoving coordinates, consider the Lagrangian for a particle of mass $m$

$$\mathcal{L}(\mathbf{r}, \mathbf{u}, t) = \frac{1}{2} m \mathbf{u}^2 - m\Phi(\mathbf{r}, t).$$

In comoving coordinates, it becomes

$$\begin{aligned}\mathcal{L}(\mathbf{R}, \dot{\mathbf{R}}, t) =& \frac{1}{2} m (a\dot{\mathbf{R}} + \dot{a}\mathbf{R})^2 - m\Phi(a\mathbf{R}, t) \\ =& \frac{1}{2} m a^2 \dot{\mathbf{r}}^2 - m\left(\Phi(a\mathbf{R}, t) + \frac{1}{2} a\ddot{a}\mathbf{R}^2\right) + \frac{\mathrm{d}}{\mathrm{d}t}\left(\frac{1}{2} m a\dot{a}\mathbf{R}^2\right).\end{aligned}$$

Recall that the total time derivative does not affect the equations of motion. This motivates the gravitational potential in comoving coordinates to be defined as

$$\phi(\mathbf{R}, t) \equiv \Phi(a\mathbf{R}, t) + \frac{1}{2} a\ddot{a}\mathbf{R}^2. \tag{2.27}$$

It satisfies the wave equation

$$\nabla^2 \phi(\mathbf{R}, t) = 4\pi G a^2(t)[\rho(\mathbf{R}, t) - \langle\rho\rangle(t)], \tag{2.28}$$

where the new operator $\nabla$ is with respect to the comoving coordinates $R$.It is now possible to write the fluid equations in expanding coordinates. In terms of the new system,

$$\frac{\partial}{\partial t}\rho(\mathbf{r}/a(t), t) = \frac{\partial}{\partial t}\rho(\mathbf{R}, t) - \frac{\dot{a}}{a}\mathbf{R} \cdot \nabla\rho(\mathbf{R}, t),$$

and similarly

$$\nabla_r \cdot (\rho\mathbf{u}) = \frac{1}{a}\nabla \cdot (\rho\mathbf{v}) + 3\frac{\dot{a}}{a}\rho + \frac{\dot{a}}{a}\mathbf{R} \cdot \nabla\rho.$$

Therefore, the continuity equation (2.22) in comoving coordinates becomes

$$\frac{\partial\rho}{\partial t} + \frac{1}{a}\nabla \cdot (\rho\mathbf{v}) + 3\frac{\dot{a}}{a}\rho = 0. \tag{2.29}$$

It is convenient to re-express it in terms of $\delta_\rho$. Making use of the energy conservation relation (2.5)

$$\frac{\partial \langle\rho\rangle}{\partial t} = -3\frac{\dot{a}}{a}\langle\rho\rangle$$

to see that

$$\frac{\partial \rho}{\partial t} = \langle \rho \rangle \frac{\partial \delta_\rho}{\partial t} - 3\frac{\dot{a}}{a}\rho,$$

the continuity equation then takes the form

$$\frac{\partial \delta_\rho}{\partial t} + \frac{1}{a}\nabla \cdot [(1+\delta_\rho)\mathbf{v}] = 0. \tag{2.30}$$

The new Navier-Stokes equation (2.23) is

$$\frac{\partial \mathbf{v}}{\partial t} + \frac{\dot{a}}{a}\mathbf{v} + \frac{1}{a}(\mathbf{v}\cdot\nabla)\mathbf{v} = -\frac{1}{a}\nabla\phi. \tag{2.31}$$

From these coupled equations, it is desirable to have an equation for the dynamics of $\delta_\rho$ alone. If this is accomplished, (2.30) can then be used to determine $\mathbf{v}(\mathbf{R}, t)$ from $\delta_\rho$. To this end, multiply (2.29) by $\mathbf{v}$, multiply (2.31) by $\rho$, and add the results.

$$\frac{\partial(\rho v^i)}{\partial t} + \frac{1}{a}\frac{\partial}{\partial R^j}(\rho v^i v^j) + 4\frac{\dot{a}}{a}\rho v^i = -\frac{\rho}{a}\frac{\partial}{\partial R_i}\phi$$

In this expression, indices repeated in the same term are implicitly summed over. Now replace the density with the overdensity

$$\left[\frac{\partial}{\partial t} + \frac{\dot{a}}{a}\right][(1+\delta_\rho)v^i] + \frac{1}{a}\frac{\partial}{\partial R^j}[(1+\delta_\rho)v^i v^j] = -\frac{1}{a}(1+\delta_\rho)\frac{\partial}{\partial R_i}\phi,$$

and act on the result with the operator $-\frac{1}{a}\frac{\partial}{\partial R^i}$, applying (2.30) to the divergence acting on the first term.

$$\frac{\partial^2 \delta_\rho}{\partial t^2} + 2\frac{\dot{a}}{a}\frac{\partial \delta_\rho}{\partial t} = \frac{1}{a^2}\nabla\cdot[(1+\delta_\rho)\nabla\phi] + \frac{1}{a^2}\frac{\partial^2}{\partial R^i \partial R^j}[(1+\delta_\rho)v^i v^j] \tag{2.32}$$

Then apply (2.30) and (2.32) to the linear regime where overdensities are small. For our discussion, it is suitable to consider distributions where the momentum skewness is negligible. After applying (2.28), the result is the linear perturbation equations

$$\frac{\partial^2 \delta_\rho}{\partial t^2} + 2\frac{\dot{a}}{a}\frac{\partial \delta_\rho}{\partial t} = 4\pi G \langle \rho \rangle \delta_\rho, \tag{2.33}$$

$$\frac{\partial \delta_\rho}{\partial t} + \frac{1}{a}\nabla\cdot\mathbf{v} = 0. \tag{2.34}$$

### 2.2.2 The Linear Perturbation Growth Factor

Following the method of [61], solving (2.33) is done by first expressing it in terms of redshift, instead of comoving time. Similarly to the calculation in (2.15),

$$\frac{\partial}{\partial t} = -(1+z)H(z)\frac{\partial}{\partial z}.$$

For the second time derivative, it is helpful to note, with $H(z)$ being given by (2.14) during structure formation, that

$$\frac{\partial H}{\partial z} = \frac{H_0^2}{2H(z)} 3\Omega_m \cdot (1+z)^2 = \frac{3H(z)\Omega_m(z)}{2(1+z)}.$$

Then the second time derivative can be written as

$$\frac{\partial^2}{\partial t^2} = (1+z)^2 H^2(z)\frac{\partial^2}{\partial z^2} + (1+z)H^2(z)\left(1 + \frac{3}{2}\Omega_m(z)\right)\frac{\partial}{\partial z}.$$

The source term becomes

$$4\pi G \langle\rho\rangle = \frac{3}{2}H_0^2\Omega_m \cdot (1+z)^3 = \frac{3}{2}H^2(z)\Omega_m(z).$$

The linear perturbation equation for $\delta_\rho(z)$ is therefore

$$(1+z)\frac{\partial^2\delta_\rho}{\partial z^2} + \left(\frac{3}{2}\Omega_m(z) - 1\right)\frac{\partial\delta_\rho}{\partial z} = \frac{3\Omega_m(z)}{2(1+z)}\delta_\rho. \tag{2.35}$$

The solutions for the evolution of the linear perturbation $\delta_\rho(z)$ can be written as

$$\delta_\rho(z) = \delta_\rho(0)D(z), \tag{2.36}$$

where $D$ is the linear growth factor, normalized so $D(0) = 1$. It can be verified by substitution that one solution to the linear perturbation equation is

$$D^-(z) = \frac{H(z)}{H_0}.$$

This solution describes shrinking structures. The relevant solution for structure formation is the growing mode solution, found from the method of second solution [62]

$$D(z) = CD^-(z)\int_z^\infty \mathrm{d}z'[D^-(z')]^{-2}\exp\left[-\int_0^{z'}\mathrm{d}z''p(z'')\right],$$

where

$$p(z) = \frac{\frac{3}{2}\Omega_m(z)-1}{1+z} = \frac{1}{H(z)}\frac{\partial H(z)}{\partial z} - \frac{1}{1+z}$$

for the equation under consideration, and $C$ is a constant that enforces $D(0) = 1$. The argument of the natural exponential becomes

$$-\int_0^{z'}\mathrm{d}z''p(z'') = \int_0^{z'}\frac{\mathrm{d}z''}{1+z''} - \int_{H_0}^{H(z')}\frac{\mathrm{d}H}{H} = \ln\left(\frac{H_0(1+z')}{H(z')}\right).$$

The linear perturbation growth factor is therefore

$$D(z) = C\frac{H(z)}{H_0}\int_z^\infty \mathrm{d}z'\left(\frac{H_0}{H(z')}\right)^3(1+z'), \tag{2.37}$$

$$C = \left[\int_0^\infty \mathrm{d}z\left(\frac{H_0}{H(z)}\right)^3(1+z)\right]^{-1}.$$

This is well approximated by [63]

$$D(z) \approx \frac{\Omega_m(z)}{(1+z)}\left[\Omega_m^{4/7}(z) - \Omega_\Lambda(z) + \left(1+\frac{1}{2}\Omega_m(z)\right)\left(1+\frac{1}{70}\Omega_\Lambda(z)\right)\right]^{-1}, \tag{2.38}$$

up to a constant factor. According to [64], the error of this approximation is better than $7\times10^{-4}$ for $\Omega_m = 0.27$.

For greater precision, (2.37) was integrated numerically in a form, due to [65], that is simpler computationally. Let $\omega = \Omega_\Lambda/\Omega_m$. By changing coordinates to $u = (2\omega)^{1/3}/(1+z')$, (2.37) becomes

$$D(z) = C(2\omega)^{2/3}(1+\omega^{-1})A\left(\frac{(2\omega)^{1/3}}{1+z}\right),$$

where

$$A(x) \equiv \left(\frac{2+x^3}{x^3}\right)^{1/2} \int_0^x \left(\frac{u}{2+u^3}\right)^{3/2} \mathrm{d}u. \tag{2.39}$$

The growth factor is calculated from

$$D(z) = \frac{A\left(\frac{(2\omega)^{1/3}}{1+z}\right)}{A\left((2\omega)^{1/3}\right)}. \tag{2.40}$$

In the special case where $\Omega_\Lambda = 0$, (2.37) can be integrated directly, giving

$$D(z) = \frac{1}{1+z} = a(z). \tag{2.41}$$

This is a very good approximation throughout most of the matter-dominated epoch.

### 2.2.3 The Power Spectrum of Linear Perturbations

In general, there are spatial correlations between perturbations at different positions. One measure of these correlations is the two-point correlation function

$$\xi(r,t) = \langle \delta_\rho(\mathbf{r}_1, t)\delta_\rho(\mathbf{r}_1 + \mathbf{r}, t)\rangle\,, \tag{2.42}$$

where the average can be taken to be over all positions $\mathbf{r_1}$ at time $t$. The fact that it depends only on the magnitude of $\mathbf{r}$ is due to the statistical uniformity and isotropy of the Universe [66]. Of particular interest is the Fourier transform of this function, called the power spectrum.

$$P(k,t) = \int \mathrm{d}^3\mathbf{r} e^{-i\mathbf{k}\cdot\mathbf{r}}\xi(r,t) \tag{2.43}$$

When calculated from perturbations that evolve according to the linear perturbation equations, the result is the linear power spectrum $P_{\mathrm{lin}}(k)$ that describes the power spectrum on linear scales.

An alternative formulation that is often cited is to determine the matter fluctuation

in momentum space

$$\tilde{\delta}_\rho(\mathbf{k},t) = \int \mathrm{d}^3\mathbf{r} e^{-i\mathbf{k}\cdot\mathbf{r}}\delta_\rho(\mathbf{r},t). \tag{2.44}$$

Note that this satisfies the same evolution equations as $\delta_\rho$. The momentum-space 2-moment is denoted and defined as

$$\left\langle \tilde{\delta}_\rho(\mathbf{k}_1)\tilde{\delta}_\rho(\mathbf{k}_2)\right\rangle \equiv \int \mathrm{d}^3\mathbf{r}_1\mathrm{d}^3\mathbf{r}_2 e^{-i(\mathbf{k}_1\cdot\mathbf{r}_1+\mathbf{k}_2\cdot\mathbf{r}_2)}\left\langle\delta_\rho(\mathbf{r}_1)\delta_\rho(\mathbf{r}_2)\right\rangle, \tag{2.45}$$

from which it follows that

$$\left\langle \tilde{\delta}_\rho(\mathbf{k}_1,t)\tilde{\delta}_\rho(\mathbf{k}_2,t)\right\rangle = (2\pi)^3\delta^{(3)}(\mathbf{k}_1+\mathbf{k}_2)P(k_1,t). \tag{2.46}$$

To get a physical sense of $P(k)$, consider the statistical variance of the density perturbations, denoted in this work as

$$\begin{aligned}\sigma_\rho^2(t) &= \langle\delta_\rho(\mathbf{r},t)\delta_\rho(\mathbf{r},t)\rangle - \langle\delta_\rho\rangle^2 = \xi(0,t)\\ &= \int \frac{\mathrm{d}^3\mathbf{k}}{(2\pi)^3}P(k,t) = \int \mathrm{d}(\ln k)\Delta^2(k,t),\end{aligned} \tag{2.47}$$

where

$$\Delta^2(k,t) \equiv \frac{k^3P(k,t)}{2\pi^2} \tag{2.48}$$

is the power per logarithmic wavenumber interval. Note that $\sigma_\rho^2$ is actually not a finite quantity, but this discussion is still meaningful when applied to smoothed fluctuations, discussed in Section 2.2.4.

During cosmological inflation, quantum fluctuations are continuously produced at microscopic scales. They are inflated to all larger scales up to the scale of total inflation, beyond the horizon $ct_U$ of the observable Universe, where $t_U$ is the age of the Universe. If inflation is uniform, the amplitude of fluctuations at all scales will be equivalent, and therefore the initial perturbations would be scale invariant. As the Universe expands, perturbations of length scales outside (i.e. larger than) the horizon will re-enter the horizon. Recalling that the Hubble length is a good estimate of the length scale of the observable Universe, the amplitude of scales

entering the horizon today are approximated by the definition

$$P(c/H_0, 0) \equiv \delta_H^2. \tag{2.49}$$

If the initial perturbations are scale invariant, then perturbations entering the horizon have the same amplitude,

$$\Delta^2(k_H, t_H) \sim \delta_H^2,$$

where $k_H$ is the wavenumber of the mode entering the horizon at time $t_H$. To estimate their relation, use the fact that the length scale associated with $k_H$ is $2\pi/k_H$. Then perturbations with wavenumber $k$ today entered the horizon at time $t_H$ given by

$$\frac{D(t_H)}{D(0)}\frac{2\pi}{k} \sim \frac{c}{H(t_H)}.$$

During the matter-dominated era, when the cosmological constant was negligible, one can substitute

$$D(t_H) = a(t_H) \propto t_H^{2/3}$$

and

$$H(t_H) = \frac{\dot{a}(t_H)}{a(t_H)} \propto \frac{2}{3}a^{-3/2}(t_H)$$

to find that

$$a\frac{2\pi}{k} \propto \frac{3}{2}ca^{3/2} \implies a(t_H) \propto k^{-2}.$$

For linear scales at time $t$ that entered the horizon during matter domination at time $t_H$, the linear power spectrum is roughly

$$\Delta^2_{\rm lin}(k,t) = \Delta^2_{\rm lin}(k,t_H)\frac{D^2(t)}{D^2(t_H)} \sim \delta_H^2\frac{a^2(t)}{a^2(t_H)} \propto \delta_H^2 a^2(t)k^4.$$

That is, $P_{\rm lin}(k) \propto k$ for scales that entered the horizon during matter domination. Before matter domination, when radiation was important, fluctuations grew slower than $a$, and did not grow at all during the radiation-dominated epoch. To take these different growth rates into account, the standard form for the linear power

spectrum with scale-invariant primordial fluctuations is

$$\Delta^2_{\rm lin}(k,t) = \delta_H^2 \left(\frac{ck}{H_0}\right)^4 T^2(k,t) D^2(t)$$

where T(k) is the transfer function that describes the evolution of the perturbations away from the initial primordial spectrum.

Inflation models can produce fluctuations that are not scale-invariant, and this creates a tilted primordial spectrum, so that

$$\Delta^2_{\rm lin}(k,t) = \delta_H^2 \left(\frac{ck}{H_0}\right)^{3+n_s} T^2(k,t) D^2(t), \tag{2.50}$$

where the tilt or spectral index $n_s$ provides a measure of deviation from scale invariance.

The transfer function has been calculated in detail. When calculating the linear power spectrum, the fitting function of [67] was used. Although neutrino streaming and gravitational wave effects are available as options in the developed computer program, they were neglected for the sample calculations shown in this document. In this case, the transfer function is time-independent and given by

$$T(k) = \left[1 + \frac{C(k_{\rm eff})}{L(k_{\rm eff})} k_{\rm eff}^2\right]^{-1}, \tag{2.51}$$

where

$$\begin{aligned} C(k) =& 14.4 + \frac{325}{1 + 60.5(k/{\rm Mpc}^{-1})^{1.11}}, \\ L(k) =& \ln\left[e + \frac{1.84\sqrt{\alpha_\nu}}{1 - 0.949 f_b}\left(\frac{k}{{\rm Mpc}^{-1}}\right)\right], \end{aligned}$$

for baryon fraction $f_b = \Omega_b/\Omega_m$. Here, the small-scale suppression factor is given by

$$\begin{aligned} \alpha_\nu =& f_c(1 - 0.4p_c)(1 - 0.553 f_b + 0.126 f_b^3)(1 + y_d)^{-p_c} \\ & \times \left[1 + \frac{p_c}{2}\left(1 + \frac{1}{7(3 - 4p_c)}\right)(1 + y_d)^{-1}\right], \end{aligned}$$

where use is made of the cold dark matter fraction

$$\begin{aligned} f_c =& \Omega_c/\Omega_m, \\ p_c =& (5 - \sqrt{1 + 24 f_c})/4, \end{aligned}$$

and $y_d = (1 + z_{\rm eq})/(1 + z_d)$ is the relative expansion between matter-radiation equality and the scale where baryons are released from the Compton drag of the photons. In terms of the cosmic microwave background temperature $T_{\rm CMB} = 2.728\ {\rm K} = 2.7\Theta_{2.7}\ {\rm K}$, the matter-radiation equality redshift is parametrized as $1 + z_{\rm eq} = 2.50 \times 10^4 \Omega_m h^2 \Theta_{2.7}^{-4}$, and the baryon release epoch is determined from the fitting function

$$\begin{aligned} z_d =& 1291 \frac{(\Omega_m h^2)^{0.251}}{1 + 0.659 (\Omega_m h^2)^{0.828}} \\ & \times \left\{ 1 + 0.313 (\Omega_m h^2)^{-0.419} \left[ 1 + 0.607 (\Omega_m h^2)^{0.674} \right] (\Omega_b h^2)^{0.238 (\Omega_m h^2)^{0.223}} \right\}. \end{aligned}$$

The scaling of the wavenumber being suppressed is

$$k_{\rm eff} = k \frac{\Theta_{2.7}^2}{\Omega_m h^2} \left[ \sqrt{\alpha_\nu} + \frac{1 - \sqrt{\alpha_\nu}}{1 + (0.43 s k)^4} \right]^{-1},$$

where the scale of the sound horizon is

$$s = \frac{44.5 \ln(9.83/\Omega_m h^2)}{\sqrt{1 + 10 (\Omega_b h^2)^{3/4}}} {\rm Mpc}.$$

### 2.2.4 Filtered Linear Variance of the Density Perturbations

A common method for considering large-scale perturbations to probe linear structure formation is to filter out, or smooth out, small perturbations by convoluting the perturbations with a filter $W_\rho(\mathbf{r}, R)$, associated with some length scale $R$, and normalized such that

$$\int {\rm d}^3 \mathbf{r} W_\rho(\mathbf{r}, R) = 1.$$

The filtered perturbations are

$$\delta_\rho(\mathbf{r}, R) = \int \mathrm{d}^3\mathbf{r}'\delta_\rho(\mathbf{r}-\mathbf{r}')W_\rho(\mathbf{r}', R), \tag{2.52}$$

and similar to (2.47), the linear variance of the filtered fluctuations on mass scale $M = 4\pi R^3 \langle\rho\rangle /3$ is

$$\sigma^2_{\mathrm{lin}}(M) = \int \mathrm{d}(\ln k)\Delta^2_{\mathrm{lin}}(k)|\tilde{W}_\rho(k, R)|^2, \tag{2.53}$$

where the Fourier transform of the filter is

$$\tilde{W}_\rho(k, R) = \int \mathrm{d}^3\mathbf{r}e^{-i\mathbf{k}\cdot\mathbf{r}}W_\rho(\mathbf{r}, R),$$

which depends only on $kR$ if $W$ depends only on $r/R$.

One commonly used filter is the tophat filter

$$W_\rho(r, R) = \frac{3}{4\pi R^3}\Theta(1 - r/R) = \begin{cases} \dfrac{3}{4\pi R^3} & \text{when } r \le R, \\ 0 & \text{when } r > R, \end{cases} \tag{2.54}$$

with

$$\tilde{W}_\rho(k, R) = \frac{3}{(kR)^3}[\sin(kR) - (kR)\cos(kR)]. \tag{2.55}$$

With this choice, $\delta_\rho(\mathbf{r}, R)$ is simply the average value of $\delta_\rho$ in a sphere of radius $R$ centered at the position $\mathbf{r}$.

An alternative to normalizing the linear power spectrum by specifying $\delta_H$ is to specify instead the parameter $\sigma_8$, defined as the linear variance filtered by a tophat of length scale $R = 8$ Mpc$/h$. Then $\delta_H$ is determined implicitly from

$$\sigma^2_8 = \int \mathrm{d}(\ln k)\Delta^2_{\mathrm{lin}}(k)\tilde{W}^2_\rho(k, 8\text{ Mpc}/h). \tag{2.56}$$

## 2.3 Toward Matter Collapse on Non-Linear Scales: Uniform Spherical Perturbations

### 2.3.1 A Spherical Collapse Solution

To gain an intuition for structure formation on non-linear scales due to gravitational collapse, it is useful to consider a toy model of an evolving uniform sphere of coordinate radius $R(t)$ containing matter with density $\rho_1(t) = \rho_m(t)[1 + \delta_1(t)]$, where $\rho_m$ is the density of the uniform background outside the sphere, and constant mass $M = (4/3)\pi R^3(t)\rho_1(t)$. Useful discussions of this model were found in [60, 68, 69]. According to Birkhoff's theorem, the dynamics of the spherical distribution at radius $R$ depends only on the matter distribution within that radius [70]. Since the matter within $R$ is isotropic and uniform, it is described by an FLRW metric (2.1)

$$\mathrm{d}s^2 = -\mathrm{d}t^2 + a_1^2(t)\left[\frac{\mathrm{d}r^2}{1-\kappa_1 r^2} - r^2\mathrm{d}\Omega^2\right]. \tag{2.57}$$

Here, $a_1(t)$ is the scale factor within the overdensity, and $\kappa_1$ is the curvature generated by the overdensity $\delta_1$ of the sphere.

The sphere's dynamics are therefore described by Friedmann's equation (2.2), assuming $R(t) \propto a_1(t)$:

$$\frac{\dot{R}^2}{R^2} = \frac{8\pi G}{3}\rho_m(1+\delta_1) + \frac{\Lambda}{3} - \frac{\kappa}{R^2}, \tag{2.58}$$

where $\kappa = \kappa_1 R^2/a_1^2$. Replacing $\delta_1$ in favor of the sphere's constant mass leads to the energy equation

$$\dot{R}^2(t) = \frac{2GM}{R(t)} + \frac{\Lambda}{3}R^2(t) - \kappa. \tag{2.59}$$

Similarly, the acceleration equation (2.3) gives

$$\ddot{R}(t) = -\frac{GM}{R^2(t)} + \frac{\Lambda}{3}R(t). \tag{2.60}$$

When collapse occurs in the matter-dominated regime, the cosmological constant is negligible, and the sphere's evolution equations are

$$\dot{R}^2(t) = \frac{2GM}{R(t)} - \kappa, \tag{2.61}$$

$$\ddot{R}(t) = -\frac{GM}{R^2(t)}. \tag{2.62}$$

From (2.61), it is seen that the overdensity stops growing and begins to collapse when it reaches a radius of

$$R_{\max} = \frac{2GM}{\kappa}. \tag{2.63}$$

This gives a physical interpretation for $\kappa$.

Solving for $GM$ in (2.62) and substituting into (2.61) results in the evolution equation

$$2R\ddot{R} + \dot{R}^2 + \kappa = 0, \tag{2.64}$$

which has the collapsing solution

$$\begin{aligned} R &= \frac{R_{\max}}{2}(1 - \cos\theta), \\ t &= \frac{t_{\mathrm{ta}}}{\pi}(\theta - \sin\theta), \end{aligned} \tag{2.65}$$

for $0 \le \theta \le 2\pi$, where $t$ is the time from when the perturbation first appeared with infinitesimal radius at $\theta = 0$, and $t_{\mathrm{ta}}$ is the turnaround time when $R = R_{\max}$, which occurs at $\theta = \pi$. Substituting the solution into (2.62),

$$-GM = R^2\ddot{R} = -\frac{\pi^2}{8}\frac{R_{\max}^3}{t_{\mathrm{ta}}^2} \implies t_{\mathrm{ta}} = \frac{\pi GM}{\kappa^{3/2}} = \frac{\pi}{2}\frac{R_{\max}}{\sqrt{\kappa}}. \tag{2.66}$$

The collapse time

$$t_c = 2t_{\mathrm{ta}} \tag{2.67}$$

occurs when $\theta = 2\pi$.

### 2.3.2 Spherical Collapse in the Linear Regime

To connect with the linearized formalism, consider the collapsing solution (2.65) in the linear regime, where $\theta \ll 1$. The $t$ equation gives

$$\begin{aligned} t &\approx \frac{t_{\rm ta}}{\pi}\frac{\theta^3}{6}\left(1-\frac{\theta^2}{20}\right) \\ \implies \theta^3 &\approx \frac{6\pi t/t_{\rm ta}}{1-(\theta^3)^{2/3}/20} \approx \frac{6\pi t/t_{\rm ta}}{1-(6\pi t/t_{\rm ta})^{2/3}/20} \approx 6\pi\frac{t}{t_{\rm ta}}\left[1+\frac{1}{20}\left(6\pi\frac{t}{t_{\rm ta}}\right)^{2/3}\right]. \end{aligned}$$

Substitute into the $R$ equation to find

$$\begin{aligned} \frac{R}{R_{\rm max}} &\approx \frac{\theta^2}{4}\left(1-\frac{\theta^2}{12}\right) \approx \frac{1}{4}\left(6\pi\frac{t}{t_{\rm ta}}\right)^{2/3}\left[1+\frac{1}{30}\left(6\pi\frac{t}{t_{\rm ta}}\right)^{2/3}\right]\left[1-\frac{1}{12}\left(6\pi\frac{t}{t_{\rm ta}}\right)^{2/3}\right] \\ &\approx \left(\frac{3\pi}{4}\frac{t}{t_{\rm ta}}\right)^{2/3}\left[1-\frac{1}{20}\left(6\pi\frac{t}{t_{\rm ta}}\right)^{2/3}\right]. \end{aligned}$$

This motivates the definition of the linear overdensity evolution

$$R_{\rm lin}(t) \equiv R_{\rm max}\left(\frac{3\pi}{4}\frac{t}{t_{\rm ta}}\right)^{2/3}\left[1-\frac{1}{20}\left(6\pi\frac{t}{t_{\rm ta}}\right)^{2/3}\right]. \tag{2.68}$$

Referring to (2.6), it is understood that the first term expresses the evolution of the background $a(t)$, whereas both terms give the linear theory expression for $a_1(t)$.

Now let $R_{\rm back}(t)$ be the radius of a sphere having the background density with the same mass $M$ as the overdense sphere. Since its evolution is determined by $a(t)$, it is given by the first term of $R_{\rm lin}(t)$.

$$R_{\rm back}^3 = \frac{3M}{4\pi\rho_m} = R_{\rm max}^3\left(\frac{3\pi}{4}\frac{t}{t_{\rm ta}}\right)^2 \tag{2.69}$$

From

$$\delta_{\rm lin} = \frac{\rho}{\rho_m} - 1 = \frac{R_{\rm back}^3}{R_{\rm lin}^3} - 1,$$

the linear overdensity is defined as

$$\delta_{\rm lin}(t) \equiv \frac{3}{20}\left(6\pi\frac{t}{t_{\rm ta}}\right)^{2/3}, \tag{2.70}$$

consistent with (2.41). The linear solution diverges from the total solution near the turnaround time, when the overdensity is

$$\delta_{\rm lin}(t_{\rm ta}) = \frac{3}{20}(6\pi)^{2/3} \approx 1.06. \tag{2.71}$$

That is, the linear theory breaks down when perturbations become of order 1.

The main result of this subsection is that the overdensity of the linear theory at the time that collapse occurs in the full solution is

$$\delta_c \equiv \delta_{\rm lin}(t_c) = \frac{3}{20}(12\pi)^{2/3} \approx 1.686. \tag{2.72}$$

This is the critical overdensity for spherical collapse. This provides an estimate of when halo virialization occurs in non-linear scales when probing only linear scales.

Doing the full calculation with $\Lambda \neq 0$ shows only slight modifications in $\delta_c$, which will be neglected [65, 71].

The value of a linear overdensity today that was critical for spherical collapse at redshift z is denoted as

$$\delta_c(z) \equiv \frac{\delta_c}{D(z)}. \tag{2.73}$$

The mass scale $M_*(z)$ for which

$$\sigma^2_{\rm lin}(M_*(z)) \equiv \delta_c^2(z), \tag{2.74}$$

with the linear mass variance given in (2.53), is defined as the characteristic mass at redshift $z$, and it represents the mass scale of modern halos that virialized at redshift $z$, in the context of the uniform collapsing sphere model.

### 2.3.3 Halo Virialization

The toy spherical model collapses to a point at the collapse time $t_c$. However, in reality, an overdensity ceases to collapse when it is supported by its constituent particles' virial motions. Combining the spherical model with the virial theorem, it is possible to determine the virial radius of the overdensity when it ceases to collapse [72].

The virial theorem states that the described dynamical equilibrium occurs in a radial potential $U \propto r^n$ if the kinetic energy of the system is $T = \frac{n}{2}U$ [73].

Consider the uniform spherical mass overdensity of radius $R$. Referring to the energy equation (2.59), the energy per unit mass of a shell of radius $r \leq R$ enclosing a mass $m = M(r/R)^3$ is

$$\varepsilon_r = \frac{1}{2}\dot{r}^2 - \frac{Gm}{r} - \frac{\Lambda}{6}r^2.$$

The mass of the shell of thickness $\mathrm{d}r$ is $\mathrm{d}m = 3Mr^2\mathrm{d}r/R^3$. Therefore, the total gravitational energy of the sphere is

$$U_G(R) = -\int \frac{Gm}{r}\mathrm{d}m = -G\int_0^R \frac{1}{r}\left(\frac{M}{R^3}r^3\right)\left(\frac{3M}{R^3}r^2\mathrm{d}r\right) = -\frac{3}{5}\frac{GM^2}{R}. \tag{2.75}$$

The total potential energy from $\Lambda$ is

$$U_\Lambda(R) = -\frac{\Lambda}{6}\int r^2\mathrm{d}m = -\frac{\Lambda}{6}\int_0^R r^2\left(\frac{3M}{R^3}r^2\mathrm{d}r\right) = -\frac{1}{10}\Lambda MR^2. \tag{2.76}$$

According to the virial theorem, the collapsing sphere will virialize (that is, reach virial equilibrium and discontinue its collapse) when

$$T_f = -\frac{1}{2}U_{G,f} + U_{\Lambda,f}. \tag{2.77}$$

All mass shells are at rest at the turnaround time, so $T_{\mathrm{ta}} = 0$. Energy conservation

relates the energies at virialization to the energies at turnaround.

$$T_f + U_{G,f} + U_{\Lambda,f} = U_{G,\mathrm{ta}} + U_{\Lambda,\mathrm{ta}} \tag{2.78}$$

Substitute (2.77) to find

$$\frac{1}{2}U_{G,f} + 2U_{\Lambda,f} = U_{G,\mathrm{ta}} + U_{\Lambda,\mathrm{ta}}.$$

Let $R_{\mathrm{vir}}$ denote the virial radius, the radius of the sphere after it virializes.

$$\frac{1}{2}\frac{3GM^2}{5R_{\mathrm{vir}}} + 2\frac{\Lambda}{10}MR_{\mathrm{vir}}^2 = \frac{3GM^2}{5R_{\mathrm{max}}} + \frac{\Lambda}{10}MR_{\mathrm{max}}^2.$$

This results in a cubic equation for $R_{\mathrm{vir}}/R_{\mathrm{max}}$

$$2\eta\left(\frac{R_{\mathrm{vir}}}{R_{\mathrm{max}}}\right)^3 - (2+\eta)\frac{R_{\mathrm{vir}}}{R_{\mathrm{max}}} + 1 = 0,$$

where $\eta \equiv \Lambda R_{\mathrm{max}}^3/(3GM) = 2\rho_\Lambda/\rho(t_{\mathrm{ta}})$ from (2.4).

For $\Lambda = 0$, the solution is simply $R_{\mathrm{vir}} = R_{\mathrm{max}}/2$. The general solution with any cosmological constant is

$$\frac{R_{\mathrm{vir}}}{R_{\mathrm{max}}} = \begin{cases} \sqrt{\frac{z}{2\eta}}(\sqrt{3}\sin\phi + \cos\phi), & \eta < \eta_0 \\ \frac{y}{2\eta} + \frac{z}{y}, & \eta_0 < \eta < 0 \\ \frac{1}{2}, & \eta = 0 \\ \sqrt{\frac{z}{2\eta}}(\sqrt{3}\sin\phi - \cos\phi), & \eta > 0, \end{cases} \tag{2.79}$$

where

$$
\begin{aligned}
z &= (2+\eta)/3, \\
y &= \left[2\eta^2\left(-1+\sqrt{1-\frac{2z^3}{\eta}}\right)\right]^{1/3}, \\
\phi &= \frac{\pi}{3}-\frac{1}{3}\cos^{-1}\sqrt{\frac{\eta}{2z^3}}, \\
\eta_0 &= -\left[2+\frac{3}{2}(4+2\sqrt{2})^{1/3}+3(4+2\sqrt{2})^{-1/3}\right] \approx -6.427.
\end{aligned}
$$

During the matter-dominated epoch when $\Lambda \approx 0$, the overdensity $\delta_{\rm ta}$ of the spherical perturbation at the turnaround time is

$$1+\delta_{\rm ta} = \frac{\rho(t_{\rm ta})}{\rho_m(t_{\rm ta})} = \frac{R^3_{\rm back}(t_{\rm ta})}{R^3_{\rm max}} = \left(\frac{3\pi}{4}\right)^2 = 5.55, \tag{2.80}$$

where (2.69) was used. At virialization, the radius is half the maximum, therefore the density increases by a factor of $2^3$.

$$\frac{\rho(t_{\rm vir})}{\rho(t_{\rm ta})} = 8 \tag{2.81}$$

The time of virialization $t_{\rm vir}$ can be found from

$$
\begin{aligned}
R(t_{\rm vir}) &= \frac{1}{2}R_{\rm max} \\
&= \frac{1}{2}R_{\rm max}(1-\cos\theta_{\rm vir}),
\end{aligned}
$$

using (2.65). Then $\theta_{\rm vir} = 3\pi/2$ and the associated virial time is

$$t_{\rm vir} = \frac{t_{\rm ta}}{\pi}(\theta_{\rm vir}-\sin\theta_{\rm vir}) = t_{\rm ta}\left(\frac{3}{2}+\frac{1}{\pi}\right) \sim 2t_{\rm ta}. \tag{2.82}$$

Since $\rho_m(t) \propto t^{-2}$ from (2.6), the background density decreased during the sphere's

collapse by a factor of

$$\frac{\rho_m(t_{\rm ta})}{\rho_m(t_{\rm vir})} = \left(\frac{t_{\rm vir}}{t_{\rm ta}}\right)^2 \sim 4. \tag{2.83}$$

Therefore, the overdensity of the perturbation at virialization is

$$1 + \delta_{\rm vir} = \frac{\rho(t_{\rm vir})}{\rho_m(t_{\rm vir})} = \frac{\rho(t_{\rm vir})}{\rho(t_{\rm ta})}\frac{\rho(t_{\rm ta})}{\rho_m(t_{\rm ta})}\frac{\rho_m(t_{\rm ta})}{\rho_m(t_{\rm vir})} \approx 8 \cdot 5.55 \cdot 4 = 178. \tag{2.84}$$

This value describes the scale of perturbation that separates virialized matter from still-collapsing matter, and is consistent with the corresponding scale observed in simulations [74].

## 2.4 Excursion Set Formalism and the Universal Halo Mass Function

The methods in Sections 2.4 and 2.5 follow the excellent review by Zentner [75], which may be referred to for additional details and developments.

The halo mass function $\frac{{\rm d}n}{{\rm d}M}(M, z)$ is defined such that the number density of halos at redshift $z$ with mass between $M$ and $M + {\rm d}M$ is

$$\frac{{\rm d}n}{{\rm d}M}(M, z){\rm d}M.$$

By dimensional analysis, this number density scales according to $\langle\rho\rangle(z)/M$. The statement of universality that is observed in the simulations is that, for any FLRW cosmology, the mass function is expressed by

$$\frac{M}{\langle\rho\rangle(z)}\frac{{\rm d}n}{{\rm d}M}(M, z){\rm d}M = f(\nu){\rm d}\nu, \tag{2.85}$$

where

$$\nu(M|z) \equiv \left(\frac{\delta_c(z)}{\sigma_{\rm lin}(M)}\right)^2 \tag{2.86}$$

is treated as a function of $M$. Here, the overdensity $\delta_c(z)$ with value today that had value $\delta_c = 1.686$ at redshift $z$ is given by (2.73), and the linear variance of

perturbations is given by (2.53). Arguments used to explain (2.85) and to determine the universal function $f$ are summarized below.

For reasons that will be made clear in Section 2.4.2, $f$ is called the first-crossing distribution. Assuming that all matter is contained within halos, the normalization condition for this distribution follows from

$$\int \mathrm{d}\nu f(\nu) = \langle\rho\rangle^{-1} \int \mathrm{d}M \frac{\mathrm{d}n}{\mathrm{d}M} M = 1. \tag{2.87}$$

### 2.4.1 The Press-Schechter Mass Function

An estimate of the mass function of collisionless structures formed from gravitational collapse was first obtained by Press and Schechter in 1974 [76], before it could be determined from N-body simulation, and before its universality was realized. They consider the matter distribution described by linear perturbations smoothed over scales $R$, according to (2.52) and (2.54). If the linear perturbations are distributed according to a Gaussian distribution, the variance is given by (2.47), and it follows that the smoothed perturbations of scale $R$ are also Gaussian with distribution

$$\mathcal{P}(\delta_{\rm lin}; R)\mathrm{d}\delta_{\rm lin} = \frac{1}{\sqrt{2\pi\sigma^2_{\rm lin}(R)}} \exp\left[-\frac{\delta^2_{\rm lin}}{2\sigma^2_{\rm lin}(R)}\right] \mathrm{d}\delta_{\rm lin}, \tag{2.88}$$

and variance (2.53).

A position $\mathbf{r}$ with $\delta_{\rm lin}(\mathbf{r}, R) = \delta_c = 1.686$, from (2.72) is taken to represent a virialized halo of mass scale

$$M(R) \equiv \frac{4}{3}\pi \langle\rho\rangle R^3. \tag{2.89}$$

Larger linear overdensities at the scale $R$ reached the critical density for spherical collapse in the past, at the redshift $z$ where $\delta_{\rm lin}(\mathbf{r}, R) = \delta_c(z) = 1.686/D(z)$. At the same position, the linear overdensity of an overdense region will generally decrease

toward 0 as the smoothing scale $R$ increases. Therefore, finding a scale $R$ where $\delta_{\rm lin}(\mathbf{r}, R) > \delta_c$ means that the position contains a halo of scale larger than $R$. Then the positions $\mathbf{r}$ of space such that $\delta_{\rm lin}(\mathbf{r}, R) > \delta_c$ are taken to represent the positions that are contained in halos larger than the smoothing scale $R$.

Let $F(M|z)$ be the fractional volume of space at redshift $z$ that is contained by halos larger than the scale $M$. It is given by the probability that each position has a greater than critical value of linear overdensity at that redshift, which is the probability that the linear overdensity today has value over $\delta_c(z)$:

$$F(M|z) = \int_{\delta_c(z)}^{\infty} \mathcal{P}(\delta_{\rm lin}; R) \mathrm{d}\delta_{\rm lin} = \frac{1}{2} \mathrm{erfc}\left(\sqrt{\frac{\nu(M|z)}{2}}\right),$$

where the complementary error function is defined by

$$\mathrm{erfc}(x) \equiv \frac{2}{\sqrt{\pi}} \int_x^{\infty} e^{-y^2} \mathrm{d}y. \tag{2.90}$$

Since $\sigma_{\rm lin}(M)$ diverges as $M \to 0$, then $\nu(0|z) = 0$, and $F(0|z) = 1/2$. However, $F(0|z)$ should include all matter, and should equal 1. This is fixed by hand, so that

$$F(M|z) = \mathrm{erfc}\left(\sqrt{\frac{\nu(M|z)}{2}}\right). \tag{2.91}$$

This factor of $1/2$ was explained in [77] by using the theory of excursion sets, summarized in Section 2.4.2.

The fractional volume of halos with mass between $M$ and $M + \mathrm{d}M$ is $-\frac{\mathrm{d}F}{\mathrm{d}M}\mathrm{d}M$, since $F$ decreases with increasing $M$. From the mass definition (2.89), these halos have volumes $V = M/\langle\rho\rangle$, so that the number density of these halos is

$$\frac{\mathrm{d}n}{\mathrm{d}M}\mathrm{d}M = -\frac{1}{V}\frac{\mathrm{d}F}{\mathrm{d}M}\mathrm{d}M = -\frac{\langle\rho\rangle}{M}\frac{\mathrm{d}F}{\mathrm{d}\nu}\mathrm{d}\nu,$$

resulting in the Press-Schechter universal halo function when comparing to (2.85):

$$f(\nu) = -\frac{\mathrm{d}F}{\mathrm{d}\nu} = \left(2\pi\nu e^{\nu}\right)^{-1/2}. \tag{2.92}$$

### 2.4.2 Press-Schechter Mass Function from Excursion Set Theory

One problem with the model presented by Press and Schechter is the so-called "cloud-in-cloud" problem [77]. It turns out to be common in realistic matter distributions to have situations where $\delta_{\rm lin}(\mathbf{r}, R) < \delta_c$ is subcritical, but is critical at some larger scale $R' > R$. For instance, if a virialized halo has an underdense patch in its interior. The Press-Schechter formalism would not identify this underdense region as being within a halo for smoothing scales of $R$ or smaller. To solve this problem, the condition for $\mathbf{r}$ to be within a halo of scale $R$ or greater should be modified to be true if $\delta_{\rm lin}(\mathbf{r}, R') \geq \delta_c$ for and $R' \geq R$. This new condition will modify the calculation of $F(M)$ from that of the Press-Schechter method.

Let $t_0$ be a time sufficiently early, such that all matter perturbations at the scales $R$ of interest have not yet approached the non-linear regime (i.e. are less than 1, in accordance with (2.71)). All overdensities are then evaluated at $t_0$ and linearly extrapolated to the present time via the linear growth factor. All coordinates are Lagrangian coordinates (coordinates moving with the perturbations, such that the perturbations are at rest in those coordinates), defined at $t_0$.

Begin with a very large scale $R_0$, such that $\sigma_{\rm lin}(M_0) \ll \delta_c$ and therefore the probability that $\delta_{\rm lin}(\mathbf{r}, R) \geq \delta_c$ for any $R \geq R_0$ is vanishingly small. At a given position $\mathbf{r}$, $R$ is decreased from $R_0$ until there is found a largest value of $R$ for which $\delta_{\rm lin}(\mathbf{r}, R) = \delta_c$, at which point the perturbation is said to cross the barrier $\delta_c$. It is necessary to calculate the probability that the scale $R$, or equvalently the filtered variance $\sigma_{\rm lin}(M)$, is where the first up-crossing of $\delta_{\rm lin}(\mathbf{r}, R)$ over the barrier $\delta_c$ occurs.

To understand the solution, it is helpful initially to consider two probability distributions. Specify the perturbation smoothing scale of radial extent $R$ or mass $M$ by the value of the filtered linear variance $S = \sigma^2_{\rm lin}(M)$ at that scale.

Let $\Pi(\delta, S|\delta_1, S_1)\mathrm{d}\delta$ be the probability of having, at a fixed position, an overdensity between $\delta$ and $\delta + \mathrm{d}\delta$ for a smoothing scale with variance $S$, given that at that

position the overdensity is $\delta_1$ for the scale with variance $S_1$. That is, $\Pi(\delta_1, S_1|\delta_1, S_1) = \delta_D(\delta_1)$, where in this section, $\delta_D(x)$ denotes the Dirac delta function. For our purposes, it will be sufficient to use the smooth Universe assumption that at very large scales, $\delta_1 = 0$ at $S_1 = 0$, though the argument follows for any prior values of $\delta_1$ and $S_1$.

Let $\Psi(\Delta\delta, \Delta S|\delta_1, S_1)\mathrm{d}(\Delta\delta)$ denote the transition probability of having overdensity between $\delta_1 + \Delta\delta$ and $\delta_1 + \Delta\delta + \mathrm{d}(\Delta\delta)$ at scale variance $S_1 + \Delta S$, given that the overdensity was $\delta_1$ at $S_1$ scale. Note that $\Psi(\Delta\delta, 0) = \delta_D(\Delta\delta)$.

These can be related with the statement: the probability density of overdensity $\delta$ with variance $S + \Delta S$ is the probability of $\delta - \Delta\delta$ at variance $S$ transitioning with changes $\Delta\delta$ and $\Delta S$, for any value of $\Delta\delta$.

$$\Pi(\delta, S + \Delta S) = \int_{-\infty}^{\infty} \mathrm{d}(\Delta\delta)\, \Pi(\delta - \Delta\delta, S)\, \Psi(\Delta\delta, \Delta S|\delta - \Delta\delta, S)$$

Considering this for infinitesimal transitions $\Delta S \to 0$ leads to an equation for $\Pi(\delta, S)$, in the following way. In the small $\Delta S$ limit, it is assumed that it is overwhelmingly probable the $\Delta\delta$ will also be small. That is, $\Psi(\Delta\delta, \Delta S)$ should be negligible for large values of $\Delta\delta$. Then we can Taylor expand $\Pi(\delta - \Delta\delta, S)$ about $\Delta\delta = 0$:

$$\begin{aligned}\Pi(\delta, S + \Delta S) \approx \int_{-\infty}^{\infty} \mathrm{d}(\Delta\delta) \left[\Pi(\delta, S) - \Delta\delta \frac{\partial \Pi(\delta, S)}{\partial \delta} + \frac{1}{2!}(\Delta\delta)^2 \frac{\partial^2 \Pi(\delta, S)}{\partial \delta^2}\right] \\ \times \Psi(\Delta\delta, \Delta S|\delta - \Delta\delta, S) \\ = \Pi(\delta, S) - \langle \Delta\delta \rangle_{\Psi}(\Delta S|\delta, S) \frac{\partial \Pi(\delta, S)}{\partial \delta} + \frac{\langle (\Delta\delta)^2 \rangle_{\Psi}(\Delta S|\delta, S)}{2} \frac{\partial^2 \Pi(\delta, S)}{\partial \delta^2},\end{aligned}$$

where the statistical moments

$$\langle (\Delta\delta)^n \rangle_{\Psi}(\Delta S|\delta, S) \equiv \int_{-\infty}^{\infty} \mathrm{d}(\Delta\delta)(\Delta\delta)^n \Psi(\Delta\delta, \Delta S|\delta - \Delta\delta, S)$$

are introduced. Neglecting higher-$n$ moments is equivalent to stating that $\Psi$ approaches a Gaussian distribution as $\Delta S \to 0$. Motivated by the fact that, in the case where a filter that is a top-hat in k-space rather than in configuration space is

applied to Gaussian fluctuations, it is strictly true that $\langle \Delta\delta \rangle_\Psi = 0$ and $\langle (\Delta\delta)^2 \rangle_\Psi = \Delta S$ for any $\Delta S$ [77], and by the argument that $\Psi$ should be independent of choice of filter in the small $\Delta S$ regime, one requires that

$$\lim_{\Delta S \to 0} \frac{\langle \Delta\delta \rangle_\Psi}{\Delta S} = 0,$$
$$\lim_{\Delta S \to 0} \frac{\langle (\Delta\delta)^2 \rangle_\Psi}{\Delta S} = 1.$$

Therefore,

$$\begin{aligned} \frac{\partial \Pi}{\partial S} &= \lim_{\Delta S \to 0} \frac{\Pi(\delta, S + \Delta S) - \Pi(\delta, S)}{\Delta S} \\ &= \lim_{\Delta S \to 0} \left[ -\frac{\langle \Delta\delta \rangle_\Psi}{\Delta S} \frac{\partial \Pi}{\partial \delta} + \frac{\langle (\Delta\delta)^2 \rangle_\Psi}{2\Delta S} \frac{\partial^2 \Pi}{\partial \delta^2} \right] \\ &= \frac{1}{2} \frac{\partial^2 \Pi}{\partial \delta^2}. \end{aligned} \tag{2.93}$$

Next, consider a modified $\Pi(\delta, S)$ distribution. Again at fixed position, let $\Pi'(\delta, S|\delta_0, S_0, \delta_c)\mathrm{d}\delta$ be the probability of the smoothed overdensity—at scale with variance $S$—having a value between $\delta$ and $\delta + \mathrm{d}\delta$, given that the overdensity is $\delta_0$ at scale $S_0$, AND that the overdensity is below the barrier $\delta_c$ for all (larger) scales with variances smaller than $S$. It follows that $\Pi'(\delta, S) = 0$ for $\delta \geq \delta_c$. For this definition of $\Pi'$, the integral relation to $\Psi$ is similar to before, but must be modified not to include values of $\Delta\delta$ for which $\delta - \Delta\delta \geq \delta_c$:

$$\Pi'(\delta, S + \Delta S) = \begin{cases} \displaystyle\int_{-\infty}^{\infty} \mathrm{d}(\Delta\delta)\, \Pi'(\delta - \Delta\delta, S)\, \Psi(\Delta\delta, \Delta S|\delta - \Delta\delta, S), & \delta < \delta_c, \\ 0, & \text{otherwise.} \end{cases}$$

Then (2.93) still holds for $\Pi'$.

Solving for $\Pi'$, take it to be a function of $\gamma \equiv \delta_c - \delta$. Applying the Fourier transform of $\Pi'(\gamma)$ to (2.93) and requiring $\Pi'(0) = 0$ gives

$$\Pi'(\gamma, S) = \int_{-\infty}^{\infty} \frac{\mathrm{d}\omega}{2\pi} A(\omega) \sin(\omega\gamma) e^{-\omega^2 S/2}$$

for some amplitude function $A(\omega)$. The other condition that the overdensity is $\delta_0$ at scale with variance $S_0$ requires

$$\Pi'(\gamma, S_0) = \delta_D(\gamma - \gamma_0) = \frac{1}{\pi}\int_{-\infty}^{\infty} \mathrm{d}\omega \sin(\omega\gamma_0)\sin(\omega\gamma)$$

with $\gamma_0 \equiv \delta_c - \delta_0$, thus fixing

$$A(\omega) = 2\sin(\omega\gamma_0)e^{\omega^2 S_0/2}.$$

The integration over $\omega$ can then be evaluated for $\Pi'$ to determine the conditional overdensity distribution

$$\Pi(\delta, S|\delta_0, S_0, \delta_c) = \begin{cases} \dfrac{1}{\sqrt{2\pi(S-S_0)}}\left\{\exp\left[-\dfrac{(\delta-\delta_0)^2}{2(S-S_0)}\right]\right. \\ \qquad\qquad \left. -\exp\left[-\dfrac{(\delta+\delta_0-2\delta_c)^2}{2(S-S_0)}\right]\right\}, & \delta < \delta_c \\ 0, & \delta \geq \delta_c. \end{cases} \tag{2.94}$$

The second term of $\Pi'$ takes into account the possibility of the overdensity crossing the barrier at some higher smoothing scale, giving us control over the cloud-in-cloud problem.

In set excursion theory, at a fixed position, a trajectory is the overdensity values $\delta(S)$ as the variance changes according to smoothing scale. The smallest variance $S$ at which the trajectory crosses the barrier $\delta_c$ determines the first-crossing scale. In a simulated distribution of matter, each position has its own trajectory $\delta(S)$.

Emulating the Press-Schechter prescription, let $F(S|\delta_0, S_0, \delta_c)$ denote the fraction of trajectories that have crossed the barrier $\delta_c$ for some scale with variance smaller than $S$, given that the trajectory crosses $\delta(S_0) = \delta_0$. Given that the fraction of trajectories that have not crossed the barrier for any variance less than $S$ is determined by

$$\int_{-\infty}^{\delta_c} \mathrm{d}\delta\Pi'(\delta, S),$$

it follows that

$$F(S) = 1 - \int_{-\infty}^{\delta_c} \mathrm{d}\delta\, \Pi'(\delta, S) = \mathrm{erfc}\left(\frac{\delta_c - \delta_0}{\sqrt{2(S - S_0)}}\right). \tag{2.95}$$

In accordance with the smooth Universe paradigm, take $\delta_0 = 0$ at $S_0 = 0$, and (2.91) is recovered.

The function $f$ in the mass function can be interpreted, in this context, to be the probablility density for the first crossing of the trajectory over the barrier at the scale of interest. It is for this reason that it is called the first-crossing distribution. The general first-crossing distribution for a perturbation at scale $S$, that had value $\delta_0$ at scale $S_0$ is

$$f(S|\delta_0, S_0)\mathrm{d}S = \frac{\mathrm{d}F}{\mathrm{d}S}\mathrm{d}S = \frac{\delta_c - \delta_0}{\sqrt{2\pi(S - S_0)^3}} \exp\left[-\frac{(\delta_c - \delta_0)^2}{2(S - S_0)}\right] \mathrm{d}S. \tag{2.96}$$

In the universal form used in Press-Schechter theory, let

$$\nu_{10}(M|z) \equiv \frac{(\delta_c(z) - \delta_0)^2}{S(M) - S_0}, \tag{2.97}$$

and note that $|f(S)\mathrm{d}S| = |f(\nu_{10})\mathrm{d}\nu_{10}|$ requires

$$f(S) = f(\nu_{10})\nu_{10}/(S - S_0). \tag{2.98}$$

Then

$$f(\nu_{10}) = [2\pi\nu_{10}e^{\nu_{10}}]^{-1/2}. \tag{2.99}$$

### 2.4.3 The Sheth-Tormen Mass Function

When the distribution of halos was considered in N-body simulations by Sheth and Tormen in 1998, they found that the universal form of the mass function (2.85)

held, but for a modified first-crossing distribution [78]

$$f(\nu) = Aa\left[1 + \frac{1}{(a\nu)^p}\right][2\pi a\nu e^{a\nu}]^{-1/2}, \tag{2.100}$$

where $a = 0.707$ and $p = 0.3$. The normalization $A$ is determined from (2.87) to be

$$\begin{aligned} A^{-1} =& \int_0^\infty \mathrm{d}(a\nu)\left[1 + \frac{1}{(a\nu)^p}\right][2\pi a\nu e^{a\nu}]^{-1/2} \\ =& \frac{2}{\sqrt{\pi}}\int_0^\infty \mathrm{d}x\, e^{-x^2} + \frac{1}{\sqrt{\pi}}2^{-p}\int_0^\infty \mathrm{d}y\, y^{(1/2-p)-1}e^{-y} \\ =& 1 + \frac{1}{2^p\sqrt{\pi}}\,\Gamma\left(\frac{1}{2} - p\right) \approx 0.3222, \end{aligned}$$

where the substitutions $x = \sqrt{a\nu/2}$ and $y = a\nu/2$ were made.

This was later explained in the context of non-spherical collapse, with a barrier consistent with ellipsoidal collapse [79]

$$\delta_{ec}(\nu|z) = \sqrt{a}\delta_c(z)\left[1 + 0.485(a\nu)^{-0.615}\right].$$

It was verified that this barrier resulted in the observed first-crossing distribution by simulations of random-walk trajectories $\delta(S)$.

### 2.4.4 The Mass Function in the Latest N-Body Simulations

Very recently, some interesting new results regarding the halo mass function were released from the Bolshoi simulation [64]. The analysis used the Bryan-Norman definition of the virial mass of halos [80]

$$M = \frac{4}{3}\pi R_{\rm vir}^3 \delta_{\rm vir}(z)\,\langle\rho\rangle(z), \tag{2.101}$$

where the virial overdensity is given by

$$\delta_{\rm vir}(z) = 18\pi^2 + 82x - 39x^2 \tag{2.102}$$

and $x = \Omega_m(z) - 1$. The virial overdensity is near 360 today, and evolves to 178 at high redshift. The analysis also modeled the halos as spherical overdensities (as they appear in our model), instead of the friends-of-friends analysis that is carried out in many works.

The analysis found that the Sheth-Tormen mass function described the mean distribution of halos very well at low redshift, but over-estimated the halos at high redshift, by a factor of 50% at redshift $z = 6$. The result is that the mass function comes to agreement, within 10% deviations, over the range of masses $5 \times 10^9 h^{-1} M_\odot$–$5 \times 10^{14} h^{-1} M_\odot$ and redshifts $z = 0$–10, if it is multiplied by the factor

$$F(z) = \frac{[5.501 D(z)]^4}{1 + [5.500 D(z)]^4}, \tag{2.103}$$

where $D(z)$ is the linear growth factor (2.37). It is advisable to use these results for immediate future work.

## 2.5 Halo Bias

The linear halo bias hypothesis supposes that the clustering of dark matter halos should follow the clustering of matter. More precisely, the overdensity of halos in a very large volume should have a general relation to the overdensity of matter within the volume, and it is supposed in the linear model that

$$\delta_h(\mathbf{r}, M, R) = b(M)\delta_\rho(\mathbf{r}, R), \tag{2.104}$$

where $R$ is the comoving radial extent of the volume under consideration, $\delta_\rho$ is the top-hat filtered overdensity in the volume, and $\delta_h$ is the relative excess of mass $M$ halos in the volume.

A scheme for determining the bias function $b(M)$ in the context of the uniform sphere collapse model and excursion set theory is due to Mo and White [81]. As before, the matter perturbations are taken to be at a sufficiently early time $t_0$, such that fluctuations are small. Consider a large spherical comoving volume $V_0$ with

radius $R_0$ and containing a total mass of $M_0 = 4\pi R_0^3 \langle\rho\rangle /3$. The variance of smoothed overdensities for such volumes is $S_0 = \sigma^2_{\rm lin}(M_0)$. The halo overdensity in the comoving volume $V_0$ is known as the Lagrangian coordinate halo overdensity $\delta_h^L$. It ignores the dynamical evolution of the overdense regions.

By the set excursion theory in Section 2.4.2, recall from (2.96) that the fraction of trajectories that first cross the barrier with mass scales having variances between $S$ and $S + \mathrm{d}S$ in the region with mass scale having variance $S_0$ and overdensity $\delta_0$ is

$$f(S|\delta_0, S_0)\mathrm{d}S = f(\nu_{10})\frac{\nu_{10}}{S - S_0}\mathrm{d}S,$$

using (2.98). Then the fraction of mass in halos with masses between $M$ and $M + \mathrm{d}M$ in the volume $V_0$ is

$$f(\nu_{10})\frac{\nu_{10}}{S - S_0}\left|\frac{\mathrm{d}S}{\mathrm{d}M}\right|\mathrm{d}M,$$

and the number of halos with that mass range in the volume is

$$\mathcal{N}(M|\delta_0, S_0)\mathrm{d}M = \frac{M_0}{M}f(\nu_{10})\frac{\nu_{10}}{S - S_0}\left|\frac{\mathrm{d}S}{\mathrm{d}M}\right|\mathrm{d}M. \tag{2.105}$$

Then the Lagrangian space halo overdensity becomes the relative excess of number of halos over the expected number from the mass function

$$\delta_h(M, R_0, \delta_0) = \frac{\mathcal{N}(M|\delta_0, S_0)}{\frac{\mathrm{d}n}{\mathrm{d}M}(M)V_0} - 1 = b^L(M)\delta_0. \tag{2.106}$$

to first order in $\delta_0$. An expression for $b^L$ by expanding $\mathcal{N}/V_0$ about $\delta_0 = 0$ and $S_0 = 0$.

$$\begin{aligned}\frac{1}{V_0}\mathcal{N}(M|\delta_0, S_0) \approx& \frac{1}{V_0}\mathcal{N}(M|0, 0) + \frac{1}{V_0}\left.\frac{\partial\mathcal{N}(M|\delta_0, 0)}{\partial\delta_0}\right|_{\delta_0=0}\delta_0 \\ =& \frac{\mathrm{d}n}{\mathrm{d}M}\left[1 + \frac{1}{\nu_{10}f(\nu_{10})}\frac{\partial[\nu_{10}f(\nu_{10})]}{\partial\nu_{10}}\left.\frac{\partial\nu_{10}}{\partial\delta_0}\right|_{\nu_{10}=\nu}\delta_0\right]\end{aligned}$$

The Lagrangian space linear bias function is therefore

$$b^L(\nu) = -\frac{2}{\delta_c(z)f(\nu)}\frac{\mathrm{d}[\nu f(\nu)]}{\mathrm{d}\nu}. \tag{2.107}$$

To get the result in Eulerian space, thereby taking into account the dynamics of the overdensity, the spherical collapse model of Section 2.3 is invoked. In Eulerian space, the region of mass $M_0$, if sufficiently overdense with respect to the background, will collapse and have a changing volume $V$. At the early time $t_0$, the overdensity is very small, and its volume $V_0$ is very nearly the volume of a region of the background with the same mass. Thus, the overdensity of the collapsing perturbation is $\delta = \rho/\langle\rho\rangle - 1 = R_0^3/R^3 - 1 = V_0/V - 1$. The halo overdensity is

$$\begin{aligned}\delta_h(M, R, \delta) =& \frac{\mathcal{N}}{\frac{\mathrm{d}n}{\mathrm{d}M}V} - 1 = \frac{\mathcal{N}}{\frac{\mathrm{d}n}{\mathrm{d}M}V_0}(1+\delta) - 1 \\ =& (1 + b^L\delta_0)(1+\delta) - 1 \approx (b^L + 1)\delta\end{aligned} \tag{2.108}$$

at large scales. Therefore, the suggestion in the literature for the linear bias function is

$$b(\nu, \delta_c) = 1 - \frac{2}{\delta_c(z)f(\nu)}\frac{\mathrm{d}[\nu f(\nu)]}{\mathrm{d}\nu}. \tag{2.109}$$

The Press-Schechter mass function (2.92) gives [81]

$$b(M, z) = 1 + \frac{\nu(M|z) - 1}{\delta_c(z)},$$

and the Sheth-Tormen mass function (2.100) gives [78]

$$b(\nu, \delta_c) = 1 + \frac{1}{\delta_c(z)}\left[\frac{2p}{1 + (a\nu)^{-p}} + a\nu - 1\right],$$

where $a = 0.707$ and $p = 0.3$, as before. However, Sheth, Mo, and Tormen later point out that the moving barrier of ellipsoidal collapse has additional effects on the halo clustering, which must be accounted for [82]. After simulating the effect of

the moving barrier, they found the linear bias is, to a very good approximation,

$$b(\nu, \delta_c) = 1 + \frac{1}{\delta_c(z)} \left[ a\nu + B(a\nu)^{1-c} - \frac{a^{-1/2}}{1 + B(1-c)(1-c/2)(a\nu)^{-c}} \right] \tag{2.110}$$

for new constants $B = 0.5$ and $c = 0.6$. This is the model that was used to describe halo clustering in this dissertation's calculations.

In a recent paper [83], these models were tested in simulations by comparing $b(M)$ directly to the ratio of halo power spectrum to matter power spectrum

$$b^2(M) = \frac{P_h(k, M)}{P(k)}, \tag{2.111}$$

which is the sense that the bias function is required to hold in this work. They also identify models using the spherical overdensity technique, according to some virial overdensity $\delta_{\rm vir}$. The Sheth-Mo-Tormen bias is found to be too high at low $\nu$, and too low at high $\nu$. A new fitting function is provided that takes into account the halo virial mass definition used

$$b(\nu, \delta_c, \delta_{\rm vir}) = 1 - A\frac{\nu^a}{\nu^a + \delta_c^a} + B\nu^b + C\nu^c, \tag{2.112}$$

where

$$\begin{aligned}
y =& \log_{10} \delta_{\rm vir}, \\
A =& 1.0 + 0.24ye^{-(4/y)^4}, \\
a =& 0.44y - 0.88, \\
B =& 0.183, \\
b =& 1.5, \\
C =& 0.019 + 0.107y + 0.19e^{-(4/y)^4}, \\
c =& 2.4.
\end{aligned}$$

## 2.6 Universal Halo Profiles

The properties of typical individual dark matter halos have been explored in N-body simulations. Large volume simulations can explore the properties of halos in large ensembles, but to limited resolution. Some recent examples are the Millennium [84] and Millennium-II [85] simulations, the Bolshoi and MultiDark simulations [86], and most recently, the Millennium-XXL simulation [87].

A method that has been employed to improve the resolution of results is to take local data from the environment of a single halo in a large simulation, and re-simulate that halo at much higher resolution, using the data of the large simulation to source the gravitational potential and incoming accreting matter at the volume boundary. Recent simulations of individual Milky-Way sized dark matter halos that have been carried are Via Lactea [88], Via Lactea II [55], GHALO [89], and the Aquarius simulations [50, 56]. The results reported from these works continue to provide justification for the techniques described in this section.

### 2.6.1 Universal Density Profiles

It was first pointed out by Navarro, Frenk, and White in 1996 that the relaxed halos in their simulations appeared to stratify their mass in a common way. They found that when the halo density was averaged over spherical shells, the halo density profile followed a universal form, consistent with [49]

$$\rho_h(r|\rho_s, r_s) = \frac{\rho_s}{\frac{r}{r_s}\left(1+\frac{r}{r_s}\right)^2}, \tag{2.113}$$

where the scale density $\rho_s$ and scale radius $r_s$ are fit parameters for each halo. This is referred to as the NFW profile.

The spherically-averaged density profile in an individual halo tends to be quite smooth in the inner regions of the halo, but is seen to fluctuate dramatically at

larger radii. This is due to the presence of halo substructures in the outer regions of the halo. However, the mean profile, averaged over large ensembles of halos, tends to be quite smooth and consistent with (2.113).

The Aquarius simulations [50] have been able to resolve to small enough scales to probe far enough to the core of simulated halos to suggest that the NFW profile is too dense at the core, but that the density profile is better described by the Einasto profile

$$\rho_h(r|\rho_{-2}, r_{-2}, \alpha) = \rho_{-2} \exp\left\{-\frac{2}{\alpha}\left[\left(\frac{r}{r_{-2}}\right)^{\alpha} - 1\right]\right\}.$$

Other profiles are also possible. Despite the disfavor of the NFW profile in the inner core, it is used in this work because it has a simple analytic form. It makes sense to attempt to calculate with more complex profiles once a working code has been developed. Also, previous works of extragalactic dark matter indirect signals have also used NFW profiles, and comparison of our work to the previous works is more direct if NFW profiles are used in initial calculations.

Another density profile that was cited by the Aquarius simulations as still being consistent with their halos is the Taylor-Navarro profile, which will be described in the next section.

### 2.6.2 Halos With Universal Pseudo-Phase-Space Density Profiles

In 2001, Taylor and Navarro found that the spherically-averaged total velocity dispersion $\sigma_u$ of dark matter at each radial position within their simulated halos was radially stratified according to

$$\frac{\rho_h(r)}{\sigma_{uh}^3(r)} \propto r^{-\alpha}. \tag{2.114}$$

They measured $\alpha = 15/8 = 1.875$, which continues to be consistent with modern simulations [50, 89].

A number of remarkable observations about this profile deserve to be highlighted. One is that, unlike the density profile, the observed pseudo-phase-space-density profile is relatively smooth in individual halos, even in the substructure-rich outer regions of the halo. Also, simulations have observed that disturbed halos settle to this stratification on relatively short time-scales, well before the halo would be considered to be relaxed based on other criteria. It is likely that the best-fit value of $\alpha$ has some variation from halo to halo, which likely depends on the merger history and local environment of the halo, and can be described by a distribution that can be estimated from simulations. The description is so good, though, that it makes sense to use (2.114), with a universal constant value of $\alpha$, as a base model from which perturbations can be implemented in future work.

When this phenomenological constraint is combined with the dynamics of a collisionless, self-gravitating system, it is possible to determine consistent pairs of solutions for the density profile $\rho_h$ and velocity variance profile $\sigma^2_{uh}$.

The phase space of a gravitating, collionless collection of massive particles in a static, isotropic density distribution satisfies the radial, spherical Jeans equation [91]

$$\frac{\mathrm{d}}{\mathrm{d}r}\left[\frac{-r^2}{G\rho_h}\left(\frac{\mathrm{d}(\rho_h\sigma^2_{uh,r})}{\mathrm{d}r}+\frac{2\beta}{r}\rho_h\sigma^2_{uh,r}\right)\right]=4\pi\rho_h r^2, \tag{2.115}$$

where $\sigma^2_{uh,r}\equiv\overline{u_r^2}-\overline{u_r}^2$ is the variance of the radial velocity component, and $\beta(r)\equiv 1-(\sigma^2_\theta+\sigma^2_\phi)/(2\sigma^2_r)$ is a measure of the velocity anisotropy, in terms of the velocity variance in polar and azimuthal spherical-tangential directions. In terms of these component variances, the total variance is

$$\sigma^2=\frac{\sigma^2_r+\sigma^2_\theta+\sigma^2_\phi}{3}. \tag{2.116}$$

In regions where

$$\left|\frac{\mathrm{d}(\rho_h\sigma^2_{uh,r})}{\mathrm{d}r}\right|\gg\frac{2|\beta|}{r}\rho_h\sigma^2_{uh,r},$$

it is a good approximation to neglect the velocity anisotropy, resulting in the

isotropic, spherical, radial Jeans equation

$$\frac{\mathrm{d}}{\mathrm{d}r}\left[\frac{-r^2}{G\rho_h}\frac{\mathrm{d}(\rho_h\sigma_{uh,r}^2)}{\mathrm{d}r}\right] = 4\pi\rho_h r^2. \tag{2.117}$$

However, this condition does not necessarily infer that $\beta \ll 1$ or $\sigma_r^2 \approx \sigma^2$. Therefore, it is more logical to use the measurement of $\sigma_r^2$ when using (2.117) to approximate a system with anisotropic velocities.

The system of equations, (2.114) with (2.117), was analyzed in detail by Dehnen and McLaughlin in 2005 [92]. The work in this dissertation considers this isotropic velocity approximation. Note that Dehnen-McLaughlin also analyzed (2.114) with (2.115) for an assumed universal velocity anisotropy profile $\beta(r)$, and the work in this dissertation can be generalized to include these effects.

Let $r_0$ be a reference radius to be precisely defined later, and let $\rho_0$ and $\sigma_0^2$ be the density and radial velocity variance, respectively, at that radius. The proportionality constant in (2.114) is written in terms of these. Combining (2.114) with (2.117) by removing $\sigma_{uh,r}$ results in an equation for the density profile that can be written in the useful form

$$\frac{\mathrm{d}\gamma}{\mathrm{d}x} - \frac{2}{3}\left(\gamma - \frac{2\alpha}{5}\right)\left(\gamma - \frac{2\alpha+3}{2}\right) = \frac{3}{5}\kappa x^{2-2\alpha/3} y^{1/3},$$

where

$$x \equiv \frac{r}{r_0}$$

is the scaled radial coordinate,

$$\gamma \equiv -\frac{\mathrm{d}(\ln\rho_h)}{\mathrm{d}(\ln r)} = -\frac{\mathrm{d}(\ln\rho_h)}{\mathrm{d}(\ln x)}$$

is the negative logarithmic density slope,

$$y \equiv \frac{\rho_h}{\rho_0} = \exp\left[-\int_{r_0}^{r}\gamma(r')\frac{\mathrm{d}r'}{r'}\right] = \exp\left[-\int_{1}^{x}\gamma(x')\frac{\mathrm{d}x'}{x'}\right]$$

is the scaled density, and

$$\kappa \equiv \frac{4\pi G \rho_0 r_0^2}{\sigma_0^2} \tag{2.118}$$

is a dimensionless parameter of the equation that specifies the scale of the velocity dispersion. There is a power-law solution $\gamma(r) = 6 - 2\alpha$ to this equation with $y = x^{-\gamma}$. It turns out that all physical solutions have radius at which the logarithmic slope takes this value. For general descriptions of the solutions of this equation, it therefore makes most sense to define the reference position by

$$\gamma(r_0) \equiv 6 - 2\alpha, \tag{2.119}$$

which can be compared to the more usual reference position found in the literature of $r_{-2}$, where $\gamma(r_{-2}) \equiv 2$.

For each value of $\alpha$, there is a family of density profiles delineated by the value of $\kappa$. For $\alpha > 35/18$, there are no solutions that describe the profiles observed in the simulations.

For $\alpha \leq 35/18$, there is one critical value of $\kappa$ for which the resulting density profile asymptotically approaches a power law at the inner halo core. It is also very similar to the NFW profile, making it consistent with the simulations. When $\alpha < 35/18$, the density cuts off at some outer radius, as the density becomes negative in the solution. The Taylor-Navarro density profile is this solution for $\alpha = 15/8$, and is shown in [50] with simulated density profiles. It has an inner logarithmic slope of $\gamma(0) = 3/4$.

When $\alpha = 35/18$, the density also asymptotically approaches a power law at large radius, and there is a closed form solution. Also, when the Aquarius simulations found the best fit value of $\alpha$ using $\sigma_r$ instead of $\sigma$, the values of $\alpha$ were more consistent with 35/18 than the value of 15/8, which is more consistent when using $\sigma$.

Therefore, the halo model used in this dissertation will assume the halos satisfy

(2.114) with

$$\alpha \equiv \frac{35}{18} \approx 1.944. \tag{2.120}$$

The NFW-like solution of the radial Jeans equation occurs for

$$\kappa = \frac{200}{81}, \tag{2.121}$$

and the critical Dehnen-McLaughlin density and velocity variance profiles are

$$\rho_h(r|\rho_0, r_0) = \frac{64\rho_0}{\left(\frac{r}{r_0}\right)^{7/9}\left[1+\left(\frac{r}{r_0}\right)^{4/9}\right]^6} \tag{2.122}$$

$$\sigma^2_{uh}(r|\sigma_0, r_0) = 16\sigma_0^2\left(\frac{r}{r_0}\right)^{-1}\left(\frac{\left(\frac{r}{r_0}\right)^{4/9}}{1+\left(\frac{r}{r_0}\right)^{4/9}}\right)^4, \tag{2.123}$$

with the constraint (2.118). The density profile has an inner logarithmic slope of $\gamma(0) = 7/9$, and an outer logarithmic slope of $\gamma(\infty) = 31/9$.

### 2.6.3 Universal Velocity Variance Profiles for Isotropic Velocity Distributions

Having already committed to working with the NFW profile, and wanting to model halos with universal pseudo-phase-space density profiles and isotropic velocity distributions, a method needed to be developed for determining a consistent velocity variance halo profile. The proposed strategy was to assume the desired density profile is a good fit to the simulated density profiles, and treat it as an approximation of the critical Dehnen-McLaughlin profile. By matching the two profiles at the reference position $r_0$, then (2.114) can be used to determine $\sigma^2_{uh}(r)$.

This process will now be demonstrated for the NFW profile (2.113), but can be applied to any other density profile, such as the Einasto profile. It is convenient for the NFW profile to define the constant

$$\beta \equiv \frac{2}{3}(\alpha - 1) = \frac{17}{27}, \tag{2.124}$$

the physical significance of which will become apparent.

Given an NFW profile with particular values of $\rho_s$ and $r_s$, first use (2.119) to determine the reference radius $r_0$.

$$\gamma(r_0) = 1 + \frac{2}{1+\frac{r_s}{r_0}} \equiv 6 - 2\alpha = 4 - 3\beta \implies r_0 = \frac{\frac{5}{2}-\alpha}{\alpha-\frac{3}{2}} r_s = \frac{1-\beta}{\beta-\frac{1}{3}} r_s \tag{2.125}$$

Use this result to determine the reference density.

$$\rho_0 = \rho_h(r_0) = \rho_s \left(\frac{r_0}{r_s}\right)^{-1} \left(1+\frac{r_0}{r_s}\right)^{-2} = \frac{\left(\alpha-\frac{3}{2}\right)^3}{\frac{5}{2}-\alpha}\rho_s = \frac{9\left(\beta-\frac{1}{3}\right)^3}{4(1-\beta)}\rho_s \tag{2.126}$$

Finally, determine the reference velocity variance from (2.118).

$$\sigma_0^2 = \frac{4\pi G}{\kappa}\rho_0 r_0^2 = \frac{4\pi G}{\kappa}\left(\alpha-\frac{3}{2}\right)\left(\frac{5}{2}-\alpha\right)\rho_s r_s^2 = \frac{9\pi G}{\kappa}\left(\beta-\frac{1}{3}\right)(1-\beta)\rho_s r_s^2 \tag{2.127}$$

Then the phase space density profile

$$\frac{\rho_h/\rho_0}{(\sigma_{uh}/\sigma_0)^3} = \left(\frac{r}{r_0}\right)^{-\alpha}$$

gives

$$\sigma_{uh}^2(r) = \sigma_0^2\left[\left(\frac{r}{r_0}\right)^{\alpha}\frac{\rho_h(r)}{\rho_0}\right]^{2/3} = \sigma_0^2\left(\frac{r_s}{r_0}\right)^{2\alpha/3}\left(\frac{\rho_s}{\rho_0}\right)^{2/3}\left(\frac{r}{r_s}\right)^{2(\alpha-1)/3}\left(1+\frac{r}{r_s}\right)^{-4/3}.$$

If the NFW scale variance is defined as

$$\sigma_s^2 \equiv \sigma_0^2\left(\frac{r_s}{r_0}\right)^{\beta+2/3}\left(\frac{\rho_s}{\rho_0}\right)^{2/3},$$

then the suggested NFW velocity variance profile is

$$\sigma_{uh}^2(r|\sigma_s^2, r_s) = \frac{\sigma_s^2\left(\frac{r}{r_s}\right)^{\beta}}{\left(1+\frac{r}{r_s}\right)^{4/3}}, \tag{2.128}$$

where

$$\sigma_s^2 = \frac{12^{2/3}\pi G}{\kappa}\left(\beta - \frac{1}{3}\right)^{\beta-1/3}(1-\beta)^{1-\beta}\rho_s r_s^2. \tag{2.129}$$

The physical significance of $\beta$ is now seen to be the inner logarithmic slope of $\sigma_{uh}^2$.

### 2.6.4 Universal Mean Square Relative Velocity Profiles in the Absence of Flows

The mean square relative particle velocity at a position derives directly from the velocity variance there [93]. With the relative velocity between two particles having velocities $\mathbf{u}_1$ and $\mathbf{u}_2$ denoted as $\mathbf{v} = \mathbf{u}_1 - \mathbf{u}_2$, the mean square relative velocity is

$$\overline{v^2} = \overline{(\mathbf{u}_1 - \mathbf{u}_2)^2} = \overline{\mathbf{u}_1^2} + \overline{\mathbf{u}_2^2} - 2\overline{\mathbf{u}_1 \cdot \mathbf{u}_2}.$$

In the absence of flows,

$$\overline{\mathbf{u}_1 \cdot \mathbf{u}_2} = 0,$$

and $\overline{\mathbf{u}_1} = 0$, implying

$$\overline{\mathbf{u}_1^2} = \sigma_{u_1,r}^2 + \sigma_{u_1,\theta}^2 + \sigma_{u_1,\phi}^2 = 3\sigma_u^2,$$

from (2.116). Therefore,

$$\overline{v^2} = 6\sigma_u^2. \tag{2.130}$$

One can then determine a universal mean-relative-velocity halo profile, denoted as

$$v_h(r) = \lambda\sigma_{uh}^2(r), \tag{2.131}$$

where $\lambda$ is a new constant parameter introduced in the model. For calculations requiring a value of $\lambda$, it is always set to 6. Different values can be used to model effects of velocity anisotropies, or net dark matter flows. Since dark matter flows are a significant phase space substructure in halo simulations, it is important to add them to this model in future work undertaken, for the viability of the methods of calculating indirect detection signals described in Section 4.

## 2.7 Simplest Halo Model with Rigid, Disjoint, Spherical Halos and Linear Bias

A halo model consists of a description of the point distribution of halos at each redshift, distributed by position and any halo variables required to specify the properties of the halo. The model also requires specification of the universal properties of the halos, dependent on the halo variables at each redshift. Developed in this section is the simplest halo model of large scale structure, where the only halo variable that the halo properties depend on is the halo mass $M$.

### 2.7.1 The Halo Point Distribution

At redshift $z$, the distribution of an ensemble of $N_h$ halos with masses $M_i$ and positions $R_i$, specified by a global set of coordinates at that redshift, is

$$p_h(\mathbf{r}, M, z) = \sum_{i=1}^{N_h(z)} \delta^{(3)}(\mathbf{r} - \mathbf{R}_i(z))\delta(M - M_i(z)), \tag{2.132}$$

where $\mathbf{r}$ is a position according to the same set of coordinates used to describe the halo positions at redshift $z$. In the statistical description of large scale structure, the halo positions and masses are stochastic variables. The ensemble average of the halo distribution is independent of position, because of the statistical uniformity of the Universe, and is precisely the halo mass function described in Section 2.4.

$$\langle p_h \rangle (M, z) = \frac{\mathrm{d}n}{\mathrm{d}M}(M, z) \tag{2.133}$$

Formally, the halo overdensity is then defined as

$$\delta_h(\mathbf{r}, M, z) \equiv \frac{p_h(\mathbf{r}, M, z)}{\frac{\mathrm{d}n}{\mathrm{d}M}(M, z)} - 1. \tag{2.134}$$

In practice, it is usual to consider this function averaged over fixed volumes.

Collectively, the connected $n$-point halo correlation functions

$$\tilde{\xi}^{(n)}_{hc}(\mathbf{r}_1, \mathbf{r}_2, \ldots, \mathbf{r}_n, M_1, M_2, \ldots, M_n, z) = \langle \delta_h(\mathbf{r}_1, M_1, z)\delta_h(\mathbf{r}_2, M_2, z)\cdots\delta_h(\mathbf{r}_n, M_n, z)\rangle_c$$

fully specify the halo statistics at redshift $z$, for positions $\mathbf{r}_i$ at that redshift. The angular power spectrum of dark matter annihilation products requires knowledge of the $n = 2$ halo statistics, described below:

The full halo correlation function

$$\tilde{\xi}_h(\mathbf{r}_1, \mathbf{r}_2, M_1, M_2, z) = \langle \delta_h(\mathbf{r}_1, M_1, z)\delta_h(\mathbf{r}_2, M_2, z)\rangle \tag{2.135}$$

has a singularity at $\mathbf{r}_1 = \mathbf{r}_2$. This can be seen by applying (2.134)

$$\tilde{\xi}_h(\mathbf{r}_1, \mathbf{r}_2, M_1, M_2, z) = \frac{\langle p_h(\mathbf{r}_1, M_1, z)p_h(\mathbf{r}_2, M_2, z)\rangle}{\frac{\mathrm{d}n}{\mathrm{d}M}(M_1, z)\frac{\mathrm{d}n}{\mathrm{d}M}(M_2, z)} - 1, \tag{2.136}$$

and separating the halo distribution 2-moment into diagonal (1-halo) and non-diagonal (2-halo) pieces.

$$\begin{aligned}
&\langle p_h(\mathbf{r}_1, M_1, z)p_h(\mathbf{r}_2, M_2, z)\rangle \\
&\quad= \left\langle \sum_{i=1}^{N_h}\sum_{j=1}^{N_h} \delta^{(3)}(\mathbf{r}_1 - \mathbf{R}_i)\delta(M_1 - M_i)\delta^{(3)}(\mathbf{r}_2 - \mathbf{R}_j)\delta(M_2 - M_j)\right\rangle \\
&\quad= \left\langle \sum_{i}\sum_{j\neq i} \delta^{(3)}(\mathbf{r}_1 - \mathbf{R}_i)\delta(M_1 - M_i)\delta^{(3)}(\mathbf{r}_2 - \mathbf{R}_j)\delta(M_2 - M_j)\right\rangle \\
&\qquad+ \left\langle \sum_{i} \delta^{(3)}(\mathbf{r}_1 - \mathbf{R}_i)\delta(M_1 - M_i)\delta^{(3)}(\mathbf{r}_2 - \mathbf{R}_i)\delta(M_2 - M_i)\right\rangle \\
&\quad= C^{(2)}_h(\mathbf{r}_1, M_1, \mathbf{r}_2, M_2, z) + \delta^{(3)}(\mathbf{r}_1 - \mathbf{r}_2)\delta(M_1 - M_2)\frac{\mathrm{d}n}{\mathrm{d}M}(M_2, z)
\end{aligned}$$

This expression makes the singularity explicit. Here, the function

$$C_h^{(2)}(\mathbf{r}_1, M_1, \mathbf{r}_2, M_2, z) \equiv \left\langle \sum_i \sum_{j \neq i} \delta^{(3)}(\mathbf{r}_1 - \mathbf{R}_i)\delta(M_1 - M_i)\delta^{(3)}(\mathbf{r}_2 - \mathbf{R}_j)\delta(M_2 - M_j) \right\rangle \quad (2.137)$$

is introduced as the non-diagonal part of the halo 2-moment. In disjoint ensembles where no 2 halos can be at the same position, $C_h^{(2)} = 0$ when $\mathbf{r}_1 = \mathbf{r}_2$. The non-diagonal part of the full halo correlation function is what is normally referred to as the halo correlation function, and it can be defined as

$$\xi_h(\mathbf{r}_1, \mathbf{r}_2, M_1, M_2, z) \equiv \frac{C_h^{(2)}(\mathbf{r}_1, M_1, \mathbf{r}_2, M_2, z)}{\frac{\mathrm{d}n}{\mathrm{d}M}(M_1, z)\frac{\mathrm{d}n}{\mathrm{d}M}(M_2, z)} - 1, \quad (2.138)$$

so that

$$\tilde{\xi}_h(\mathbf{r}_1, \mathbf{r}_2, M_1, M_2, z) = \xi_h(\mathbf{r}_1, \mathbf{r}_2, M_1, M_2, z) + \frac{\delta^{(3)}(\mathbf{r}_1 - \mathbf{r}_2)\delta(M_1 - M_2)}{\frac{\mathrm{d}n}{\mathrm{d}M}(M_1, z)}. \quad (2.139)$$

The halo power spectrum is defined accordingly as

$$P_h(k, M_1, M_2, z) \equiv \int \mathrm{d}^3\mathbf{r} e^{-i\mathbf{k}\cdot\mathbf{r}} \xi_h(\mathbf{r}_1, M_1, \mathbf{r}_1 + \mathbf{r}, M_2, z). \quad (2.140)$$

Its correlation to the matter power spectrum is encoded in the halo bias function. For our purposes, the precise meaning of the halo bias is through the relation

$$P_h(k, M_1, M_2, z) = b(M_1, z)b(M_2, z)P(k, z). \quad (2.141)$$

For extragalactic annihilation signals of dark matter, the properties of the point distribution of halos that are required are the halo mass function and the linear halo bias function. The sample calculations carried out used the Sheth-Tormen mass function (2.100) with (2.85), and the associated Sheth-Mo-Tormen bias function (2.110).

### 2.7.2 Universal Halo Profiles in the Halo Model

What remains, in order to specify the halo model, is to define the individual halo properties as functions of halo redshift and the other universal halo variables. For our purposes, the halo density and velocity variance profiles are specified in terms of the halo mass and redshift, $\rho_h(r|M,z)$ and $\sigma^2_{uh}(r|M,z)$.

Unfortunately, the mass of a halo described by the NFW profile (2.113) is ill-defined, since its radial integration diverges. This issue is normally addressed by defining a virial radius $R_{\rm vir}$ for the halo, beyond which the density is negligible:

$$\rho_h(r|\rho_s, r_s, R_{\rm vir}) = \frac{\rho_s}{\frac{r}{r_s}\left(1+\frac{r}{r_s}\right)^2}\,\Theta(R_{\rm vir}-r), \tag{2.142}$$

where

$$\Theta(x) = \begin{cases} 1, & x > 0 \\ 0, & x < 0 \end{cases}$$

is the Heaviside step function. The definition of virial radius simultaneously defines the halo virial mass $M = 4\pi\int_0^{R_{\rm vir}} \rho_h(r) r^2 {\rm d}r$.

There are many different virial mass-radius relations used for halos in the literature. Motivated by the analysis of Martin White [94], which suggested that the Sheth-Tormen mass function is especially consistent with simulations for the mass-radius relation of the constant-density perturbation when it virializes (2.84), the outer boundary $R_{\rm vir}$ of the halo is defined to be where the enclosed halo mass $M$ satisfies

$$M \equiv \frac{4}{3}\pi R^3_{\rm vir}\delta_{\rm vir}\,\langle\rho\rangle(z) \tag{2.143}$$

for $\delta_{\rm vir} \equiv 180$.

Given an NFW halo with scale density $\rho_s$ and scale radius $r_s$, its concentration is defined as

$$c \equiv \frac{R_{\rm vir}}{r_s}. \tag{2.144}$$

The scale radius can then be replaced in favor of the halo mass, redshift, and concentration.

$$r_s(M,z,c) = \frac{1}{c}\left(\frac{3M}{4\pi\delta_{\rm vir}\,\langle\rho\rangle(z)}\right)^{1/3} \tag{2.145}$$

The halo mass satisfies (letting $x = r/R_{\rm vir} = r/(cr_s)$)

$$\begin{aligned} M =& 4\pi\int_0^{R_{\rm vir}} \rho_h(r) r^2 {\rm d}r = 4\pi\rho_s r_s^3 c^3 \int_0^1 \frac{x^2 {\rm d}x}{cx(1+cx)^2} \\ =& 4\pi\rho_s r_s^3 \int_0^1 \left[\frac{c}{1+cx} - \frac{c}{(1+cx)^2}\right] {\rm d}x \\ =& 4\pi\rho_s r_s^3 \left[\ln(1+cx) + \frac{1}{1+cx}\right]_{x=0}^{x=1} \\ =& 4\pi\rho_s r_s^3 \left[\ln(1+c) - \frac{c}{1+c}\right]. \end{aligned}$$

Substituting (2.145) for the scale radius, the scale density becomes expressed as

$$\rho_s(z,c) = \frac{\delta_{\rm vir}\,\langle\rho\rangle(z)}{3}\frac{c^3}{\left[\ln(1+c) - \frac{c}{1+c}\right]}. \tag{2.146}$$

Using these results with (2.129) determines the NFW scale velocity variance $\sigma_s^2(M,z,c)$.

It appears that spherical NFW halos require two halo variables to be specified: the halo mass, and the halo concentration. While halos of a given mass and redshift do appear to have a distribution of concentrations that is consistent with a log-normal distribution [95], this distribution can be approximated as a Dirac delta function. The mean concentration $\langle c\rangle(M,z)$ does scale with halo mass and redshift. If this scaling is understood, then the halo profiles used in the halo model are

$$\begin{aligned} \rho_h(r|M,z) &= \rho_h\Big(r\Big|\rho_s(z,c), r_s(M,z,c), R_{\rm vir}(M,z)\Big)\Big|_{c=\langle c\rangle(M,z)}, \\ \sigma_{uh}^2(r|M,z) &= \sigma_{uh}^2\Big(r\Big|\sigma_s^2(M,z,c), r_s(M,z,c), R_{\rm vir}(M,z)\Big)\Big|_{c=\langle c\rangle(M,z)}. \end{aligned}$$

### 2.7.3 Mean Halo Concentration Distribution

In this section, the spread of concentration values are not considered, and the mean concentration $\langle c \rangle (M, z)$ will be denoted only as $c(M, z)$. In the finite resolution of N-body cosmological simulations, the concentrations of halos are able to be probed over typical halo mass ranges of $10^{10} M_\odot \lesssim M \lesssim 10^{15} M_\odot$, and tend to be well-fitted by functions of the form

$$c(M, z) \approx \frac{a}{1+z} \left( \frac{M}{10^{12} h^{-1} M_\odot} \right)^b,$$

or

$$c(M, z) \approx \frac{a}{1+z} \left( \frac{M}{M_*(z)} \right)^b$$

for different constants $a$ and $b$, where the characteristic mass was defined in (2.74). These scalings are not expected to hold down to lower mass scales beyond the simulation resolution, and are not appropriate for extrapolating to low halo mass.

A physical model of concentrations was provided by NFW [49], based on the excursion set formalism. Their development was as follows. Consider a halo of mass $M$ at redshift $z = 0$. That is, the smoothed overdensity at the halo's position with scale $M$ and variance $S_0 = \sigma^2(M)$ is critical to spherical collapse $\delta_0 = \delta_c$.

Define the collapse redshift $z_c(M, f)$ to be the time when half of the mass of the halo was first contained in progenitors $M_i$ with $M_i > fM$ for a fixed fraction $f < 1$. Then, according to the excursion set formalism, with reference to (2.96), $z_c$ satisfies

$$\begin{aligned} \int_{fM}^{\infty} \mathrm{d}S \, f(S|\delta_0, S_0) =& \operatorname{erfc} \left[ \frac{\delta_c(z_c) - \delta_c}{\sqrt{2[\sigma^2(fM) - \sigma^2(M)]}} \right] = \frac{1}{2} \\ \implies & \delta_c(z_c) = \delta_c + C' \sqrt{\sigma^2(fM) - \sigma^2(M)}, \end{aligned} \tag{2.147}$$

where $C' \equiv \sqrt{2} \operatorname{erfc}^{-1}(1/2) \approx 0.67449$.

Best fits to the data were achieved for $f \ll 1$. In this regime, $\sigma^2(fM) \gg \sigma^2(M)$,

and hence $\delta_c(z_c) \gg \delta_c$. Then

$$\delta_c(z_c) \approx C'\sigma(fM), \quad f \ll 1,$$

resulting in

$$\sigma(M_*(z_c)) \approx C'\sigma(fM)$$

in terms of the characteristic mass $M_*$ in (2.74), or within an order of magnitude,

$$M_*(z_c) \approx fM. \tag{2.148}$$

This shows that, in this model, collapse occurs at a time when the characteristic mass is a small fraction of the final halo mass. The main assumption of the NFW concentration model is

$$\rho_s(M, f) = C \langle\rho\rangle (z_c(M, f)) \tag{2.149}$$

for proportionality constant $C$, and $\rho_s$ is the NFW scale density of the halo with mass $M$. The analysis of this model used the 200c definition of halo mass

$$M_{200} = \Delta_c \rho_c(z) \frac{4\pi}{3} R_{200}^3 = \int_0^{R_{200}} 4\pi\rho(r|\rho_s, r_s) r^2 \mathrm{d}r,$$

where $\Delta_c = 200$. The concentration is $c = R_{200}/r_s$, and the mass definition gives

$$\frac{\Delta_c \rho_c(z)}{3\rho_s} = \frac{\ln(1+c) - \frac{c}{1+c}}{c^3}.$$

When combined with (2.149), it is found that the concentration in this model is given implicitly by

$$\frac{c^3}{\ln(1+c) - \frac{c}{1+c}} = \frac{3C\Omega_m(z)[1 + z_c(M, f)]^3}{\Delta_c} \tag{2.150}$$

for mass $M$ halos at redshift $z$. The best fit with the N-body simulations of NFW (which used $\Omega_m = 0.25$, $\Omega_\Lambda = 0.75$, $h = 0.75$, and $\sigma_8 = 1.3$) had $f = 0.01$ and $C = 3410$. This model is now known to over-predict the concentration of halos at early times.

An improvement was proposed by Bullock, *et al.* [95]. Their analysis defined spherical halos with the Bryan-Norman virial mass (2.102). The model contains two axioms. First, the definition of the collapse redshift $z_c(M)$ of a mass $M$ halo is modified to be given precisely by (2.148) for a small proportionality constant $F \ll 1$.

$$M_*(z_c) \equiv FM \tag{2.151}$$

From the definition of the characteristic mass (2.74), this is equivalent to $\nu(FM|z_c) = 1$, using (2.86), or in terms of the linear growth factor,

$$D(z_c) = \frac{\delta_c}{\sigma_{\rm lin}(FM)}, \tag{2.152}$$

where $\delta_c = 1.686$ is assumed, as usual. The second axiom is to assume that

$$\frac{M}{\frac{4}{3}\pi r_s^3} \equiv K^3 \delta_{\rm vir}(z) \langle\rho\rangle(z_c) = K^3 \delta_{\rm vir}(z) \langle\rho\rangle(z) \left(\frac{1+z_c}{1+z}\right)^3. \tag{2.153}$$

Using the definition of the virial mass of a halo observed at redshift $z$,

$$\frac{M}{\frac{4}{3}\pi r_s^3} = \delta_{\rm vir}(z) \langle\rho\rangle(z) \left(\frac{R_{\rm vir}}{r_s}\right)^3 = \delta_{\rm vir}(z) \langle\rho\rangle(z) c^3,$$

then the halo concentration is given by

$$c(M, z|F, K) = K \frac{1+z_c(M|F)}{1+z}. \tag{2.154}$$

This model fits much of the simulation data for $K \approx 4$ and $F \approx 0.01$.

As is pointed out in the original paper, this model underestimates the concentrations of the highest mass halos (see also [96]). That is because the model has a hard cutoff where halo concentration vanishes at a maximum halo mass, characterized as having a collapse redshift of -1

$$M_{\rm max} = \frac{M_*(-1)}{F}, \tag{2.155}$$

or equivalently

$$\sigma_{\rm lin}(FM_{\rm max}) = \delta_c(-1) = \frac{\delta_c}{D(-1)}. \tag{2.156}$$

Using WMAP5 cosmological parameters [11], $M_{\rm max} = 2.03 \times 10^{15} M_\odot$.

This is the concentration distribution that was used for the sample calculations later in this dissertation, which introduced an upper halo mass to the model. When integrating over the halo masses, care was required when integrating near the maximum mass in order for the numerical integrator to be stable and converge to the required precision. Knowledge of the analytic structure of $c(M, z)$ near $M = M_{\rm max}(z)$ was very useful and I will summarize some of the unpublished results here. First, determine the asymptotic linear growth factor. From (2.40),

$$D(z) = \frac{A\left(\frac{1}{\xi(z)}\right)}{A\left(\frac{1}{\xi(0)}\right)},$$

after defining

$$\xi(z) \equiv \frac{1+z}{(2\omega)^{1/3}}$$

with $\omega = \Omega_\Lambda/\Omega_m$. Also define

$$A_\infty \equiv A(\infty) = \int_0^\infty \left(\frac{u}{2+u^3}\right)^{3/2} {\rm d}u = \frac{\Gamma\left(\frac{5}{6}\right)\Gamma\left(\frac{5}{3}\right)}{2^{2/3}\sqrt{\pi}} \approx 0.36217.$$

The asymptotic expansion

$$\begin{aligned}\int_0^x \left(\frac{u}{2+u^3}\right)^{3/2} {\rm d}u =& A_\infty - \int_0^{\frac{1}{x}} \frac{t}{(1+t^3)^{3/2}} {\rm d}t \\ =& A_\infty - \frac{1}{2x^2} + \frac{3}{5x^5} - \frac{15}{16x^8} + \mathcal{O}(x^{-11})\end{aligned}$$

can be multiplied by $\sqrt{1+2x^{-3}}$ and expanded to find

$$A\left(\frac{1}{\xi}\right) = A_\infty - \frac{1}{2}\xi^2 + A_\infty \xi^3 + \frac{A_\infty}{2}\xi^6 - \frac{7}{80}\xi^8 + \mathcal{O}(\xi^9). \tag{2.157}$$

Next, let $\Delta(M)$ denote the relative linear growth of a newly collapsed halo of mass

$M$, relative to its asymptotic future growth

$$\Delta(M) \equiv 1 - \frac{D(z_c)}{D(-1)}. \tag{2.158}$$

Then $\Delta(M_{\rm max}) = 0$, and this is a perturbative quantity near maximum halo mass. Using (2.152) and (2.156), $\Delta(M)$ is most conveniently calculated as

$$\Delta(M) = 1 - \frac{\delta_c}{D(-1)\sigma_{\rm lin}(FM)} = 1 - \frac{\sigma_{\rm lin}(FM_{\rm max})}{\sigma_{\rm lin}(FM)}. \tag{2.159}$$

Defining

$$\xi_c(M) \equiv \xi(z_c(M)) = \frac{1 + z_c(M))}{(2\omega)^{1/3}} = \frac{K}{(2\omega)^{1/3}}(1+z)c(M,z), \tag{2.160}$$

then an expansion for $\Delta(M)$ near $M = M_{\rm max}$ is

$$\Delta = 1 - \frac{D(z_c)}{D(-1)} = 1 - \frac{A(\xi^{-1})}{A_\infty} = \frac{1}{2A_\infty}\xi_c^2 - \xi_c^3 - \frac{1}{10A_\infty}\xi_c^5 + \mathcal{O}(\xi_c^6).$$

Reversing the series to expand $\xi_c$ in $\Delta$, and using (2.160) to replace $\xi_c$ in favor of $c$ gives the desired expansion

$$c(M,z) = \frac{K(2\omega)^{1/3}}{1+z}\left[\sqrt{2A_\infty\Delta(M)} + 2A_\infty^2\Delta(M) + 5\sqrt{2A_\infty^7\Delta^3(M)} + \frac{2}{5}A_\infty^2(1+80A_\infty^3)\Delta^2(M) + \mathcal{O}(\Delta^{5/2}(M))\right]. \tag{2.161}$$

As with other aspects of the halo model, there is some very recent progress on the distribution of halo concentrations from the latest simulations that should be applied to future work. It is found in the Bolshoi simulation [64] that the redshift dependence is not quite like $(1+z)^{-1}$, but is well fit by

$$c(M,z) = c(M,0)\left[D^{4/3}(z) + \kappa(M)\left(D^{-1}(z) - 1\right)\right]. \tag{2.162}$$

where $\kappa(M)$ was found to be 0.084 for $M = 3 \times 10^{11}h^{-1}M_\odot$ and 0.135 for $M = 3 \times 10^{12}h^{-1}M_\odot$.

A more complete concentration profile is provided by [97], based on data from the Bolshoi and MultiDark simulations. Motivated by the form of the Sheth-Tormen mass function, a curve as a function of $\sigma(M)$ was found, and a fitting function for the full rms matter fluctuation, from [64], is also provided.

### 2.7.4 Minimum Halo Mass

One more input into the halo model is the minimum mass $M_{\rm min}$ of dark matter halos. For a thermal dark matter WIMP in the standard cosmology, there are two effects that wash out small-scale structures: particle free-streaming, and acoustic oscillations.

The mass scale at which each of these suppresses the power spectrum is dependent on the dark matter's kinetic decoupling temperature, at which the dark matter relic's temperature begins to deviate from the temperature of the background. However, the free-streaming cutoff scale also depends on the dark matter particle mass, whereas the mass of the smallest surviving structures of acoustic oscillations depends on the effective relativistic degrees of freedom, and is thus more efficient at higher decoupling temperatures.

Scans of supersymmetric neutralino dark matter parameter space show that either effect may determine the minimum halo mass scale, and the models accomodate $10^{-10} M_\odot \lesssim M_{\rm min} \lesssim 10^{-3} M_\odot$ [98]. Therefore, the halo mass cutoff provides a window into the constraint of the particle interaction properties of dark matter, and should be fixed consistently with the particle model being considered. For the sample calculations in this dissertation, the minimum halo mass is set to a constant value by hand.

Other recent papers look at other effects on the minimum halo mass, including the streaming of baryons at the time of recombination [99], and effects from a reheating epoch [100].

### 2.7.5 Halo Substructure

It is quite probable that the largest neglected effect in the sample calculations carried out below is the presence of halo substructure. N-body simulations predict that dark matter halos contain an abundant population of subhalos, sub-subhalos, etc. [55, 56, 88, 89]. The subhalo mass function in these simulations is consistent with

$$\frac{\mathrm{d}N}{\mathrm{d}M_{\mathrm{sub}}} \propto M_{\mathrm{sub}}^{-1.90}$$

down to the simulation resolutions. The subhalos have density profiles consistent with NFW profiles, but they are generally more concentrated than halos of the same mass. This can be accounted for by tidal stripping of the subhalo as it merges with the parent halo.

Different analytic approaches for accounting for substructure in indirect detection annihilation signals have been independently developed [101], allowing for different methods to estimate the substructure effects.

Since the intensity of dark matter annihilation scales with the square density of the annihilating region (as explained in Section 4), a population of densely-cored substructures within a halo can dramatically increase the overall annihilation intensity of the halo. If observing from within the halo, the substructure annihilations are dispersed throughout the field of view. Therefore, it is unlikely that the substructures within the galactic halo would increase the intensity of annihilations from within the halo by more than a factor of a few. However, substructures in an extragalactic halo can have a dramatic coherent effect on the halo's annihilation intensity, and for Milky Way sized halos, could increase the intensity by a factor on the order of 100 [102]. Clearly, this is an important effect to be modeled, and the consequences and constraints of different halo substructure models need to be understood in future work.

## 2.8 General Matter Distribution Results from the Spherical Halo Model

The spherical halo model allows for elementary calculation and prediction of statistical measures of the large scale structure on all scales [103], such as the power spectrum, matter variance of fluctuations, bispectrum, trispectrum, and so on. Comparison of these results with the N-body simulations guides how this semi-analytic model should be used in serious work.

The mean density profile of the Universe was used as a constraint in the model to normalize the halo mass function in (2.87). However, the new velocity variance profiles allow the mean vlocity variance of the Universe to be calculated at each redshift as a model prediction.

$$\left\langle \sigma_u^2 \right\rangle(z) = \int \mathrm{d}^3\mathbf{r}\mathrm{d}M \frac{\mathrm{d}n}{\mathrm{d}M}(M,z)\sigma_{uh}^2(r|M,z) \tag{2.163}$$

This is shown in Figure 3 for a cosmology with $\Omega_\Lambda = 0.721$, $\Omega_b = 0.0462$, $\Omega_c = 1 - \Omega_\Lambda - \Omega_b$, $h = 0.701$, $\sigma_8 = 0.817$, $n_s = 0.96$, and $M_{\min} = 10^6 M_\odot$. Inclusion of smaller halo masses have negligible effect on the result. In this model of distributed velocities, the mean velocity variance was increasing during the matter domination epoch as structures grew. However it turns over near $z = -0.1$ and the spatially-average relative speed begins slow. In this model, the mean velocity variance is very near its maximum today. This is understood by the fact that we are currently in the transition epoch from matter domination to dark energy domination. As dark energy becomes the dominant energy density in the universe, matter structures stop growing and are pulled apart from each other, decreasing the net phase space. In the range of $-1 \leq z \lesssim 1$, the result is described quite well by the function

$$\left\langle \sigma_u^2 \right\rangle(z) \approx A(1+z)\exp\left\{-[B(1+z)]^{1+B}\right\} \tag{2.164}$$

where $A = 2.97 \times 10^{-9}$ and $B = 0.8$ are constants. The relative error of the fit is shown in the inset of the figure.

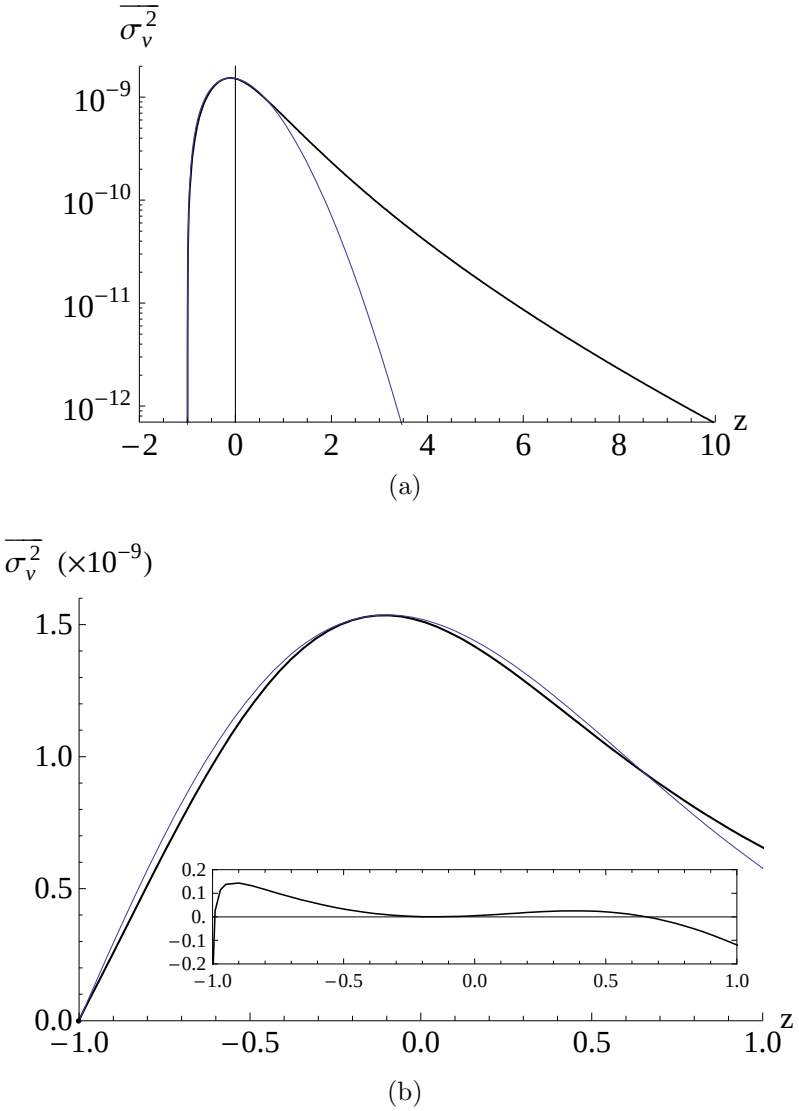


Figure 3: Spatially averaged one-point velocity variance, $\langle \sigma_u^2 \rangle(z)$. It is calculated from the spherical halo model for parameters described in the text. In (a) is a log plot, and (b) shows a linear plot. The thin, blue fitting curve, given by Eqn. (2.164), agrees well for $-1 \leq z \lesssim 1$, to within 15% except for very near $z = -1$. The relative error of the fit is shown in the inset.

# 3 CONTRIBUTIONS OF PARTICLE PHYSICS TO EXTRAGALACTIC DARK MATTER ANNIHILATION*

## 3.1 Particle Properties Important for Annihilation Signals

The signals of cosmic dark matter annihilation depend on the nature of the dark matter particle, and details of its self-interaction. These properties are specified by the particle physics model. Given the particle Lagrangian, the particle properties important to indirect detection can be determined. For simplicity, it is assumed that the dark matter is composed of a single species of particle. Generalizing the calculations in this dissertation to models where the dark matter is made up of more than one kind of particle is straight forward to do.

The quantities that contribute to the observable annihilation radiation are:

- the dark matter annihilation cross section $\sigma(v)$, expressed here as a function of the relative velocity $v$ of the annihilating dark matter particles,
- the spectrum $\frac{\mathrm{d}N_\gamma}{\mathrm{d}E_\gamma}(E_\gamma, v)$ of produced gamma-rays of energy $E_\gamma$, per annihilation at relative velocity $v$, and
- the dark matter particle mass $m_{\mathrm{DM}}$.

It is often more convenient to consider the velocity dependence of the quantities $\sigma v$ and $\mathrm{d}N_\gamma/\mathrm{d}E_\gamma$ in terms of $v^2$. Hence, frequently they will appear in this dissertation written as $[\sigma v](v^2)$ and $\frac{\mathrm{d}N_\gamma}{\mathrm{d}E_\gamma}(E_\gamma, v^2)$.

---

*Parts of this section are reprinted with permission from "*Effects of Velocity-Dependent Dark Matter Annihilation on the Energy Spectrum of the Extragalactic Gamma-ray Background*" by S. Campbell, B. Dutta, and E. Komatsu, Phys. Rev. D **82**, 095007 (2010), Copyright 2010 by The American Physical Society, and "*Effects of P-wave Annihilation on the Angular Power Spectrum of Extragalactic Gamma-rays from Dark Matter Annihilation*" by S. Campbell and B. Dutta, Phys. Rev. D **84**, 075004 (2011), Copyright 2011 by The American Physical Society.

Let $i = 1, 2, \ldots, N$ enumerate the different channels of annihilation in the theory. Each annihilation channel has its own velocity-weighted cross section $[\sigma v]_i(v^2)$, and produces gamma-rays with average spectrum per annihilation of $\frac{\mathrm{d}N_{\gamma,i}}{\mathrm{d}E_\gamma}(E_\gamma, v^2)$.

To understand the significance of these particle quantities, consider a volume (infinitesimal $\mathrm{d}V$) of dark matter particles at some position $\mathbf{r}$ with number density $n(\mathbf{r})$ and velocity distribution $f_{\mathbf{u}}(\mathbf{u}|\mathbf{r})$ such that $\int \mathrm{d}^3\mathbf{u}' f_{\mathbf{u}}(\mathbf{u}') = 1$ and the mean particle velocity is $\overline{\mathbf{u}} = \int \mathrm{d}^3\mathbf{u}'\mathbf{u}' f_{\mathbf{u}}(\mathbf{u}')$. From $f_{\mathbf{u}}$, the distribution of square relative velocities $v^2$ is

$$f_{v^2}(v^2) = \int \mathrm{d}^3\mathbf{u}_1 \mathrm{d}^3\mathbf{u}_2 f_{\mathbf{u}}(\mathbf{u}_1) f_{\mathbf{u}}(\mathbf{u}_2) \delta(v^2 - |\mathbf{u}_1 - \mathbf{u_2}|^2).$$

The total annihilation cross section $\sigma(v) = \sum_{i=1}^{N} \sigma_i(v)$ determines the rate at which annihilations occur in this volume $\mathrm{d}V$ of dark matter. Recall that the cross section of annihilation $\sigma(v)$ is defined as the rate $\Gamma_p$ of annihilations per target particle, divided by the incident flux $nv$ on the target (for an incident particle with relative speed $v$ with the target). By averaging over all particles incident on the target, the mean annihilation rate per target at position $\mathbf{r}$ is

$$\overline{\Gamma}_p(\mathbf{r}) = n(\mathbf{r})\overline{\sigma v}(\mathbf{r}), \tag{3.1}$$

where the mean velocity-weighted cross section is

$$\overline{\sigma v}(\mathbf{r}) = \int \mathrm{d}v^2 f_{v^2}(v^2|\mathbf{r})[\sigma v](v^2). \tag{3.2}$$

The annihilation rate per unit volume at the given position is

$$\frac{\mathrm{d}\Gamma}{\mathrm{d}V}(\mathbf{r}) = \frac{1}{2} n(\mathbf{r})\overline{\Gamma}_p(\mathbf{r}) = \frac{1}{2} n^2(\mathbf{r})\overline{\sigma v}(\mathbf{r}), \tag{3.3}$$

where the factor of $1/2$ occurs because each particle is being considered as both an incident and a target particle, thus double-counting each possible interaction between pairs of particles.

The annihilation spectrum is required to determine the power emissivity $\frac{\mathrm{d}P_\gamma}{\mathrm{d}V\mathrm{d}E_\gamma}$ of annihilation-produced gamma-rays: that is, the amount of energy emitted, due to produced gamma-rays with energy between $E_\gamma$ and $E_\gamma + \mathrm{d}E_\gamma$, per unit time, per unit volume $\mathrm{d}V$, per unit energy range $\mathrm{d}E_\gamma$. In particular, what is needed is the quantity

$$[\sigma v](v^2)\frac{\mathrm{d}N_\gamma}{\mathrm{d}E_\gamma}(E_\gamma, v^2) = \sum_i [\sigma v]_i(v^2)\frac{\mathrm{d}N_{\gamma,i}}{\mathrm{d}E_\gamma}(E_\gamma, v^2) \tag{3.4}$$

$$= [\sigma v](v^2)\sum_i B_i(v^2)\frac{\mathrm{d}N_{\gamma,i}}{\mathrm{d}E_\gamma}(E_\gamma, v^2), \tag{3.5}$$

where the channel branching fractions $B_i = \sigma_i/\sigma$ satisfy $\sum B_i = 1$.

The rate of energy of these emitted gamma-rays, per target particle, per gamma-ray energy range $\mathrm{d}E_\gamma$, for incident particles of square relative velocity $v^2$, is

$$\frac{\mathrm{d}P_{\gamma,p}}{\mathrm{d}E_\gamma}(E_\gamma, v^2) = \Gamma_p(v^2)E_\gamma\frac{\mathrm{d}N_\gamma}{\mathrm{d}E_\gamma}(E_\gamma, v^2) = nE_\gamma[\sigma v](v^2)\frac{\mathrm{d}N_\gamma}{\mathrm{d}E_\gamma}(E_\gamma, v^2).$$

Averaging this quantity over the incident particles in the volume gives

$$\overline{\frac{\mathrm{d}P_{\gamma,p}}{\mathrm{d}E_\gamma}}(E_\gamma, \mathbf{r}) = n(\mathbf{r})E_\gamma\overline{\frac{\mathrm{d}N_\gamma}{\mathrm{d}E_\gamma}\sigma v}(E_\gamma, \mathbf{r}).$$

The power emissivity at position $\mathbf{r}$ is thus

$$\frac{\mathrm{d}P_\gamma}{\mathrm{d}V\mathrm{d}E_\gamma}(E_\gamma, \mathbf{r}) = \frac{1}{2}n(\mathbf{r})\overline{\frac{\mathrm{d}P_{\gamma,p}}{\mathrm{d}E_\gamma}}(E_\gamma, \mathbf{r}) = \frac{1}{2}E_\gamma n^2(\mathbf{r})\overline{\frac{\mathrm{d}N_\gamma}{\mathrm{d}E_\gamma}\sigma v}(E_\gamma, \mathbf{r}). \tag{3.6}$$

For initial considerations, the work in this dissertation will assume that the particle models being considered each have a dark matter annihilation spectrum $\mathrm{d}N_\gamma/\mathrm{d}E_\gamma$ that depends negligibly on the relative velocity of the annihilating particles, over the relevant energy range of annihilations occurring in the cosmos. This is a good approximation if all of the relevant branching fractions, and each channel's gamma-ray-spectrum-per-annihilation, do not change with the energy of annihilation. The annihilation spectrum also will not change significantly if the

annihilation spectra of channels with changing branching fractions are indistinguishable. For these types of theories, the power emissivity can be written

$$\frac{\mathrm{d}P_\gamma}{\mathrm{d}V\mathrm{d}E_\gamma}(E_\gamma,\mathbf{r}) = \frac{\mathrm{d}\Gamma}{\mathrm{d}V}E_\gamma\frac{\mathrm{d}N_\gamma}{\mathrm{d}E_\gamma}(E_\gamma) = \frac{1}{2}E_\gamma\frac{\mathrm{d}N_\gamma}{\mathrm{d}E_\gamma}(E_\gamma)n^2(\mathbf{r})\overline{\sigma v}(\mathbf{r}). \tag{3.7}$$

The dark matter particle mass $m_{\mathrm{DM}}$ appears explicitly in the number density, to convert it to the mass density $\rho$. Implicitly, the cross section and annihilation spectrum also depend on the particle mass. The energy of the produced gamma-rays scales with $m_{\mathrm{DM}}$, the spectrum has an upper kinematical cutoff near $m_{\mathrm{DM}}$, and the normalization of the spectrum typically scales like $m_{\mathrm{DM}}^{-1}$. Between this and the dependence of $n$, the power emissivity scales roughly like $m_{\mathrm{DM}}^{-3}$.

$$\frac{\mathrm{d}P_\gamma}{\mathrm{d}V\mathrm{d}E_\gamma}(E_\gamma,\mathbf{r}) = \frac{E_\gamma}{2m_{\mathrm{DM}}^3}\frac{\mathrm{d}N_\gamma}{\mathrm{d}(\frac{E_\gamma}{m_{\mathrm{DM}}})}\left(\frac{E_\gamma}{m_{\mathrm{DM}}}\middle|\, m_{\mathrm{DM}}\right)[\rho^2\overline{\sigma v}](\mathbf{r}|m_{\mathrm{DM}}) \tag{3.8}$$

## 3.2 Non-relativistic Velocity-Dependence of Annihilation Cross Sections

### 3.2.1 S-wave and P-wave Annihilations

If the particle annihilation is not through a resonance, partial wave analysis can decompose the cross section into its constituent multipole contributions.

$$[\sigma v](v^2) = \sum_{\ell=0}^{\infty}[\sigma v]_\ell(v^2)$$

Each component takes the form

$$[\sigma v]_\ell(v^2) = \sum_{n=\ell}^{\infty} C_{\ell,n}v^{2n}$$

for constant coefficients $C_{\ell,n}$. The first multipole is the s-wave component

$$[\sigma v]_0(v^2) = \sum_{n=0}^{\infty} s_n v^{2n}$$

for constant coefficients $s_n \equiv C_{0,n}$, and the p-wave is the second multipole

$$[\sigma v]_1(v^2) = \sum_{n=1}^{\infty} p_n v^{2n}$$

for constant coefficients $p_n \equiv C_{1,n}$. That is,

$$[\sigma v](v^2) = s_0 + (s_1 + p_1)v^2 + \mathcal{O}(v^4).$$

Because cosmic dark matter is non-relativistic, then $v \ll 1$ in light-speed units, and $\sigma v$ is constant to high precision for all cosmic particle relative velocities. However, it sometimes occurs that the s-wave is suppressed, due to a symmetry. If sufficiently small, so that $s_0 \ll p_1$ and $s_1 \ll p_1$, then p-wave annihilation is important. In this case, it is typical in the literature for the cross section to be written as

$$[\sigma v](v^2) = a + bv^2, \tag{3.9}$$

where $a$ and $b$ are constants. If the s-wave is suppressed, then $b$ is dominated by the p-wave, and it is often referred to as the p-wave contribution, even though the s-wave also contributes to it. An example of an annihilation cross section with a strong p-wave is shown in the figure on page 104, found in Section 5.2, where calculations with realistic particle physics models are shown.

Annihilation with p-wave is an example where the cross section increases with interaction energy. However, there exist possible resonance effects that could be responsible for an increase of the cross section at lower interaction energies. These may include Sommerfeld enhancements, and Breit-Wigner resonances.

### 3.2.2 Sommerfeld-Enhanced Annihilation

The Sommerfeld enhancement [105–107] of dark matter annihilation occurs in cases where the annihilation is mediated by an attractive Yukawa force through a scalar or vector boson. Non-perturbative resonant boson exchange between annihilating particles is demonstrated to result in a significant enhancement of the cross-section that grows as relative particle motion decreases.

Although this enhancement occurs for any partial wave [107], I will (for simplicity) present intensity spectra for s-wave Sommerfeld enhancement. It is expressed in the form

$$[\sigma v](v) = S\left(\frac{v}{\alpha}\middle|\epsilon_\phi\right)[\sigma v]_0, \tag{3.10}$$

where $[\sigma v]_0$ is the relative-velocity-weighted annihilation cross section at tree level, assumed constant at all relevant energies for this model, and set for the calculations to $[\sigma v]_f = 3 \times 10^{-26}$ cm$^3$/s to satisfy the relic density (although, in careful calculations, the enhancement can have significant effects on the relic density calculation [108]). Here, $\alpha$ is the Yukawa coupling between the dark matter and mediator, and

$$\epsilon_\phi \equiv \frac{m_\phi}{m_{\mathrm{DM}}\alpha}$$

with $m_\phi$ the mediator mass. For convenience, $\epsilon_v \equiv \frac{v}{\alpha}$ is also defined.

Following the derivation by [106], $S$ is extracted from the solution $\Phi(x)$ of the Schrödinger equation

$$\Phi'' + \frac{2}{x}\Phi' + (1 - \tilde{U})\Phi = 0$$

with boundary conditions $\Phi(0) = 1$ and $\Phi'(0) = -1/\epsilon_v$, and where

$$\tilde{U}(x) \equiv -\frac{2}{\epsilon_v x}e^{-2\frac{\epsilon_\phi}{\epsilon_v}x}$$

is the normalized potential. This is more illuminating with $\psi(x) \equiv x\Phi(x)$, in which case the Schrödinger equation becomes

$$\psi'' + (1 - \tilde{U})\psi = 0 \tag{3.11}$$

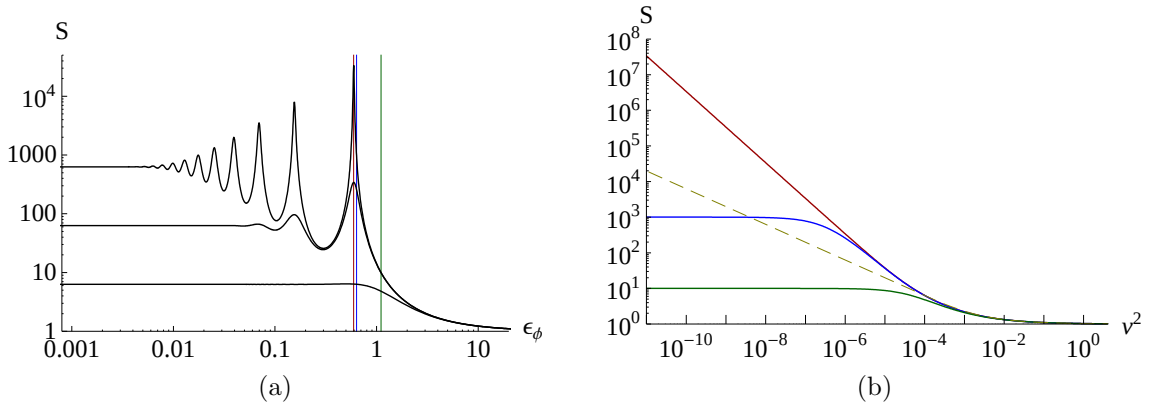


Figure 4: The s-wave Sommerfeld enhancement. (a) $S(\epsilon_v|\epsilon_\phi)$ vs. $\epsilon_\phi$ for $\epsilon_v = 1$, 0.1, and 0.01 from bottom to top, respectively. The vertical lines correspond, from right to left, to $\epsilon_\phi = 1.107$, 0.635, and the first Sommerfeld resonance $\epsilon_\phi^{(1)}$ described in the text. (b) $S(\frac{v}{\alpha}|\epsilon_\phi)$ vs. $v^2$ for $\alpha = 0.01$. The solid curves show the enhancement for the same three values of $\epsilon_\phi$ specified earlier from bottom to top, and the dashed curve shows the Coulomb case where $\epsilon_\phi = 0$.

with the necessary solution near the boundary of $\lim_{x\to 0}\psi = x - x^2/\epsilon_v$ and $\lim_{x\to 0}\psi' = 1 - 2x/\epsilon_v$.

Written in this form, it is now easy to see that $\psi$ converges very quickly to a sinusoid as $x$ increases. $S$ is simply the inverse square of the amplitude of $\psi$ far from the origin. One could integrate Eq. (3.11) to $x = x_M$ large enough that $\tilde{U}(x_M)$ is sufficiently negligible, and simply evaluate

$$S = \frac{1}{\psi^2(x_M) + \psi'^2(x_M)}. \tag{3.12}$$

Figure 4a shows the enhancement for $\epsilon_v = 1$, 0.1, and 0.01. As relative velocity decreases, a series of Sommerfeld resonances reveals itself.

Define the locations of the resonances to be at $\epsilon_\phi = \epsilon_\phi^{(n)}$ for $n = 1, 2, \ldots$. Analytic approximations show the first few s-wave resonances to be near $\epsilon_\phi^{(n)} \approx 6/(n\pi)^2$.

Also,

$$\lim_{\epsilon_v \to 0} S(\epsilon_v | \epsilon_\phi^{(n)}) = \frac{A^{(n)}}{\epsilon_v^2},$$

where $A^{(n)}$ are constants. The first resonance, found at $\epsilon_\phi^{(1)} = 0.595\,306\,210\,530\,309$, has $A^{(1)} = 3.37286$, up to the given precisions. Away from the resonances, the enhancement saturates to a constant value as $v$ diminishes. Until the resonances arise at low $\epsilon_\phi$, $S$ follows the Coulomb-Sommerfeld enhancement in the center-of-momentum frame

$$S(\epsilon_v | 0) = \frac{2\pi/\epsilon_v}{1 - e^{-2\pi/\epsilon_v}},$$

which scales like $\epsilon_v^{-1}$ at low $v$. Examples of the relative velocity dependence of each of these cases are shown in Figure 4b for $\alpha = 0.01$.

In principle, the resonance cross-sections can break unitarity bounds for s-wave annihilation [109]. If the scattering operator conserves angular momentum and is unitary, then the weighted s-wave annihilation cross section must satisfy [110]

$$\sigma v \leq \frac{4\pi}{m_{\rm DM}^2 v}. \tag{3.13}$$

In the low-$v$ limit $v \ll \alpha$ for the Coulomb case, this provides an upper bound on the mass for a given coupling:

$$\alpha m_{\rm DM}^2 \lesssim \frac{2}{[\sigma v]_f} \sim (30\ {\rm TeV})^2, \quad \text{for } \epsilon_\phi = 0 \tag{3.14}$$

for the value of $[\sigma v]_f$ in our model. For the first Sommerfeld resonance, we require

$$v \gtrsim v_{\rm min} \equiv \frac{A^{(1)} m_{\rm DM}^2 \alpha^2}{4\pi} [\sigma v]_f \sim \left(\frac{m_{\rm DM}\alpha}{40\ {\rm TeV}}\right)^2, \quad \text{for } \epsilon_\phi = \epsilon_\phi^{(1)}. \tag{3.15}$$

As long as the enhancement saturates before getting to relative velocities below $v_{\rm min}$, the theory is consistent. Otherwise, some neglected model-dependent effects (such as finite widths or non-perturbative dynamics) become important and must be taken into account. A model near resonance which saturates below scales that contribute to the intensity would be indistinguishable from the resonance intensity,

but would still satisfy unitarity constraints.

### 3.2.3 Annihilation Through Breit-Wigner Resonance

The final common example of effect in annihilation cross sections to be mentioned in this section is the Breit-Wigner resonance, due (for example) to the mass of the annihilation mediator's being at the energy of the annihilating particles. If the dark matter annihilates via an unstable particle of mass $M$ and decay rate $\Gamma \ll M$, and the center-of-momentum energy $E$ of the annihilation is near $M$, then the annihilation cross section is of the form [111]

$$\sigma_{\text{BW}}(E) \propto \frac{1}{E\sqrt{E^2 - 4m_{\text{DM}}^2}} \frac{M^2\Gamma^2}{(E^2 - M^2)^2 + M^2\Gamma^2}. \tag{3.16}$$

If we define

$$\begin{aligned} \tilde{\Gamma} &\equiv \frac{\Gamma}{M}, \\ \Delta m &\equiv \frac{M}{2} - m_{\text{DM}}, \text{ and} \\ \overline{\Delta m} &\equiv \frac{\Delta m}{M}\left(1 - \frac{\Delta m}{M}\right), \end{aligned}$$

then, for any relative velocity $v$ of the annihilating particles and spectral separation $\Delta m$, the velocity dependence of the cross section near the resonance is

$$[\sigma v]_{\text{BW}}(v) \propto \frac{\sqrt{1 - \left(\frac{v}{2}\right)^2}}{1 + \left[\frac{\left(\frac{v}{2}\right)^2 - 4\overline{\Delta m}}{\tilde{\Gamma}\left[1 - \left(\frac{v}{2}\right)^2\right]}\right]^2}. \tag{3.17}$$

For a non-relativistic resonance, we have $v \ll 1$ and $|\Delta m| \ll M$, and the cross section is

$$[\sigma v]_{\text{BW}}(v) = \frac{[\sigma v]_r}{1 + \frac{1}{\tilde{\Gamma}^2}\left[\left(\frac{v}{2}\right)^2 - 4\overline{\Delta m}\right]^2}, \tag{3.18}$$

where, in this context, $\overline{\Delta m} = \Delta m/M$ and $[\sigma v]_r$ is the velocity-weighted cross section at the resonance energy where $v = v_r \equiv 4\sqrt{\overline{\Delta m}}$ (which is unattainable by the interaction in the case that $M < 2m_{\rm DM}$).

If there are no other significant additional features in the cross section from the resonance scale $v_r$ to the freezeout scale $v_f = 6T_f/m_{\rm DM} \sim 1/2$ for freezeout temperature $T_f$, then $[\sigma v]_r$ can be correlated to the mean cross section at freezeout $[\sigma v]_f \sim 3 \times 10^{-26}$ cm$^3$/s:

$$[\sigma v]_r \sim \frac{[\sigma v]_f}{(16\tilde{\Gamma})^2}$$

for theories where one may assume $v_f \sim 1/2$, $|\overline{\Delta m}| \ll 1/64$, and $\tilde{\Gamma} \ll 1/16$. Also note that some $\mathcal{O}(1)$ constants are being neglected, owing to $v_f$ being near 1. In this kind of theory,

$$[\sigma v]_{\rm BW}(v) = \frac{\eta[\sigma v]_f}{(16)^2} \frac{\left[1 - \left(\frac{v}{2}\right)^2\right]^{5/2}}{\left[\left(\frac{v}{2}\right)^2 - 4\overline{\Delta m}\right]^2 + \tilde{\Gamma}^2\left[1 - \left(\frac{v}{2}\right)^2\right]^2} \tag{3.19}$$

up to the freezeout scale where $\eta$ is an $\mathcal{O}(1)$ constant that takes into account the approximations of the relic density calculation and relativistic freezeout velocities.

The velocity dependence for s-wave annihilation via a non-relativistic ($v_r \ll 1$ and $|\Delta m| \ll M/64$) Breit-Wigner resonance of small width ($\Gamma \ll M/16$) is therefore found to have the broad behavior of

$$[\sigma v]_{\rm BW}(v) \approx \begin{cases} \dfrac{\eta[\sigma v]_f}{(16v_s)^2}, & \text{for } \dfrac{v}{2} \ll v_s, \\ \dfrac{\eta[\sigma v]_f}{16v^4}, & \text{for } v_s \ll \dfrac{v}{2} \ll 1, \end{cases} \tag{3.20}$$

where the cross section saturates at

$$\frac{v}{2} \sim v_s \equiv \sqrt[4]{\tilde{\Gamma}^2 + (4\overline{\Delta m})^2}. \tag{3.21}$$

Accordingly, when the energy scale of the dark matter is above the saturation threshold, $[\sigma v]_{\rm BW}(v) \propto v^{-4}$, and when the cross section is saturated, it is modified

by a factor of $\sim (16 v_s)^{-2}$ from the freezeout cross section. Behaviors for other cases of Breit-Wigner resonance could be similarly derived starting from Eq. (3.17), and their features in the extragalactic gamma-ray spectrum due to dark matter annihilation could then be studied using the methods described in the rest of Section 4.

A summary of the simple functional forms of $[\sigma v](v^2)$ for non-relativistic velocities that were encountered in this section is given in Table 1. In this dissertation, sample calculations are given of the mean intensity and angular power spectrum of extragalactic gamma-rays from annihilation with strong p-wave, and the mean intensity for annihilation with various Sommerfeld enhancements and resonances. These results are presented in Section 5.

Table 1: Possible non-relativistic scalings of $[\sigma v](v)$.

| | |
|---|---|
| $v^{-4}$ | non-relativistic Breit-Wigner resonance |
| $v^{-2}$ | Yukawa-Sommerfeld resonance |
| $v^{-1}$ | Coulomb-Sommerfeld resonance |
| $v^{0}$ | s-wave, saturated resonance |
| $v^{2}$ | p-wave |

## 3.3 Universal Halo Cross-section Profiles

Given the dark matter annihilation cross section $[\sigma v](v^2)$, such as one of the examples in Section 3.2, the next step is to apply Equation (3.2) to determine $\overline{\sigma v}(\mathbf{r})$ at each position. When the distribution of particle velocities in a dark matter halo follows a universal profile, then the mean velocity-weighted cross section halo profile $[\overline{\sigma v}]_h(r)$ is also universal. This observation is what couples the particle annihilation physics to the halo statistics of large scale structure.

For the case of p-wave annihilation, the full velocity distribution is not required. We only need the mean-square-relative-velocity profile, as in Equation (2.131).

$$[\overline{\sigma v}]_h(r) = a + b v_h^2(r) = a + \lambda b \sigma_{uh}^2(r) \tag{3.22}$$

In this way, whenever $\sigma v$ is a polynomial in $v^2$, one only requires the mean of whole powers of $v^2$ at each position of the halo, rather than the complete relative velocity distribution function at each position.

For more complicated functional forms of $\sigma v$, the halo profile, calculated from (3.2), in principle requires knowledge of the particle velocity distribution at each position in the halo. For a simple "zeroth order" estimation, one might approximate

$$[\overline{\sigma v}]_h(r) \approx [\sigma v](v_h^2(r)). \tag{3.23}$$

This approximates $f_{v^2}(v^2|r) \approx \delta(v^2 - \lambda\sigma_{uh}^2(r))$, which happens to be exact for p-wave annihilation. The next order of approximation that is often used is to assume an isotropic Maxwell-Boltzmann distribution at each position with velocity variance $\sigma_{uh}^2(r)$. The velocity distributions observed in simulated dark matter halos are better described by Tsallis distributions [112], but the profile of the Tsallis distribution parameters in halos remains to be determined from the simulations.

# 4 DARK MATTER ANNIHILATION PRODUCTS FROM EXTRAGALACTIC UNIVERSAL HALOS: FORMALISM*

## 4.1 Intensity of Massless Annihilation Products from Extragalactic Dark Matter Annihilation

In this section, a formula is derived to determine the intensity $I_\gamma$ of gamma-rays of energy $E_\gamma$ from the annihilation of dark matter along a line of sight in the direction $\hat{\mathbf{n}}$. The argument is a generalization of the discussion found in [113]. It is applicable to any specified phase space distribution of the dark matter particles, and any theory of dark matter particle annihilation.

To begin, consider a volume $\mathrm{d}V$ of dark matter particles with number density $n$ that may annihilate one another, as in Section 3.1. The rate of particle annihilations per unit volume is given by Equation (3.3); Equation (3.6) expresses the power emissivity of the annihilations.

In a flat FLRW cosmology, using the physical coordinates in the cosmological rest frame described in Section 2.1, the proper volume of space with solid angle $\mathrm{d}\Omega$ and thickness $\mathrm{d}z$ at redshift $z$ is

$$\mathrm{d}V = [a(z)\mathrm{d}r][a^2(z)r^2\mathrm{d}\Omega] = \frac{1}{(1+z)^3}r^2\mathrm{d}r\mathrm{d}\Omega$$

where $a$ is the cosmological scale factor. Consider each position $\mathbf{r}$ to be specified as being in a particular direction $\hat{\mathbf{n}}$ with distance specified by redshift $z$, as in Equation (2.9). The discussion will treat $z$ as a time coordinate given by (2.15).

*Parts of this section are reprinted with permission from "*Effects of Velocity-Dependent Dark Matter Annihilation on the Energy Spectrum of the Extragalactic Gamma-ray Background*" by S. Campbell, B. Dutta, and E. Komatsu, Phys. Rev. D **82**, 095007 (2010), Copyright 2010 by The American Physical Society, and "*Effects of P-wave Annihilation on the Angular Power Spectrum of Extragalactic Gamma-rays from Dark Matter Annihilation*" by S. Campbell and B. Dutta, Phys. Rev. D **84**, 075004 (2011), Copyright 2011 by The American Physical Society.

The luminosity $\mathrm{d}L_\gamma(E_\gamma, \mathbf{r})$ of photons of energy $E_\gamma$ emitted from the region of space at position $\mathbf{r}$ because of annihilations is

$$\mathrm{d}L_\gamma(E_\gamma, \mathbf{r}, z) = \frac{\mathrm{d}P_\gamma}{\mathrm{d}V\mathrm{d}E_\gamma}(E_\gamma, \mathbf{r}, z)\mathrm{d}V = \frac{1}{2}E_\gamma n^2(\mathbf{r})\overline{\frac{\mathrm{d}N_\gamma}{\mathrm{d}E_\gamma}\sigma v}(E_\gamma, \mathbf{r})\frac{1}{(1+z)^3}r^2\mathrm{d}r\mathrm{d}\Omega.$$

Assuming isotropic emission, the photons emitted by this volume pass with uniform flux density through any sphere centered on the source. The sphere on which we sit, centered on the source, has proper surface area

$$A = 4\pi r^2 a^2(0) = 4\pi r^2.$$

The total luminosity on this shell (energy of photons emitted from the source with energies between $E_\gamma$ and $E_\gamma + \mathrm{d}E_\gamma$, per $\mathrm{d}E_\gamma$, per unit time of emission) is redshifted: the cosmological redshift of photon energy due to the expansion of the universe is cancelled by the redshift of the energy bin $\mathrm{d}E_\gamma$; the arrival rate of photons is redshifted giving one factor of $(1+z)^{-1}$. Observation of photons of energy $E_\gamma$ means photons of energy $(1+z)E_\gamma$ were emitted. Hence, the luminosity of photons on the observer's spherical shell with energy $E_\gamma$ from the source at redshift $z$ is

$$\mathrm{d}L'_\gamma(E_\gamma, \mathbf{r}, z) = \frac{\mathrm{d}L_\gamma((1+z)E_\gamma, \mathbf{r}, z)}{1+z}e^{-\tau((1+z)E_\gamma, z)}$$

where $\tau(E_\gamma, z)$ is the optical depth of the universe to gamma rays [104]. The photon flux on the sphere, or surface brightness, due to a source at position $\mathbf{r}$ and redshift $z$ is

$$\begin{aligned}\mathrm{d}S_\gamma(E_\gamma,&\mathbf{r}, z) = \frac{\mathrm{d}L'_\gamma(E_\gamma, \mathbf{r}, z)}{A(z)} \\ &= \frac{1}{8\pi}(1+z)E_\gamma n^2(\mathbf{r})\overline{\frac{\mathrm{d}N_\gamma}{\mathrm{d}E_\gamma}\sigma v}((1+z)E_\gamma, \mathbf{r})e^{-\tau((1+z)E_\gamma, z)}\frac{1}{(1+z)^4}\mathrm{d}r\mathrm{d}\Omega,\end{aligned}$$

where (2.9) is used to express the line-of-sight integration in terms of redshift with the Hubble function $H(z)$ expressed by (2.14). The net specific intensity (number of photons of energy $E_\gamma$ observed per bin $\mathrm{d}E_\gamma$, per unit time, per source solid angle, per normal photon collecting area) is found from a line-of-sight integration in

direction $\hat{\mathbf{n}}$:

$$I_\gamma(E_\gamma, \hat{\mathbf{n}}) = \int \frac{\mathrm{d}S_\gamma(E_\gamma, z)}{E_\gamma \mathrm{d}\Omega} = \frac{1}{8\pi m_{\mathrm{DM}}} \int \frac{\mathrm{d}z}{H(z)} \frac{1}{(1+z)^3} e^{-\tau((1+z)E_\gamma, z)} \left[\rho^2 \overline{\frac{\mathrm{d}N_\gamma}{\mathrm{d}E_\gamma} \sigma v}\right] ((1+z)E_\gamma, \hat{\mathbf{n}}, z). \tag{4.1}$$

Considering models where the annihilation spectrum is negligibly dependent on the relative velocity, the gamma-ray intensity from annihilations is

$$I_\gamma(E_\gamma, \hat{\mathbf{n}}) = \int \frac{\mathrm{d}z}{H(z)} W((1+z)E_\gamma, z)[\rho^2 \overline{\sigma v}](\hat{\mathbf{n}}, z), \tag{4.2}$$

where the important spatially dependent field $\rho^2 \overline{\sigma v}$ is weighted by the intensity window function

$$W(E_\gamma, z) = \frac{1}{8\pi m_{\mathrm{DM}}^2} \frac{1}{(1+z)^3} \frac{\mathrm{d}N_\gamma}{\mathrm{d}E_\gamma}(E_\gamma) e^{-\tau(E_\gamma, z)}. \tag{4.3}$$

## 4.2 The Mean Extragalactic Annihilation Intensity in the Spherical Halo Model

From (4.2), the mean intensity of annihilation gamma-rays is found from averaging over ensembles of dark matter halos

$$\langle I_\gamma \rangle (E_\gamma) = \int \frac{\mathrm{d}z}{H(z)} W((1+z)E_\gamma, z) \left\langle \rho^2 \overline{\sigma v} \right\rangle (z). \tag{4.4}$$

In the disjoint halo model, an ensemble of halos at redshift $z$ has

$$[\rho^2 \overline{\sigma v}](\mathbf{r}, z) = \sum_{i=1}^{N_h(z)} \rho_h^2(\mathbf{r} - \mathbf{R}_i(z) \,|\, M_i(z), z)\ [\overline{\sigma v}]_h(\mathbf{r} - \mathbf{R}_i(z) \,|\, M_i(z), z)$$

where $\mathbf{r}$ are a global set of coordinates at the time associated with redshift $z$. For disjoint ensembles, at most one term contributes to the sum at any given position $\mathbf{r}$. This expression allows the formulation of the ensemble average in terms of the

halo mass function, using (2.132) and (2.133).

$$\begin{aligned}\left\langle \rho^2 \overline{\sigma v} \right\rangle(z) &= \int \mathrm{d}^3\mathbf{R}\,\mathrm{d}M \left\langle \sum_{i=1}^{N_h(z)} \delta^{(3)}(\mathbf{R}-\mathbf{R}_i(z))\,\delta(M-M_i(z)) \right\rangle \\ &\quad \times \rho_h^2(\mathbf{r}-\mathbf{R}\,|\,M,z)\;[\overline{\sigma v}]_h(\mathbf{r}-\mathbf{R}\,|\,M,z) \\ &= \int \mathrm{d}^3\mathbf{R}\,\mathrm{d}M \frac{\mathrm{d}n}{\mathrm{d}M}(M,z)\;\rho_h^2(R|M,z)\;[\overline{\sigma v}]_h(R|M,z) \end{aligned} \tag{4.5}$$

For s-wave annihilation, $\sigma v = [\sigma v]_0$, a constant. Then the intensity spectrum is

$$\langle I_\gamma \rangle_0(E_\gamma) = [\sigma v]_0 \int \frac{\mathrm{d}z}{H(z)}\, W((1+z)E_\gamma, z)\;\left\langle \rho^2 \right\rangle(z) \tag{4.6}$$

where

$$\left\langle \rho^2 \right\rangle(z) = \int \mathrm{d}^3\mathbf{r}\mathrm{d}M \frac{\mathrm{d}n}{\mathrm{d}M}(M,z)\rho_h^2(r|M,z). \tag{4.7}$$

For annihilation with p-wave, the velocity-weighted annihilation cross section is

$$\sigma v = a + bv^2 = [\sigma v]_0 \left(1 + \frac{b}{a}v^2\right)$$

where $[\sigma v]_0 = a$ and $b$ are constants, and the cross section halo profile is given by (3.22). In this case, if there is significant dark matter annihilation with square relative velocities $\gtrsim a/b$, then the distribution of produced gamma-rays is coupled to the cosmic dark matter velocity distribution. The intensity spectrum with p-wave annihilation is

$$\langle I_\gamma \rangle\,(E_\gamma) = [\sigma v]_0 \int \frac{\mathrm{d}z}{H(z)} W((1+z)E_\gamma, z) \left\langle \rho^2 \left(1 + \frac{\lambda b}{a}\sigma_u^2\right) \right\rangle(z) \tag{4.8}$$

where

$$\begin{aligned}\left\langle \rho^2 \left(1 + \frac{\lambda b}{a}\sigma_u^2\right) \right\rangle(z) &= \int \mathrm{d}^3\mathbf{r}\mathrm{d}M \frac{\mathrm{d}n}{\mathrm{d}M}(M,z)\rho_h^2(r|M,z) \left[1 + \frac{\lambda b}{a}\sigma_{uh}^2(r|M,z)\right] \\ &= \left\langle \rho^2 \right\rangle(z) + \frac{\lambda b}{a}\left\langle \rho^2 \sigma_u^2 \right\rangle(z). \end{aligned} \tag{4.9}$$

The effects of the p-wave on the shape of the annihilation spectrum are encoded in the relative contribution of the new second term, due to the p-wave, given by

$$\frac{\langle I_\gamma\rangle(E_\gamma|\sigma v = a + bv^2)}{\langle I_\gamma\rangle_0(E_\gamma|\sigma v = a)} - 1 = \frac{\lambda b}{a}\Delta_I(E_\gamma) \tag{4.10}$$

with

$$\Delta_I(E_\gamma) \equiv \frac{\int \frac{\mathrm{d}z}{H(z)} W((1+z)E_\gamma, z)\,\langle\rho^2\sigma_u^2\rangle(z)}{\int \frac{\mathrm{d}z}{H(z)} W((1+z)E_\gamma, z)\,\langle\rho^2\rangle(z)}. \tag{4.11}$$

Other than the dependence on large scale structure in the ensemble averages, $\Delta_I$ depends only on the details of the annihilation spectrum and opacity effects. Note the relative change in intensity diverges for vanishing $[\sigma v]_0$ since the s-wave intensity is zero in this limit.

## 4.3 The Angular Power Spectrum of the Intensity

The formulation of the angular power spectrum in this section is a generalization of the derivation in [51]. The angular anisotropies in the intensity signal are explored by determining its angular power spectrum, defined as

$$C_\ell = \left\langle |a_{\ell m}|^2 \right\rangle,$$

with spherical harmonic coefficients obtained from

$$\delta_I(\hat{\mathbf{n}}, E_\gamma) \equiv \frac{I_\gamma(\hat{\mathbf{n}}, E_\gamma)}{\langle I_\gamma\rangle\,(E_\gamma)} - 1 = \sum_{\ell=0}^{\infty}\sum_{m=-\ell}^{\ell} a_{\ell m}(E_\gamma) Y_{\ell m}(\hat{\mathbf{n}}),$$

or

$$\begin{aligned} a_{\ell m}(E_\gamma) &= \oint \mathrm{d}\Omega\, \delta_I(\hat{\mathbf{n}}, E_\gamma)\, Y^*_{\ell m}(\hat{\mathbf{n}}) \\ &= \frac{1}{\langle I_\gamma\rangle(E_\gamma)} \oint \mathrm{d}\Omega \int \frac{\mathrm{d}z}{H(z)} \left\{ [\rho^2\overline{\sigma v}](\hat{\mathbf{n}}, z) - \left\langle \rho^2\overline{\sigma v}\right\rangle(z) \right\} W((1+z)E_\gamma, z)\, Y^*_{\ell m}(\hat{\mathbf{n}}) \\ &= \frac{1}{\langle I_\gamma\rangle(E_\gamma)} \int \frac{\mathrm{d}z}{H(z)} \left\langle \rho^2\overline{\sigma v}\right\rangle(z)\, W((1+z)E_\gamma, z) \oint \mathrm{d}\Omega\, \delta_{\rho^2\overline{\sigma v}}(\hat{\mathbf{n}}, z) Y^*_{\ell m}(\hat{\mathbf{n}}) \end{aligned}$$

where, as usual,

$$\delta_{\rho^2\overline{\sigma v}} \equiv \frac{\rho^2\overline{\sigma v}}{\langle \rho^2\overline{\sigma v}\rangle} - 1.$$

Then

$$C_\ell(E_\gamma) = \frac{1}{\langle I_\gamma\rangle^2(E_\gamma)} \int \frac{\mathrm{d}z}{H(z)} \frac{\mathrm{d}z'}{H(z')} \left\langle \rho^2\overline{\sigma v}\right\rangle(z) \left\langle \rho^2\overline{\sigma v}\right\rangle(z') \times W((1+z)E_\gamma, z)\, W((1+z')E_\gamma, z')\, F_\ell(z,z'),$$

where

$$F_\ell(z,z') \equiv \int \mathrm{d}\Omega \mathrm{d}\Omega' \left\langle \delta_{\rho^2\overline{\sigma v}}(\hat{\mathbf{n}}, z)\delta_{\rho^2\overline{\sigma v}}(\hat{\mathbf{n}}', z')\right\rangle Y^*_{\ell m}(\hat{\mathbf{n}}) Y_{\ell m}(\hat{\mathbf{n}}').$$

It will soon be apparent why $F_\ell$ is independent of $m$. To simplify: write in terms of the power spectrum of the $\rho^2\overline{\sigma v}$ field,

$$\langle \delta_{\rho^2\overline{\sigma v}}(\hat{\mathbf{n}}, z)\delta_{\rho^2\overline{\sigma v}}(\hat{\mathbf{n}}', z')\rangle = \int \frac{\mathrm{d}^3\mathbf{k}}{(2\pi)^3} e^{irk\hat{\mathbf{n}}\cdot\hat{\mathbf{k}}} e^{-ir'k\hat{\mathbf{n}}'\cdot\hat{\mathbf{k}}} P_{\rho^2\overline{\sigma v}}(k,z,z'),$$

where $r$ is the distance to redshift $z$, given by (2.9), and $r'$ is the distance to redshift $z'$. Applying Rayleigh's formula

$$e^{irk\hat{\mathbf{n}}\cdot\hat{\mathbf{k}}} = 4\pi \sum_{\ell'=0}^{\infty} \sum_{m'=-\ell'}^{\ell'} i^{\ell'} j_{\ell'}(kr) Y^*_{\ell' m'}(\hat{\mathbf{k}}) Y_{\ell' m'}(\hat{\mathbf{n}})$$

and the orthogonality of spherical harmonics, one finds

$$F_\ell(z,z') = \frac{2}{\pi}\int_0^\infty \mathrm{d}k k^2 P_{\rho^2\overline{\sigma v}}(k,z,z') j_\ell(kr) j_\ell(kr').$$

We would not expect any significant correlation between regions of different redshift along a line-of-sight. One way this is realized is when $P_{\rho^2\overline{\sigma v}}$ is a slowly-varying function of $k$. In this case, it is a good approximation to treat it as a constant at wave number where $j_\ell(kr)$ is maximized. Since $j_\ell(x)$ has its maximum near $x = \ell$, we can approximate the power spectrum by its value at $k = \ell/r(z)$. Then orthogonality of the spherical Bessel functions

$$\int_0^\infty \mathrm{d}k k^2 j_\ell(kr) j_\ell(kr') = \frac{\pi}{2r^2}\delta(r-r') = \frac{\pi}{2r^2(z)} H(z)\delta(z-z')$$

gives

$$F_\ell(z,z') \approx \delta(z-z')\frac{H(z)}{\ell^2}\, k^2 P_{\rho^2\overline{\sigma v}}(k,z)\Big|_{k=\frac{\ell}{r(z)}}.$$

Thus, the angular power spectrum is finally expressed as

$$C_\ell(E_\gamma) \approx \frac{1}{\ell^2 \left\langle I_\gamma \right\rangle^2(E_\gamma)} \int \frac{\mathrm{d}z}{H(z)} W^2((1+z)E_\gamma, z) k^2 \overline{P}_{\rho^2\overline{\sigma v}}(k,z)\Big|_{k=\frac{\ell}{r(z)}}, \tag{4.12}$$

where we denote

$$\overline{P}_{\rho^2\overline{\sigma v}}(k,z) \equiv \left\langle \rho^2\overline{\sigma v}\right\rangle^2(z) P_{\rho^2\overline{\sigma v}}(k,z).$$

To derive the expression for the power spectrum of $\rho^2\overline{\sigma v}$, consider the correlation function at two points $\mathbf{r}_1, \mathbf{r}_2$ at the same redshift $z$.

$$\langle \delta_{\rho^2\overline{\sigma v}}(\mathbf{r}_1,z)\delta_{\rho^2\overline{\sigma v}}(\mathbf{r}_2,z)\rangle = \frac{\langle [\rho^2\overline{\sigma v}](\mathbf{r}_1,z)[\rho^2\overline{\sigma v}](\mathbf{r}_2,z)\rangle}{\left\langle \rho^2\overline{\sigma v}\right\rangle^2(z)} - 1$$

Recalling from the definition of the full halo correlation function (2.136) that

$$\langle p_h(\mathbf{R}_1, M_1, z) p_h(\mathbf{R}_2, M_2, z)\rangle = \frac{\mathrm{d}n}{\mathrm{d}M}(M_1,z)\frac{\mathrm{d}n}{\mathrm{d}M}(M_2,z)[\tilde{\xi}_h(\mathbf{R}_1, M_1, \mathbf{R}_2, M_2, z) + 1],$$

the 2-moment becomes

$$\begin{aligned}
&\left\langle [\rho^2\overline{\sigma v}](\mathbf{r}_1,z)[\rho^2\overline{\sigma v}](\mathbf{r}_2,z)\right\rangle \\
&\quad= \left\langle \sum_i \sum_j [\rho^2\overline{\sigma v}]_h(\mathbf{r}_1 - \mathbf{R}_i|M_i,z)[\rho^2\overline{\sigma v}]_h(\mathbf{r}_2-\mathbf{R}_j|M_j,z)\right\rangle \\
&\quad= \int \mathrm{d}^3\mathbf{R}_1 \mathrm{d}M_1 \mathrm{d}^3\mathbf{R}_2 \mathrm{d}M_2 [\rho^2\overline{\sigma v}]_h(\mathbf{r}_1-\mathbf{R}_1|M_1,z)[\rho^2\overline{\sigma v}]_h(\mathbf{r}_2-\mathbf{R}_2|M_2,z) \\
&\qquad\times \langle p_h(\mathbf{R}_1,M_1,z)p_h(\mathbf{R}_2,M_2,z)\rangle \\
&\quad= \int \mathrm{d}^3\mathbf{R}_1 \mathrm{d}M_1 \mathrm{d}^3\mathbf{R}_2 \mathrm{d}M_2 \frac{\mathrm{d}n}{\mathrm{d}M}(M_1,z)\frac{\mathrm{d}n}{\mathrm{d}M}(M_2,z) \\
&\qquad\times [\rho^2\overline{\sigma v}]_h(\mathbf{r}_1-\mathbf{R}_1|M_1,z)[\rho^2\overline{\sigma v}]_h(\mathbf{r}_2-\mathbf{R}_2|M_2,z)\xi_h(\mathbf{R}_1,M_1,\mathbf{R}_2,M_2,z) \\
&\qquad+ \int \mathrm{d}^3\mathbf{R}\mathrm{d}M \frac{\mathrm{d}n}{\mathrm{d}M}(M,z)[\rho^2\overline{\sigma v}]_h(\mathbf{r}_1-\mathbf{R}|M,z)[\rho^2\overline{\sigma v}]_h(\mathbf{r}_2-\mathbf{R}|M,z) \\
&\qquad+ \left\langle \rho^2\overline{\sigma v}\right\rangle^2(z),
\end{aligned}$$

where the second term in the last equality is due to the singularity in $\tilde{\xi}_h$, shown in (2.139). We therefore find the correlation function to be

$$\begin{aligned}
&\langle \delta_{\rho^2\overline{\sigma v}}(\mathbf{r}_1, z)\delta_{\rho^2\overline{\sigma v}}(\mathbf{r}_2, z)\rangle \\
&= \int \mathrm{d}^3\mathbf{R}\mathrm{d}M \frac{\mathrm{d}n}{\mathrm{d}M}(M, z)\frac{[\rho^2\overline{\sigma v}]_h(\mathbf{r}_1 - \mathbf{R}|M, z)[\rho^2\overline{\sigma v}]_h(\mathbf{r}_2 - \mathbf{R}|M, z)}{\langle \rho^2\overline{\sigma v}\rangle^2(z)} \\
&\quad + \int \mathrm{d}^3\mathbf{R}_1\mathrm{d}M_1\mathrm{d}^3\mathbf{R}_2\mathrm{d}M_2 \frac{\mathrm{d}n}{\mathrm{d}M}(M_1, z)\frac{\mathrm{d}n}{\mathrm{d}M}(M_2, z) \\
&\qquad \times \frac{[\rho^2\overline{\sigma v}]_h(\mathbf{r}_1 - \mathbf{R}_1|M_1, z)[\rho^2\overline{\sigma v}]_h(\mathbf{r}_2 - \mathbf{R}_2|M_2, z)}{\langle \rho^2\overline{\sigma v}\rangle^2(z)}\xi_h(\mathbf{R}_1, M_1, \mathbf{R}_2, M_2, z).
\end{aligned}$$

This simplifies significantly in momentum space. If we determine the Fourier transform of the halo profile

$$\mathcal{FT}\{[\rho^2\overline{\sigma v}]_h\}(k|M, z) = \int \mathrm{d}^3\mathbf{r} e^{-i\mathbf{k}\cdot\mathbf{r}}[\rho^2\overline{\sigma v}]_h(r|M, z),$$

the power spectrum can be written

$$\begin{aligned}
\overline{P}_{\rho^2\overline{\sigma v}}(k, z) &= \left\langle \rho^2\overline{\sigma v}\right\rangle^2(z)\int \mathrm{d}^3\mathbf{r}\,\langle \delta_{\rho^2\overline{\sigma v}}(\mathbf{r}_1, z)\delta_{\rho^2\overline{\sigma v}}(\mathbf{r}_1 + \mathbf{r}, z)\rangle\, e^{-i\mathbf{r}\cdot\mathbf{k}} \\
&= \int \mathrm{d}M \frac{\mathrm{d}n}{\mathrm{d}M}(M, z)\,\mathcal{FT}\{[\rho^2\overline{\sigma v}]_h\}^2(k|M, z) + \int \mathrm{d}M_1\mathrm{d}M_2 \frac{\mathrm{d}n}{\mathrm{d}M}(M_1, z)\frac{\mathrm{d}n}{\mathrm{d}M}(M_2, z) \\
&\quad \times \mathcal{FT}\{[\rho^2\overline{\sigma v}]_h\}(k|M_1, z)\mathcal{FT}\{[\rho^2\overline{\sigma v}]_h\}(k|M_2, z)P_h(k, M_1, M_2, z).
\end{aligned}$$

The first term, the one-halo term, dominates at small scales (large $k$) and the second term, the two-halo term, dominates at the large scales, in the linear regime. Therefore, in this expression, it is correct to use

$$P_h(k, M_1, M_2, z) = b(M_1, z)b(M_2, z)P_{\mathrm{lin}}(k, z)$$

if (2.141) holds true. The power spectrum is thus expressed as

$$\begin{aligned}
\overline{P}_{\rho^2\overline{\sigma v}}(k, z) &= \int \mathrm{d}M \frac{\mathrm{d}n}{\mathrm{d}M}(M, z)\left[\mathcal{FT}\{[\rho^2\overline{\sigma v}]_h\}(k|M, z)\right]^2 \\
&\quad + \left[\int \mathrm{d}M \frac{\mathrm{d}n}{\mathrm{d}M}(M, z)b(M, z)\mathcal{FT}\{[\rho^2\overline{\sigma v}]_h\}(k|M, z)\right]^2 P_{\mathrm{lin}}(k, z). \qquad (4.13)
\end{aligned}$$

For s-wave annihilation, the angular power spectrum reduces to

$$C_{0,\ell}(E_\gamma) = \frac{[\sigma v]_0^2}{\ell^2 \, \langle I_\gamma \rangle_0^2(E_\gamma)} \int \frac{\mathrm{d}z}{H(z)} W^2((1+z)E_\gamma, z) \, k^2 \overline{P}_{\rho^2,\rho^2}(k,z)\Big|_{k=\frac{\ell}{r(z)}} \tag{4.14}$$

with

$$\begin{aligned} k^2 \overline{P}_{\rho^2,\rho^2}(k,z) &= \int \mathrm{d}M \frac{\mathrm{d}n}{\mathrm{d}M}(M,z) \big[ k \, \mathcal{FT}\{\rho_h^2\}(k|M,z) \big]^2 \\ &\quad + \left[ \int \mathrm{d}M \frac{\mathrm{d}n}{\mathrm{d}M}(M,z) \, b(M,z) \left[ k \, \mathcal{FT}\{\rho_h^2\}(k|M,z) \right] \right]^2 P_{\mathrm{lin}}(k,z). \end{aligned} \tag{4.15}$$

The quantity $k \, \mathcal{FT}\{\rho_h^2\}(k|M,z)$ for the NFW halo profile that we use approaches a constant in the asymptotic $k \to \infty$ limit (see Appendix A.1). Note that, due to the normalization with mean intensity, the angular power spectrum does not depend on the value of the annihilation cross section, $[\sigma v]_0$. In fact, it is a desirable property of the angular power spectrum that it is independent of any uniform constants appearing in the intensity distribution, including constant intensity boost factors that may be associated with halo substructures or non-thermal relic effects, or intensity suppression factors due to p-wave suppression or co-annihilations during freeze out.

The angular power spectrum with p-wave annihilations is

$$C_\ell(E_\gamma) = \frac{[\sigma v]_0^2}{\ell^2 \, \langle I_\gamma \rangle^2(E_\gamma)} \int \frac{\mathrm{d}z}{H(z)} W^2((1+z)E_\gamma, z) \, k^2 \overline{P}_{\rho^2\left(1+\frac{\lambda b}{a}\sigma_u^2\right)}(k,z)\Big|_{k=\frac{\ell}{r(z)}} \tag{4.16}$$

where the power spectrum is

$$\begin{aligned} \overline{P}_{\rho^2\left(1+\frac{\lambda b}{a}\sigma_u^2\right)}(k,z) &= \int \mathrm{d}M \frac{\mathrm{d}n}{\mathrm{d}M}(M,z) \left[ \mathcal{FT} \left\{ \rho_h^2 + \frac{\lambda b}{a} \rho_h^2 \sigma_{uh}^2 \right\}(k|M,z) \right]^2 \\ &\quad + \left[ \int \mathrm{d}M \frac{\mathrm{d}n}{\mathrm{d}M}(M,z) b(M,z) \mathcal{FT} \left\{ \rho_h^2 + \frac{\lambda b}{a} \rho_h^2 \sigma_{uh}^2 \right\}(k|M,z) \right]^2 P_{\mathrm{lin}}(k,z) \end{aligned} \tag{4.17}$$

$$= \overline{P}_{\rho^2,\rho^2}(k,z) + 2\frac{\lambda b}{a} \overline{P}_{\rho^2,\rho^2\sigma_u^2}(k,z) + \left(\frac{\lambda b}{a}\right)^2 \overline{P}_{\rho^2\sigma_u^2,\rho^2\sigma_u^2}(k,z). \tag{4.18}$$

For clarification, the mixed power spectrum is

$$\begin{aligned}\overline{P}_{\rho^2,\rho^2\sigma_u^2}(k,z) &= \left\langle\rho^2\right\rangle(z)\left\langle\rho^2\sigma_u^2\right\rangle(z)P_{\rho^2,\rho^2\sigma_u^2}(k,z)\\ &= \int \mathrm{d}M\frac{\mathrm{d}n}{\mathrm{d}M}(M,z)\mathcal{FT}\{\rho_h^2\}(k|M,z)\mathcal{FT}\{\rho_h^2\sigma_{uh}^2\}(k|M,z)\\ &\quad+\left[\int \mathrm{d}M\frac{\mathrm{d}n}{\mathrm{d}M}(M,z)b(M,z)\mathcal{FT}\{\rho_h^2\}(k|M,z)\right]\\ &\quad\times\left[\int \mathrm{d}M\frac{\mathrm{d}n}{\mathrm{d}M}(M,z)b(M,z)\mathcal{FT}\{\rho_h^2\sigma_{uh}^2\}(k|M,z)\right]P_{\rm lin}(k,z).\end{aligned}$$

The biggest challenge in evaluating these expressions is the efficient evaluation of the Fourier transforms. Numerical integration of the Fourier transforms for each integrand sampling during the halo mass and redshift integrations is more time-intensive than is reasonable. See Appendix A for the efficient algorithms that I developed and implemented for evaluation of these transforms for the case of NFW halo profiles.

The relative contribution of the quadratic term in $\sigma v$ to the angular power spectrum is

$$\frac{C_\ell(E_\gamma|\sigma v=a+bv^2)}{C_{0,\ell}(E_\gamma|\sigma v=a)}=\frac{1+\frac{\lambda b}{a}\Delta_{C_\ell}^{(1)}(E_\gamma)+\left(\frac{\lambda b}{a}\right)^2\Delta_{C_\ell}^{(2)}(E_\gamma)}{\left[1+\frac{\lambda b}{a}\Delta_I(E_\gamma)\right]^2} \tag{4.19}$$

where each multipole $\ell$ has its own set of power spectrum coefficients

$$\Delta_{C_\ell}^{(1)}(E_\gamma) \equiv \frac{2\int\frac{\mathrm{d}z}{H(z)}W^2((1+z)E_\gamma,z)\,k^2\overline{P}_{\rho^2,\rho^2\sigma_u^2}(k,z)\Big|_{k=\ell/r(z)}}{\int\frac{\mathrm{d}z}{H(z)}W^2((1+z)E_\gamma,z)\,k^2\overline{P}_{\rho^2,\rho^2}(k,z)\Big|_{k=\ell/r(z)}}, \tag{4.20}$$

$$\Delta_{C_\ell}^{(2)}(E_\gamma) \equiv \frac{\int\frac{\mathrm{d}z}{H(z)}W^2((1+z)E_\gamma,z)\,k^2\overline{P}_{\rho^2\sigma_u^2,\rho^2\sigma_u^2}(k,z)\Big|_{k=\ell/r(z)}}{\int\frac{\mathrm{d}z}{H(z)}W^2((1+z)E_\gamma,z)\,k^2\overline{P}_{\rho^2,\rho^2}(k,z)\Big|_{k=\ell/r(z)}}. \tag{4.21}$$

It is more convenient to re-express the p-wave effect as

$$\frac{C_\ell(E_\gamma|\sigma v=a+bv^2)}{C_{0,\ell}(E_\gamma|\sigma v=a)}=1+\frac{\frac{\lambda b}{a}\overline{\Delta_{C_\ell}^{(1)}}(E_\gamma)+\left(\frac{\lambda b}{a}\right)^2\overline{\Delta_{C_\ell}^{(2)}}(E_\gamma)}{\left[1+\frac{\lambda b}{a}\Delta_I(E_\gamma)\right]^2} \tag{4.22}$$

where

$$\overline{\Delta^{(1)}_{C_\ell}}(E_\gamma) \equiv \Delta^{(1)}_{C_\ell}(E_\gamma) - 2\Delta_I(E_\gamma), \tag{4.23}$$

$$\overline{\Delta^{(2)}_{C_\ell}}(E_\gamma) \equiv \Delta^{(2)}_{C_\ell}(E_\gamma) - \Delta^2_I(E_\gamma). \tag{4.24}$$

It is interesting to note that this has a well-defined finite value in the vanishing $a$ limit, and that $\overline{\Delta^{(1)}_{C_\ell}}$ does not contribute there.

# 5 CALCULATIONS OF EXTRAGALACTIC GAMMA-RAYS DUE TO ANNIHILATING DARK MATTER*

## 5.1 Particle Models of Dark Matter Annihilation

Example models of dark matter considered in this dissertation are supersymmetric extensions of the standard model [114] with WIMP (weakly interacting massive particle) dark matter. In these extensions, each particle degree of freedom (DoF) in the standard model has an associated SUSY particle DoF with spin differing by 1/2. The spin-1/2 leptons and quarks have associated spin-0 sleptons and squarks, respectively. The spin-1 gauge bosons have spin-1/2 gaugino partners, and spinless Higgs bosons result in spin-1/2 higgsinos. Mixing terms in the gaugino and higgsino sector mean that the charged particles combine to produce states called charginos $\tilde{\chi}^{\pm}$, and the neutral charginos and higgsinos combine to form four neutralinos $\tilde{\chi}^{0}$.

SUSY extensions of the standard model were proposed as a solution to the hierarchy problem [115]. In the standard model, renormalization corrections to the bare Higgs particle mass, calculated to determine the measurable physical mass, were very large and needed to cancel the squared mass very precisely (to 34 orders of magnitude) to produce the expected physical mass of about 100 GeV. It was since discovered that the addition of SUSY modified the renormalization of the standard model gauge couplings (the strength of the forces) so that they unify at an energy scale of about $10^{16}$ GeV, known as the grand unified theory (GUT) scale [116]. This provides hints of a more complete particle physics theory, derived from a unified gauge theory at this scale. The most general theory would allow interactions

*Parts of this section are reprinted with permission from "*Effects of Velocity-Dependent Dark Matter Annihilation on the Energy Spectrum of the Extragalactic Gamma-ray Background*" by S. Campbell, B. Dutta, and E. Komatsu, Phys. Rev. D **82**, 095007 (2010), Copyright 2010 by The American Physical Society, "*Effects of P-wave Annihilation on the Angular Power Spectrum of Extragalactic Gamma-rays from Dark Matter Annihilation*" by S. Campbell and B. Dutta, Phys. Rev. D **84**, 075004 (2011), Copyright 2011 by The American Physical Society, and "*Extragalactic and galactic gamma rays and neutrinos from annihilating dark matter*" by R. Allahverdi, Sheldon Campbell, and Bhaskar Dutta, Phys. Rev. D **85**, 035004 (2012), Copyright 2012 by The American Physical Society.

that cause decay of the proton. The stability of the proton requires that there be some principle, such as R-parity symmetry [117], that disallows (or suppresses) these interactions involving an odd number of SUSY particles. A consequence of such a symmetry is that the lightest SUSY particle becomes stable (or very nearly so), and therefore a candidate to make up the dark matter in the Universe.

As explained in Section 1, the abundance of WIMP dark matter in the cosmos freezes out when the Universe becomes too cool to create new dark matter particles spontaneously, and the rate of expansion of the Universe exceeds the rate of particle annihilation. The dyanamical abundance of dark matter is calculated by numerical integration of the Boltzmann equation [59, 118]. The time at which the dark matter relic freezes out is specified in terms of the temperature of the Universe at freezeout $T_f$, defined to be the temperature at which the dark matter number density is twice the value it would be if it were still in thermal equilibrium. This freezeout temperature is often expressed in terms of $x_f \equiv m_{\rm DM}/T_f$. It typically takes values around $x_f \sim 20$–$25$. For a pure s-wave annihilation, the correct dark matter abundance is reached if $\sigma v = 3 \times 10^{-26}$ cm$^3$/s $= 10^{-36}$ cm$^2$. For other theories of annihilation, the mean velocity-weighted annihilation cross section at freezeout $[\overline{\sigma v}]_f$ must be near this value, to obtain the correct relic density for a thermally produced relic.

### 5.1.1 mSUGRA

A subset of possible SUSY extensions of the standard model are models of minimal supergravity (mSUGRA) [119]. In mSUGRA, scalar sfermions have a unified mass $m_0$ at the GUT scale, and the gauginos have a unified GUT mass $m_{1/2}$. Also united at the GUT scale are the trilinear couplings $A_0$ of the fermion-sfermion-gaugino interactions. There must be two Higgs superfields to cancel anomalies. The up-type Higgs couples the weak isospin 1/2 fermions and generates a vacuum expectation value (VEV) $v_1$. Likewise, the down-type Higgs couples the weak isospin -1/2 fermions and generates a VEV $v_2$. The model can be specified by the ratio $\tan\beta = v_1/v_2$, the values of $m_0$, $m_{1/2}$, and $A_0$, and the sign of the mass parameter

$\mu$ coupling the two Higgs superfields in the superpotential. This parameter space of four parameters and one sign is currently being actively probed by the ATLAS [120] and CMS [121] experiments at the Large Hadron Collider.

At the present time, there is plenty of parameter space of mSUGRA that satisfies all current particle physics, astrophysical, and cosmological constraints, with a variety of phenomenologies (although, if the new hints of a light Higgs particle with mass around 125 GeV are confirmed [122], the parameter space will become much more heavily constrained). In these regions, the dark matter particle is the lightest neutralino $\tilde{\chi}_1^0$. Examples of models with vanishing $A_0$ and positive $\mu$ will be considered. When describing annihilation spectra, the focus is on universal masses that are not so large as to result in a dark matter particle massive enough to produce significant top quarks from annihilations.

In the three-dimensional parameter space of $m_0$, $m_{1/2}$, and $\tan\beta$, the parameter space is typically broken up into four main regions: the bulk region, the focus point (also known as hyperbolic) region, the co-annihilation region, and the funnel region. In these regions, the dark matter particle turns out to be the lightest neutralino $\tilde{\chi}_1^0$.

In the bulk region, both $m_0$ and $m_{1/2}$ are relatively small. The neutralino is nearly pure bino (the gaugino which is the supersymmetric partner of the weak hypercharge gauge boson), and annihilates predominantly to bottom anti-bottom quark pairs $b\bar{b}$, secondarily to tau anti-tau lepton pairs $\tau^+\tau^-$ (more so at larger $\tan\beta$). These processes in the bulk region give the correct annihilation cross section to account for the relic density, if it were thermally produced.

Generically, larger values of $m_0$ and $m_{1/2}$ result in theories with larger mass dark matter that have smaller annihilation cross sections, and therefore would result in more thermally produced dark matter in the Universe than is observed today. However, when considered carefully, one finds that other parameter space does result in the correct relic density, due to different mechanisms [123], according to the parameter space of interest.

The focus point region [124] has a branch where $m_{1/2}$ remains small and $m_0$ is allowed to increase. As $m_0$ does so, the lightest neutralino gains a larger Higgsino component, which opens up additional annihilation channels. Here, annihilation dominantly produces $W^+W^-$ bosons, with small branching fractions also producing $b\bar{b}$ quark pairs and $ZZ$ boson pairs, for small to moderate $\tan\beta$. For large $\tan\beta$, the Higgsino component of the lightest neutralino is again small in this region, but Bino annihilation is enhanced by an increased coupling to the pseudoscalar Higgs $A$ and annihilation is again dominated by $b\bar{b}$ and $\tau^+\tau^-$.

There is a threshold where $m_0$ becomes too small and one of the supersymmetric partners of the tau (stau $\tilde{\tau}$) becomes the lightest supersymmetric particle, which is electrically charged and therefore cosmologically disallowed. This threshold increases with $m_{1/2}$. Near this boundary, the $\tilde{\tau}$ mass is only slightly larger than the $\tilde{\chi}_1^0$ mass, enhancing the co-annihilation interaction cross section between these particles. The $\tilde{\tau}$'s present in the early Universe co-annihilate with the $\tilde{\chi}_1^0$'s, reducing the neutralino density to the correct value. This parameter space is the stau-neutralino co-annihilation region [125]. When $A_0 > 0$, there is parameter space at low $m_{1/2}$ where a supersymmetric partner of the top quark (stop $\tilde{t}$) becomes lighter than $\tilde{\chi}_1^0$. The stop-neutralino co-annihilation region [126] is near this boundary. In these parameter spaces, $\tilde{\chi}_1^0$ is again nearly pure Bino, and mostly $b\bar{b}$ and some $\tau^+\tau^-$ are produced from annihilations. Because there are no $\tilde{\tau}$ or $\tilde{t}$ particles present today, they no longer contribute to annihilations and the effective annihilation cross section of the neutralinos is reduced from its value at freezeout. Additionally, at low $\tan\beta$, annihilation is dominated by t-channel sfermion exchange, which is helicity-suppressed [127]. The presence of a strong p-wave annihilation component brings the annihilation cross section up to its needed value at freezeout, but slow relative motions of the particles today do not allow the p-wave to contribute. In these cases, the annihilation cross-sections are quite small, which make the rates of annihilations low and the intensity of annihilation radiation much more difficult to detect. The situation improves at large $\tan\beta$ where annihilation via $A$ is a stronger component, lifting much of the helicity suppression.

The final parameter space, the heavy Higgs or $A$ annihilation funnel regions, occurs

where the mass of one of the Higgs bosons is near half the $\tilde{\chi}_1^0$ mass, resulting in a Breit-Wigner resonance enhancement of the annihilations at freezeout interaction energies [128]. Since the resonance does not enhance the cross section today, the annihilation cross sections are again lower in the present epoch for dark matter models of this parameter space.

### 5.1.2 Gauged $U(1)_{B-L}$ Model

Another paradigm to be considered, which is interesting in the context of neutrino radiation production, is the $U(1)_{B-L}$ extension of the MSSM [129]. Here, baryon number $B$ minus lepton number $L$ is a gauged charge with associated gauge boson $Z'$ that couples to baryons and leptons, according to their $B-L$ charges with gauge coupling $g'$. This extension requires the presence of right-handed neutrinos $N^c$ for anomaly cancellation, providing a natural framework to explain neutrino masses and oscillations. In order for this new internal symmetry to be spontaneously broken, two new Higgs superfields $\mathbf{H}_1'$ and $\mathbf{H}_2'$ must be introduced, which are standard model neutral and oppositely charged under $B-L$ for anomaly cancellation. They are coupled by a new mass parameter $\mu'$ in a new term added to the MSSM superpotential. The physical neutrinos $\nu$ are light, but $N^c$ heavy, by the type I see-saw mechanism [130]. This requires a Majorana mass for the $N^c$, which does not obey the $B-L$ symmetry; however, the $N^c$ can have a Yukawa coupling to another Higgs field with lepton number $-2$, which we identify with $H_2'$. This Higgs will gain a vacuum expectation value around 1 TeV, producing the $N^c$ Majorana mass and generating the appropriate neutrino spectrum. Thus, by defining supersymmetric partners for each of the introduced new fields and putting them in chiral supermultiplets, the minimal $U(1)_{B-L}$ extension to the MSSM has superpotential [131]

$$W = W_{\text{MSSM}} + y_D \mathbf{N}^c \mathbf{H}_u \mathbf{L} + f \mathbf{H}_2' \mathbf{N}^c \mathbf{N}^c + \mu' \mathbf{H}_1' \mathbf{H}_2' \tag{5.1}$$

where $\mathbf{H}_u$ is the Higgs superfield of the MSSM that gives mass to the up-type quarks, and $\mathbf{L}$ is the superfield containing the left-handed leptons. Note that flavor and the weak isospin $SU(2)_L$ indices have been suppressed.

There exists parameter space in this framework where the LSP is a supersymmetric partner of $N^c$, the right sneutrino $\tilde{N}$. If the $N^c$ mass is less than the $\tilde{N}$ mass, then annihilations could produce a large number of $N^c$ from neutralino exchange, which would then decay according to the particular model considered. In any case, one would expect many direct neutrinos to be produced, while photons would only be produced secondarily.

Alternatively, $\tilde{N}$ s-channel annihilation via the $B - L$ $Z'$ boson would produce mostly leptons (including neutrinos) and some hadrons, which would then radiate photons and additional neutrinos.

## 5.2 Mean Extragalactic Gamma-ray Intensity and Angular Power Spectrum for Annihilation with S-wave and P-wave

### 5.2.1 Example mSUGRA Dark Matter Models

To begin, consider three mSUGRA models with $\tan\beta = 10$, $A_0 = 0$, and $\mu > 0$: one in the focus point region with neutralino dark matter particle mass $m_{\tilde{\chi}_1^0} = 150$ GeV, one with the same particle mass in the stau-neutralino co-annihilation region, and a third model in the bulk region with $m_{\tilde{\chi}_1^0} = 62.3$ GeV. Properties of these models are given in Table 2.

All mSUGRA particle spectra, cross sections, annihilation spectra, and relic densities are calculated using DarkSUSY 5.0.5 [132], interfaced with ISAJET 7.78 [133], and FeynHiggs 2.6.5.1 [134]. In Figure 5, the velocity-weighted annihilation cross section is shown for the co-annihilation region model, as a function of the square relative velocity of the annihilating particles in the center-of-momentum frame. The mean square relative velocity of the dark matter at freezeout is indicated by the gold vertical line. At energies below the freezeout energy, the annihilation cross section, indicated by the thick blue line, is well-described by $\sigma v = a + bv^2$, shown by the thin blue line using the values for $a$ and $b$ implicated in Table 2. There is a strong Breit-Wigner annihilation resonance, due to the

pseudoscalar Higgs particle, at an energy above freezeout. The resonance is unimportant for this model, but in the funnel region of parameter space, the energy of this resonance coincides with the freezeout energy. Above the rest energy of a $\tilde{\chi}_1^0$ and a $\tilde{\tau}$, neutralino co-annihilations with stau particles are kinematically allowed. The thick magenta line shows the effective annihilation cross section with co-annihilations during the early Universe. The coannihilations bring the rate of neutralino annihilations up to the needed rate to provide the correct thermally-produced dark matter relic density.

For the initial calculations, ΛCDM cosmological parameters from WMAP5 [11] were used, neglecting primordial neutrino effects: $\Omega_\Lambda = 0.721$, $\Omega_b = 0.0462$, $\Omega_c = 1 - \Omega_\Lambda - \Omega_b$, $h = 0.701$, $\sigma_8 = 0.817$, and $n_s = 0.96$. The minimal halo mass scale is set to $M_{\rm min} = 10^6 M_\odot$, and the effects due to the opacity of the Universe are neglected, to be considered later since they do not affect the discussion. (Note that WMAP7 results are applied in the calculations of Section 6. The photon opacity and a smaller minimum halo mass of $10^{-6} M_\odot$ are applied from Section 5.2.4 onward, except for the results of Section 5.3.)

Table 2: Sample mSUGRA models with parameters $\tan\beta = 10$, $A_0 = 0$, and $\mu > 0$. The first two columns show the input model parameters. The other columns show the calculated dark matter properties that are relevant to this discussion. The last column shows the thermally-averaged $\sigma v$ at freezeout, including co-annihilations.

| mSUGRA Region | $m_0$ (GeV) | $m_{1/2}$ (GeV) | $m_{\tilde{\chi}_1^0}$ (GeV) | $a$ ($\times 10^{-26}$ cm$^3$/s) |
|---|---|---|---|---|
| Focus Point | 2569 | 395 | 150 | 1.9 |
| Bulk | 79 | 171 | 62.3 | 0.27 |
| Co-annihilation | 79 | 373.7 | 150 | 0.0019 |
| **mSUGRA Region** | $\frac{b}{a}$ | $\Omega_c h^2$ | $x_f$ | $[\overline{\sigma v}]_f$ ($\times 10^{-26}$ cm$^3$/s) |
| Focus Point | 1.8 | 0.114 | 22.9 | 2.6 |
| Bulk | 57.5 | 0.114 | 22.5 | 3.8 |
| Co-annihilation | 378.8 | 0.113 | 24.0 | 5.8 |

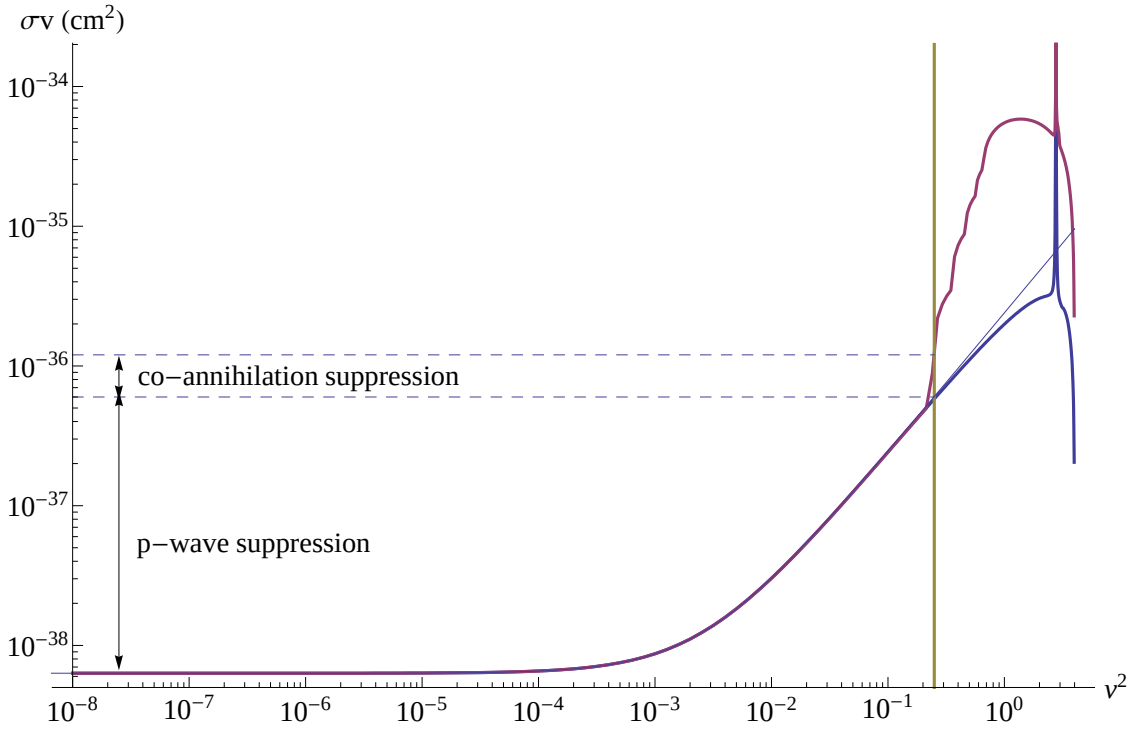


Figure 5: The effective relative-velocity-weighted annihilation cross section for a 150 GeV neutralino dark matter particle in the mSUGRA model with $\tan\beta = 10$ and $A_0 = 1$ in the co-annihilation region. It results in a relic density of $\Omega_c h^2 = 0.113$. The thick blue line shows the cross section involving annihilations between $\tilde{\chi}_1^0$ particles only. The thin blue line shows the best fit $a + bv^2$ using values in Table 2. The magenta line indicates the effective annihilation, including co-annihilations, during the early Universe. The vertical gold line indicates the value of the mean square relative particle velocities at the time of freezeout. The suppression of the low-energy cross section due to co-annihilations at freezeout, and due to the strength of the p-wave during freezeout, are each indicated.

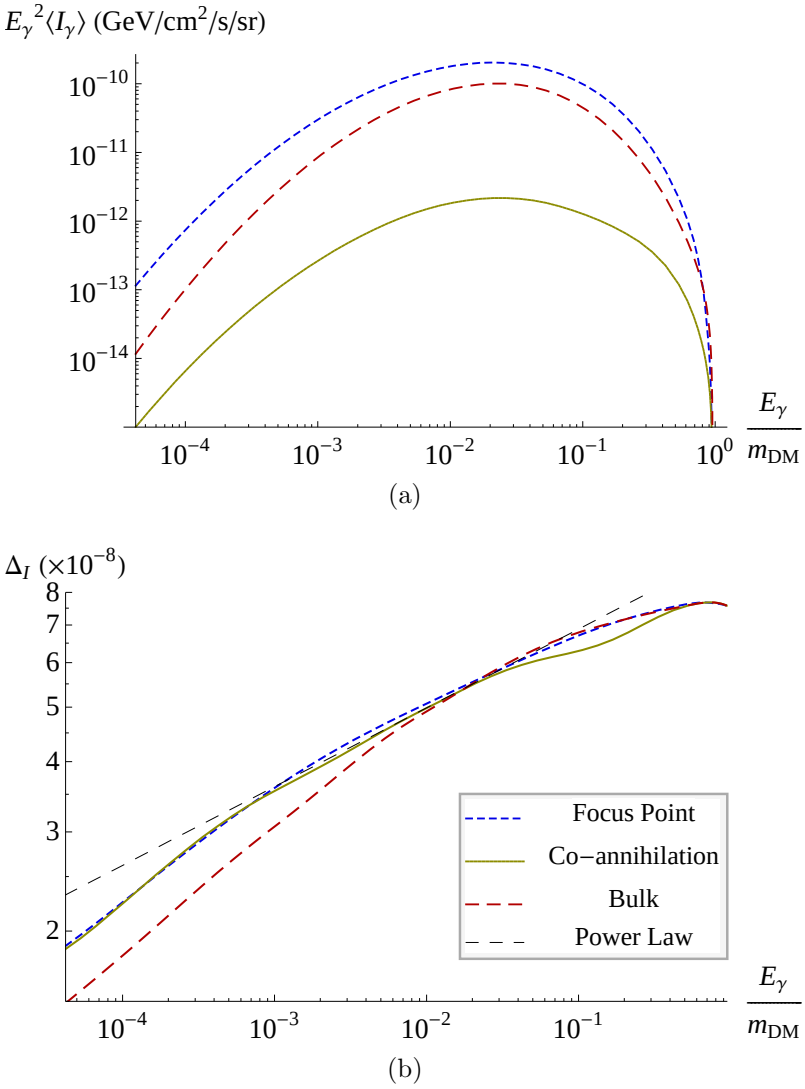


Figure 6: Sample gamma-ray mean intensities and p-wave relative contributions of extragalactic dark matter annihilation for three mSUGRA models. (a) Gamma-ray intensity spectrum of extragalactic dark matter annihilation for the three mSUGRA models (at $\tan\beta = 10$, $A_0 = 0$, and $\mu > 0$), which have neutralino dark matter with the properties given in Table 2. (b) $\Delta_I$ vs. $E_\gamma$ for those three models. For comparison, a power law $\propto (E_\gamma/m_{\rm DM})^{0.14}$ is also plotted.

The resulting intensity spectra of gamma-rays from extragalactic dark matter annihilation are shown in Figure 6a for the three models in Table 2. The differences between these models can be described broadly in terms of five effects.

The first is the normalization shift due to the difference in particle mass. The mean intensity at a particular gamma-ray energy per particle mass scales approximately like $m_{\rm DM}^{-3}$ (as in Equation (3.8)), if opacity effects are negligible. Therefore, the bulk model intensity has a factor of about 14 over the other two models, due to its smaller particle mass.

The second and third effects are also normalization shifts that cause changes in the value of the s-wave component $a$ of the velocity-weighted annihilation cross section. The main effect is the p-wave suppression: the fact that $a$ must be smaller for models with larger p-wave strengths $b/a$ in a thermally-produced relic. The mean square relative particle velocities at freezeout are $\overline{v^2} = 6/x_f$. Therefore, applying $\overline{\sigma v} = a + b\overline{v^2}$ at freezeout, one finds

$$a = \frac{[\overline{\sigma v}]_f}{1 + \left(\frac{b}{a}\right)\frac{6}{x_f}}. \tag{5.2}$$

For thermally-produced dark matter, $a$ becomes an approximate measure of the p-wave strength.

$$a \approx \frac{3 \times 10^{-26}\ \mathrm{cm}^3/\mathrm{s}}{1 + \frac{1}{4}\frac{b}{a}}$$

The p-wave suppression of the cross section for the co-annihilation model is indicated in Figure 5, and is seen to be approximately a factor of $10^{-2}$. Also seen in that figure is the third effect, the suppression of $a$ in the co-annihilation model, that is due to the presence of co-annihilations in the early Universe. In this model, $a$ must be reduced by an additional factor of about 1/2 in order to be consistent with the conditions at the time of freezeout. Other enhancements at freezeout, such as annihilation resonances, would also suppress $a$ for thermally-produced dark matter.

The fourth effect is dependence of the shape of the spectrum on the velocity-dependence of the cross section. With p-wave annihilation, regions of space

where dark matter particles have higher relative velocities will annihilate at increased rates because of the larger cross section. The effect of p-wave annihilation on the spectrum shape is expressed in Equations (4.10)–(4.11). Figure 6b plots $\Delta_I$ for the three models in consideration. The only quantities that contribute to variations among them are their different annihilation spectra. The $\Delta_I$ for these models are very nearly the same value close to the peak energy of the spectrum. For comparison, also plotted is the power law $\Delta_I = 0.95 \times 10^{-7} \left(\frac{E_\gamma}{m_{\rm DM}}\right)^{0.14}$, which approximately describes $\Delta_I$ near the peak of the spectrum. Because $\Delta_I$ is increasing with gamma-ray energy, the p-wave increases the intensity of higher energy gamma-rays more than lower energy, thereby making the spectral shape harder than if the cross-section were purely s-wave.

Referring to Equation (4.10), the magnitude of $\Delta_I \sim 10^{-7}$ informs that the p-wave will only have significant effect on the shape of the intensity spectrum if $\lambda b/a \gtrsim 10^7$, or if the p-wave strength exceeds $b/a \gtrsim 10^6$. This is consistent with the largest significantly present relative velocities that affect the cosmic annihilation signal to be $v \lesssim 10^{-3}$ in our halo model. It follows that the p-wave does not affect the shapes of the spectra in Figure 6a in any observable way. Their variations in shape can, therefore, only be due to differences in their annihilation spectrum—the fifth effect to be observed.

Of these five effects, the one most dominant is the p-wave suppression. The total effect that a p-wave component in the annihilation cross section has on the intensity of extragalactic gamma-rays from annihilations of a thermal dark matter relic is

$$\frac{\langle I_\gamma \rangle (E_\gamma|\sigma v = a + bv^2)}{\langle I_\gamma \rangle (E_\gamma|\sigma v = [\overline{\sigma v}]_f)} = \frac{a}{[\overline{\sigma v}]_f} \frac{\langle I_\gamma \rangle (E_\gamma|\sigma v = a + bv^2)}{\langle I_\gamma \rangle (E_\gamma|\sigma v = a)} = \frac{1 + \left(\frac{b}{a}\right) \lambda \Delta_I(E_\gamma)}{1 + \left(\frac{b}{a}\right) \frac{6}{x_f}}, \quad (5.3)$$

using (4.10) and (5.2). This p-wave suppression of the intensity is plotted in Figure 7a for mild values of $b/a$, with $x_f = 24$ and $\lambda \Delta_I = 5 \times 10^{-7}$. Since $\lambda \Delta_I \ll 6/x_f$, there are 3 regions of interest, as can be seen explicitly in Figure 7b:

1. When $b/a \ll x_f/6 \sim 4$, the theory is s-wave dominated, and the p-wave contributes very little to both the relic density calculation and the

annihilation photon intensity spectrum. When $b/a \lesssim 1$, the intensity suppression is linear in $b/a$ with slope $-6/x_f \sim -1/4$.

2. When $x_f/6 \ll b/a \ll (\lambda\Delta_I)^{-1}$, it is important to include the p-wave for the accurate calculation of the relic density, resulting in a suppression of the s-wave of the annihilation cross section. But the p-wave contribution to the shape of the intensity spectrum is negligible in this region.

3. When $b/a \gg (\lambda\Delta_I)^{-1} \sim 10^6$, the theory is p-wave dominated and the s-wave component contributes little to both calculations. In this regime, p-wave suppression is maximal with a suppression factor of $x_f\lambda\Delta_I/6 \sim x_f\Delta_I \sim 10^{-6}$ relative to an equivalent s-wave dominated theory.

In summary, for each of the three regions, the p-wave suppression behaves as

$$\frac{\langle I_\gamma\rangle\left(E_\gamma|\sigma v = a + bv^2\right)}{\langle I_\gamma\rangle\left(E_\gamma|\sigma v = [\overline{\sigma v}]_f\right)} \approx \begin{cases} 1 - \frac{6}{x_f}\left(\frac{b}{a}\right) & \frac{b}{a} \ll \frac{x_f}{6}, \\ \left[\frac{6}{x_f}\left(\frac{b}{a}\right)\right]^{-1} & \frac{x_f}{6} \ll \frac{b}{a} \ll [\lambda\Delta_I(E_\gamma)]^{-1}, \\ \frac{x_f}{6}\lambda\Delta_I(E_\gamma) & \frac{b}{a} \gg [\lambda\Delta_I(E_\gamma)]^{-1}. \end{cases} \tag{5.4}$$

It follows that the extragalactic intensities for the three mSUGRA models considered can be calculated as s-wave theories with $\sigma v = a$, with the appropriate value of $a$ for each model. It is interesting to consider whether there are regions of parameter space in the Minimally Supersymmetric Standard Model (MSSM) (where each supersymmetric partner of standard model particles has its own mass, and each allowed supersymmetric interaction beyond the standard model and each allowed soft supersymmetry breaking interaction has its own coupling constant) that has a very large p-wave strength of $\frac{b}{a} \gtrsim 10^6$.

### 5.2.2 Large P-wave Strengths in the MSSM

The first step is recognizing that neutralino dark matter has certain annihilation channels where the s-wave components are helicity-suppressed. For annihilation

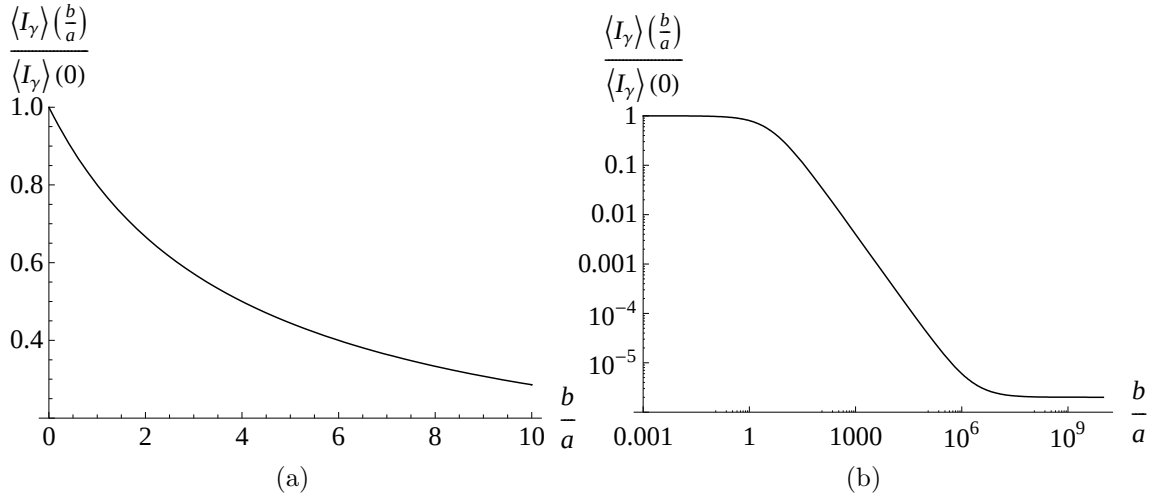


Figure 7: (a) The p-wave suppression factor for the mean intensity of extragalactic dark matter annihilation photons [Eq. (5.3)] as a function of $b/a$, for typical values of $x_f = 24$ and $\lambda\Delta_I = 5 \times 10^{-7}$. The suppression is shown here for small values of $b/a$. (b) The same plot as in (a), but on log scale and for a wider range of $b/a$.

into a fermion anti-fermion pair, the s-wave annihilation component is suppressed by $(m_f/m_{\tilde{\chi}_1^0})^2$, the squared ratio of the fermion mass to the neutralino mass. This includes t and u-channel sfermion exchange, and s-channel mediation by the $Z$ boson or neutral Higgs bosons. Each contribution to the total cross-section amplitude has an approximate factor of $(m_M/m_{\tilde{\chi}_1^0})^{-2}$, where $m_M$ is the mediator mass. This factor enhances the channels mediated by the $Z$ and lightest Higgs, but suppresses the sfermion and heavy Higgs channels.

In the parameter space where the neutralino is very nearly pure bino and the magnitude of the Higgs superpotential coupling $\mu$ is much larger than the first soft gaugino mass $M_1$, the annihilation is dominated by the sfermion exchange. This allows the contributions of $Z$ or Higgs mediation to be greatly reduced, as well as all other annihilation channels that are not helicity-suppressed.

In the case where the sfermion masses are unified at the GUT scale, the heavy third generation fermion channels dominate the s-wave annihilations, due to their

larger masses when compared with the other fermions. In parameter space where the neutralino is nearly pure bino, squark masses are much larger than sfermion masses. However, the $b$ quark is sufficiently massive when compared with the $\tau$ lepton that it still has a significant branching ratio. Also, remaining modest amounts of $Z$ mediation will add to the $b\bar{b}$ production. The production of $t$ quarks becomes important if the neutralino is massive enough to kinematically allow it.

We can increase $b/a$ further by taking advantage of the sfermion mass suppression of the cross section and considering large non-universal 3rd generation sfermion masses at the GUT scale. In this parameter space of the MSSM, where the neutralino is nearly pure bino and annihilation into 3rd generation fermions is suppressed, we would expect the dominant contribution to the s-wave component of the cross section to be proportional to $(m_\mu/m_{\tilde{\chi}_1^0})^2 \lesssim 10^{-6}$, relative to the p-wave component.

However, there are loop processes that become the dominant s-wave contribution at this point, generated when the fermion anti-fermion pair close the loop and two gauge bosons come off the internal lines [135], such as two photons, photon and $Z$, or two gluons. The amplitude due to these loops provides a hard lower bound on the s-wave component of the cross section on the order of $10^{-29}$ cm$^3$/s, keeping $b/a \lesssim 10^4$ in the MSSM parameter space that satisfies the relic density constraint. Correspondingly, the p-wave intensity term will have a magnitude of less than a percent of the s-wave approximation. However, as already explained, such large values of $b/a$ still require a significant reduction in the s-wave component of the cross section in order to satisfy the relic density constraint.

Therefore, it can be concluded that, in the MSSM, the s-wave approximation of the intensity calculation in Eq. (4.6) gives very accurate results in the MSSM, as long as the correct annihilation cross section is used. The p-wave suppression of the s-wave component is very significant in parts of the MSSM parameter space. The intensity is further suppressed in parameter space with significant co-annihilations at dark matter freezeout, or with a significant Breit-Wigner resonance at freezeout.

### 5.2.3 A P-wave Dominated Theory in MSSM$\otimes U(1)_{B-L}$

To find models with very strong p-wave annihilation, consider the $U(1)_{B-L}$ extension of the MSSM. In this model, the lightest supersymmetric particle (LSP) can be the lightest right sneutrino or the lightest neutralino. Here, a parameter space where the right sneutrino is the LSP is considered. Thus, the dark matter is neutral to standard model charges and the only gauge interaction is with the $Z'$ (and $B-L$ neutralinos) via its lepton charge. It also interacts with the $B-L$ Higgs fields. Possible s-wave annihilation processes are annihilation into neutrinos mediated by $B-L$ neutralinos, and into $B-L$ Higgs via s-channel $Z'$ or Higgs fields. However, there is parameter space where the $B-L$ Higgs' and neutralinos are massive compared to twice the sneutrino mass, and can be neglected in this discussion. In this region, sneutrino annihilation is (at tree level) exclusively s-channel via the $Z'$ into fermion anti-fermion pairs. In this process, s-wave annihilation is completely forbidden. Therefore, this is an example of a pure p-wave annihilation process.

At one loop, an s-wave component is generated, but is strongly coupling-suppressed when compared with the tree level p-wave cross section, with additional factors of $\alpha^4$ or $g'^4\alpha^2$, where $\alpha$ is the fine structure constant (or the strong force constant in the case where gluons are emitted from quarks, instead of photons) and $g'$ is the $U(1)_{B-L}$ gauge coupling, which is taken to be 0.4 in the calculation. Thus, we would estimate $b/a$ in this scenario to be $\gtrsim 10^8$, completely p-wave dominated. A calculation of the intensity spectrum due to annihilations at the tree level, neglecting the small s-wave component altogether, is carried out.

For our example, consider a model with spectrum $m_{\tilde{\nu}} = 550$ GeV, $M_{Z'} = 1300$ GeV, and $Z'$ width $\Gamma_{Z'} = 17$ GeV. Here, the sneutrino is at a near resonance with the $Z'$, which allows the relic density constraint to be satisfied. The annihilation cross section and relic density calculations were performed using a Mathematica program written by Bhaskar Dutta. The photon spectrum per annihilation was simulated with Pythia 8.135 [136]. The resulting intensity spectrum is shown in the bottom curve of Figure 8a.

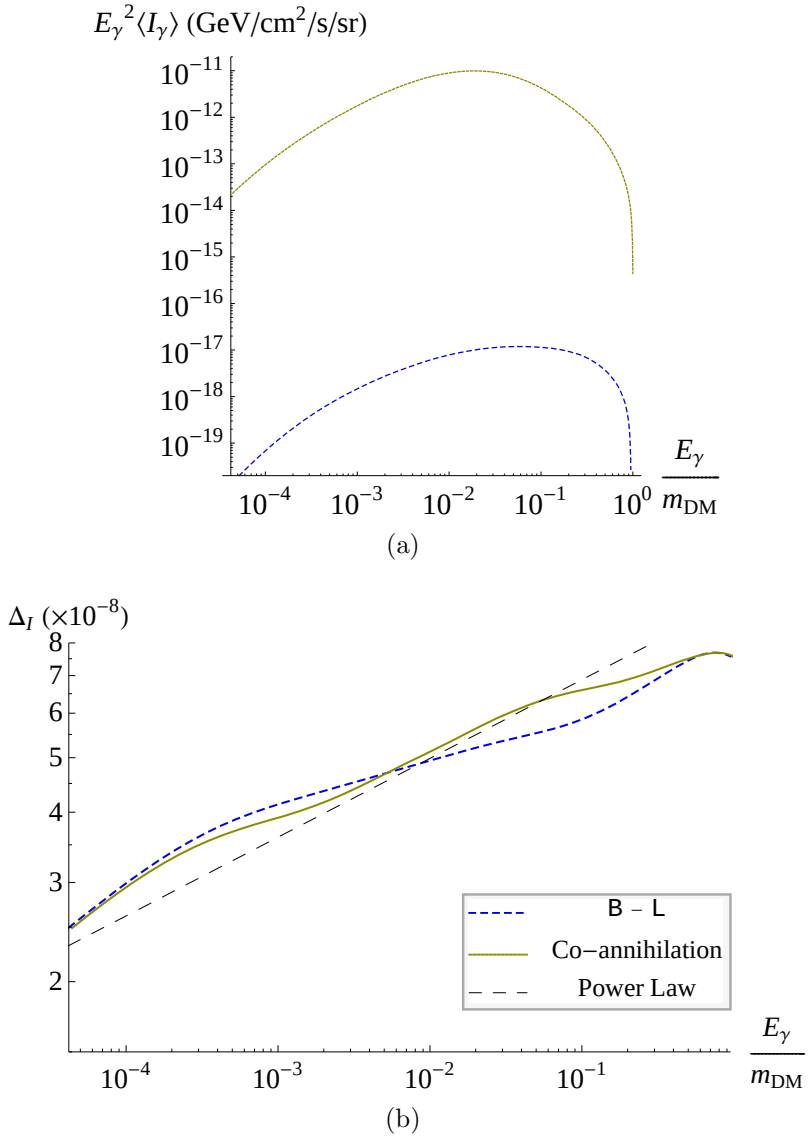


Figure 8: More sample extragalactic annihilation gamma-ray spectra. (a) The lower curve is the intensity spectrum for a pure p-wave process. This scenario is realized in the MSSM$\otimes U(1)_{B-L}$ with right handed sneutrino dark matter. The sneutrino, here of mass 550 GeV, annihilates through a $Z'$ resonance into fermion anti-fermion pairs. The $Z'$ for this plot had mass 1300 GeV and width 17 GeV. For contrast, the upper curve is due to annihilations of a 550 GeV neutralino in the co-annihilation region of mSUGRA with $\tan\beta = 50$, $A_0 = 0$, and $\mu > 0$. This model has a relatively mild p-wave strength of $b/a = 4.8$. (b) The associated $\Delta_I$ for the two models, given by Eq. (4.11). For reference, the same power law as in Figure 6b is also shown.

The low intensity in this model shows the expected full p-wave suppression factor of nearly 6 orders of magnitude. For comparison, the spectrum for an mSUGRA co-annihilation region model at high $\tan\beta = 50$ is shown. The dark matter is a neutralino, also of mass 550 GeV. It has a p-wave strength of $b/a = 4.8$, which is relatively weak when compared with the low $\tan\beta$ model considered earlier. This is because of a stronger neutralino coupling to the pseudoscalar Higgs boson. Here, the differences in spectrum shape between the two models will be due both to differences in photon spectrum per annihilation, and the fact that the lower intensity curve is directly coupled to the current dark matter velocity distribution, whereas the upper curve is not.

### 5.2.4 Inclusion of the Opacity Effect

An important effect that was neglected in Section 5.2.1 is the opacity of the Universe to gamma-rays. As energetic photons propagate, they interact with background fields such as the cosmic microwave background. A fitting function for the optical depth $\tau(E_\gamma, z)$ is available [104], and it was applied to the annihilation intensity calculations.

Figure 9 shows how these changes affect the intensity spectrum and p-wave $\Delta_I$ for each of the 5 SUSY models we considered. The inclusion of microhalos down to a mass of $10^{-6} M_\odot$ increases the annihilation intensity and slightly lowers $\Delta_I$. The opacity has little effect on the intensity of the three smaller mass models, but introduces a much sharper cutoff in the intensity spectrum for the two higher particle mass models. The effect of opacity on $\Delta_I$ is observed to depend strongly on the particle mass of the dark matter, based on how models with the same particle mass group together. In particular, the opacity pushes up the value of $\Delta_I$ to near its maximum value, and this occurs at a lower photon energy for higher mass dark matter particles.

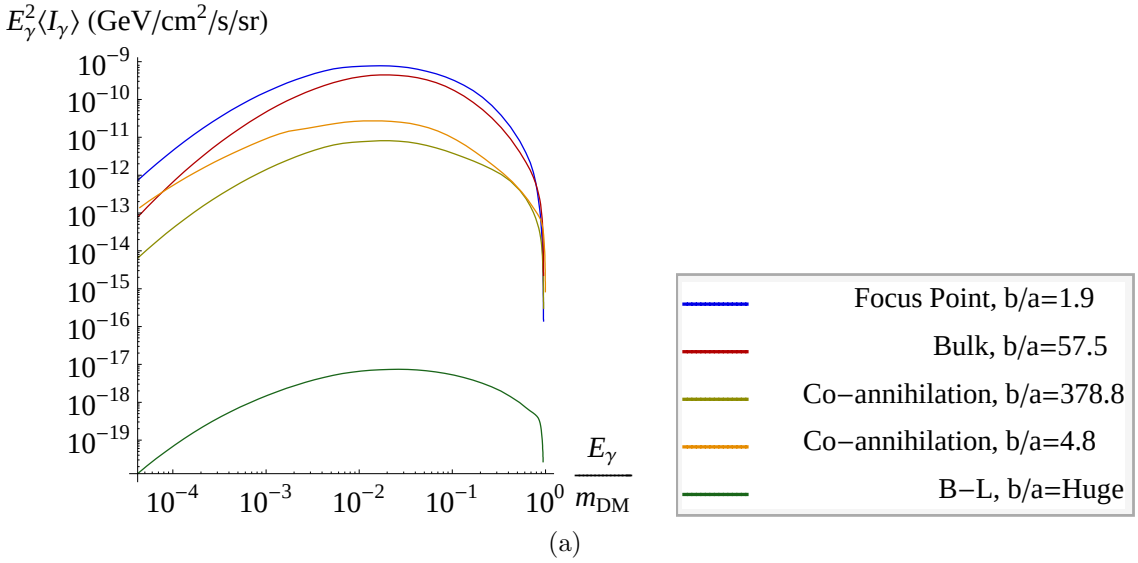


(a)

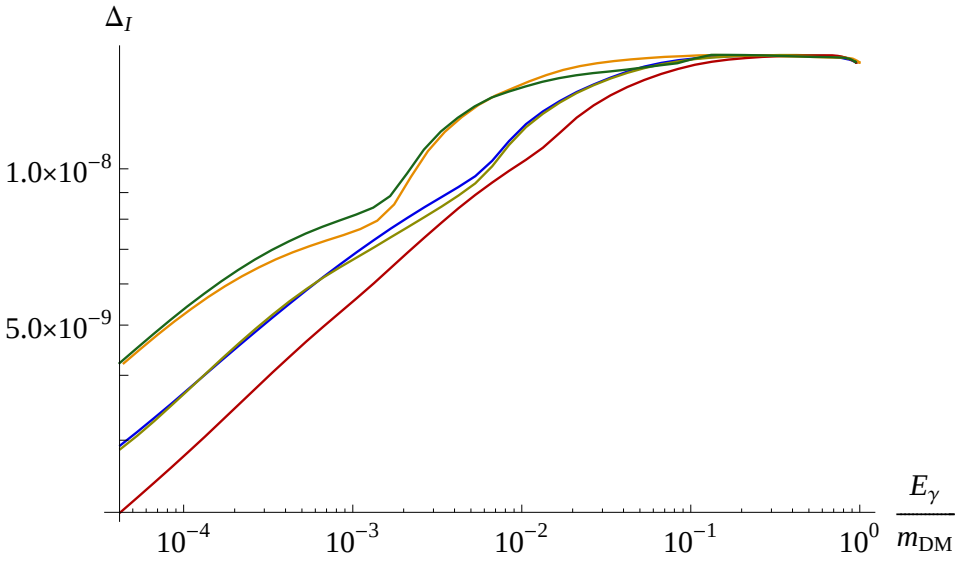


(b)

Figure 9: Sample spectra with photon opacity effects. This shows Figures 6 and 8 combined, with the opacity effect added, and the minimum halo mass reduced to $M_{\rm min} = 10^{-6} M_\odot$.

### 5.2.5 Spectra for Single Branching Ratios

To see the variation in the annihilation intensity that is possible with different annihilation spectra, one can carry out the calculations for the same annihilation cross section and particle mass, but with different annihilation channels. These results could be used with Equation (3.5) to construct the intensity for combinations of these channels according to any velocity-independent branching ratios. If the branching ratios are velocity-dependent, they need to be included in the halo ensemble average for that model.

In Figure 10a, intensity spectra are shown for s-wave dark matter annihilation for particles with annihilation cross-section $[\sigma v]_0 = 1.9 \times 10^{-26}$ cm$^3$/s and mass 150 GeV, the same as for our focus point model. They were calculated for dark matter annihilating purely to $W^+W^-$ bosons, $b\bar{b}$ quarks, $c\bar{c}$ quarks, $\tau^+\tau^-$ leptons, $\mu^+\mu^-$ leptons, or $e^+e^-$ leptons. The gamma-ray spectrum per annihilation for this calculation was simulated with Pythia for each of the annihilation products. The intensity from annihilation to $W$'s is indistinguishable from annihilation to $b$ quarks for 150 GeV dark matter. The $c$ quarks have an additional high energy bump, but that would also be difficult to observe. Also, the light leptons, muons and electrons, produce nearly equivalent hard spectra that would be similarly difficult to distinguish from each other.

Each of the models has a strong feature in $\Delta_I$ near $E_\gamma = 5 \times 10^{-3} m_{\rm DM}$ from the gamma-ray opacity. This is even visible in the intensity spectra for the annihilations to leptons. These hard spectra also show a strong feature at $E_\gamma = m_{\rm DM}/(1 + z_{\rm max})$ where $z_{\rm max} = 10$ is the largest redshift integrated to in the calculation. In retrospect, this effect is slightly visible in $\Delta_I$ for the $B - L$ SUSY model, which produces a large number of light leptons. The redshift cutoff $z_{\rm max}$ is near the epoch of reionization because effects of reionization are not modeled. It was surprising to see possible contributions from photons at this distance. It is intriguing that neglecting photons produced from this era (and beyond) generates observable effects in our calculations. The possibility of being able to probe the physics of reionization with a hard annihilation signal is interesting.

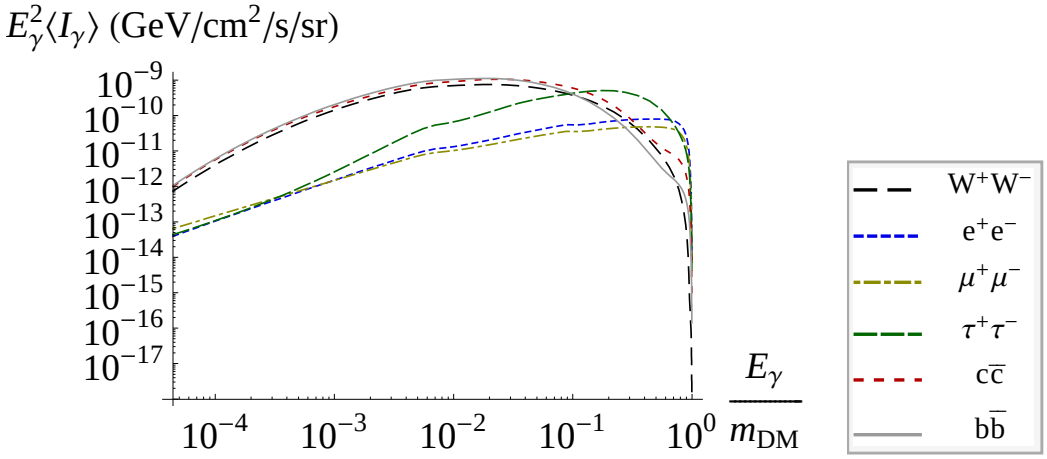


(a)

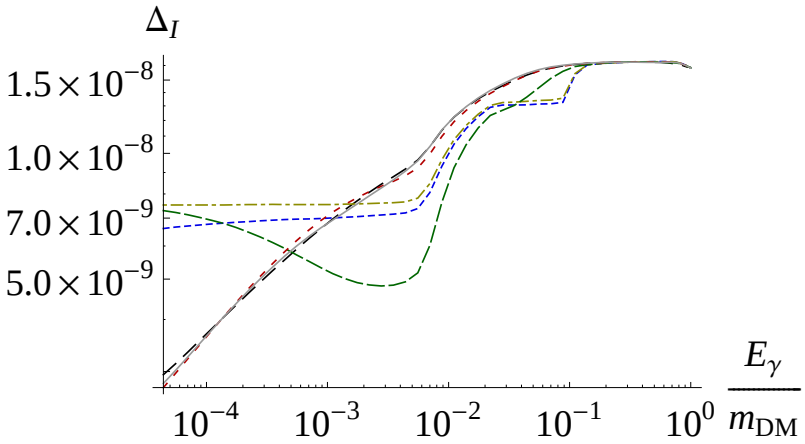


(b)

Figure 10: Intensity spectra for s-wave dark matter annihilation to single channels. (a) These show results for 150 GeV dark matter particles that annihilate with velocity-weighted cross section $[\sigma v]_0 = 1.9 \times 10^{-26}$ cm$^3$/s. (b) The p-wave effect on the spectral shape for each of the annihilation products.

### 5.2.6 Angular Power Spectrum with P-wave Annihilation

From Equation 4.22, the relative effect of p-wave annihilation on the angular power spectrum of the extragalactic gamma-ray radiation it produces is determined from $\Delta_I(E_\gamma)$, and the new coefficients $\overline{\Delta^{(1)}_{C_\ell}}(E_\gamma)$ and $\overline{\Delta^{(2)}_{C_\ell}}(E_\gamma)$.

These new coefficients are plotted—for the five SUSY models we've considered—in Figure 11, at the energy $E_{\gamma,\text{peak}}$ where $E_\gamma^2 \langle I_\gamma \rangle (E_\gamma)$ is maximized. The variations, from opacity effects and different annihilation spectra, are quite mild.

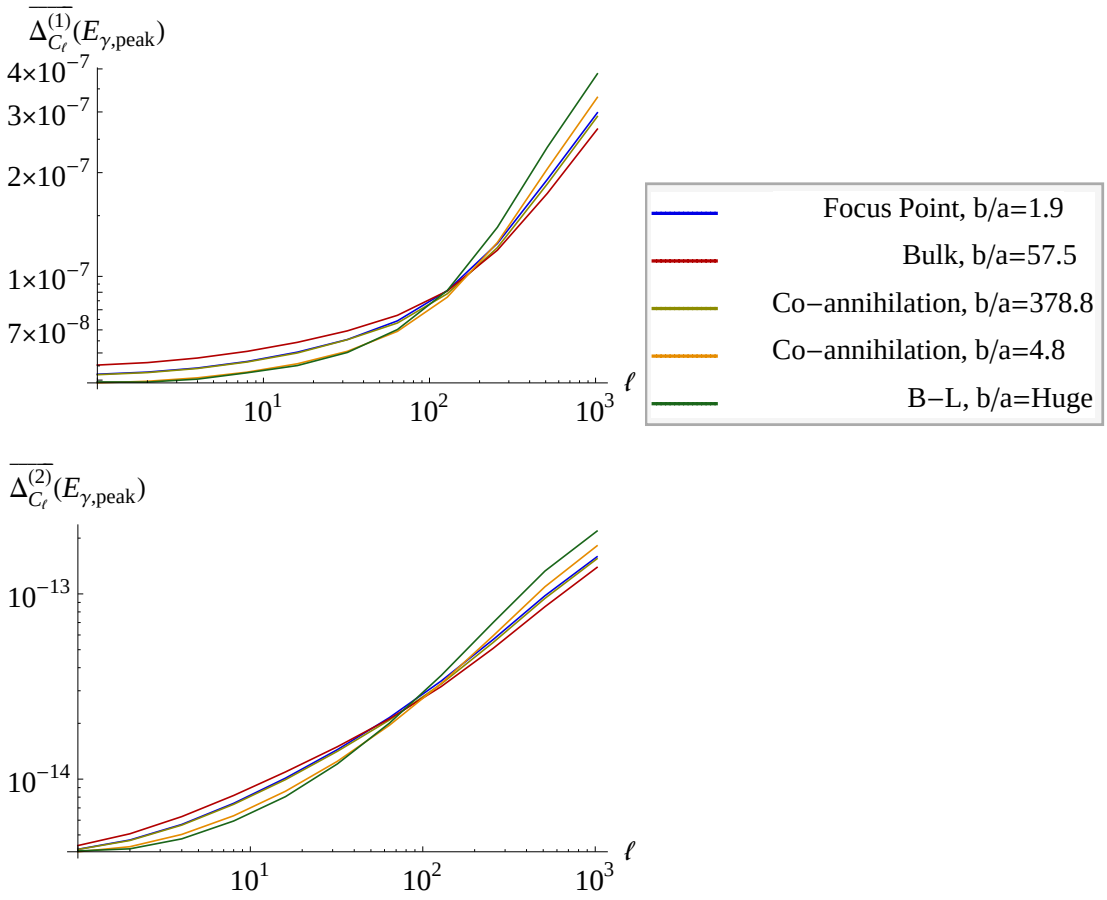


Figure 11: The coefficients that describe the relative effect of p-wave annihilation on the angular power spectrum, according to Eq. (4.22), for the five sample SUSY models under consideration.

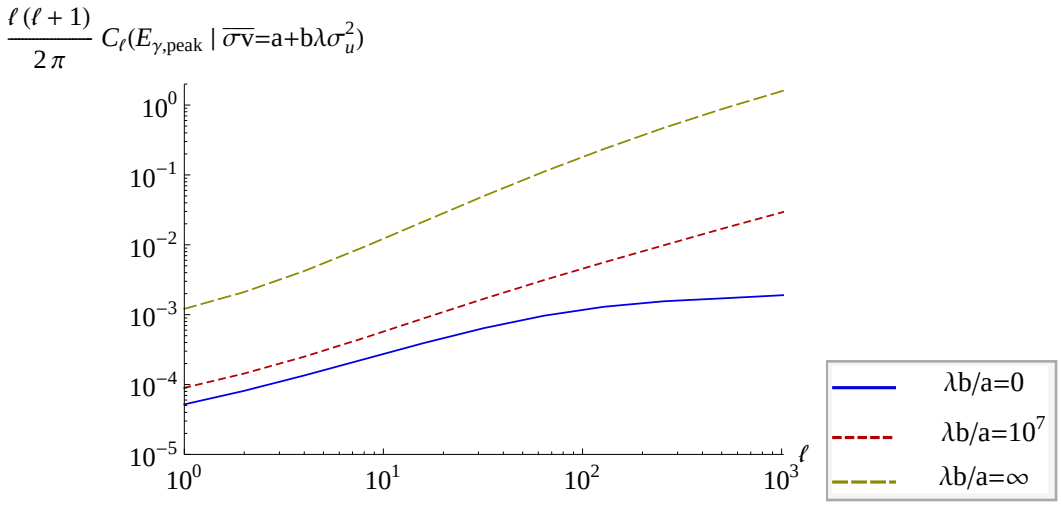


Figure 12: The angular power spectrum of extragalactic, diffuse gamma-rays from dark matter annihilation with different p-wave components.

With $\overline{\Delta^{(1)}_{C_\ell}}(E_\gamma) \sim 10^7$, it is only non-negligible to $C_\ell$ if $\lambda b/a \gtrsim 10^7$, or $b/a \gtrsim 10^6$. Similarly for $\overline{\Delta^{(2)}_{C_\ell}}(E_\gamma) \sim 10^{14}$. This is consistent with the results of the p-wave effects on the intensity spectrum.

It is interesting to take the general shapes of $\overline{\Delta^{(1)}_{C_\ell}}$ and $\overline{\Delta^{(2)}_{C_\ell}}$, and put them into Eq. (4.22) for various values of $\lambda b/a$, to see how the angular power spectrum can be affected by the coupling of dark matter annihilation to the particle velocity distribution. The results of this exercise are shown in Figure 12 for the focus point model. At $b = 0$, the usual s-wave angular power spectrum seen in previous works is reproduced [51, 52]. Note how a strong p-wave can significantly increase power, more so for large values of $\ell$. If a component of gamma-rays of extragalactic origin is determined to have an angular power spectrum that is best described by a dark matter annihilation with significant $v^2$ component in its cross section, it would be an interesting challenge to understand the mechanisms that allow such a signal to be observable, since one would expect its intensity to be strongly p-wave suppressed. The magnitude of the effects for the p-wave cross section provide motivation for considering other interesting scenarios of velocity-dependent annihilation, such as annihilation resonances at low dark matter particle velocities.

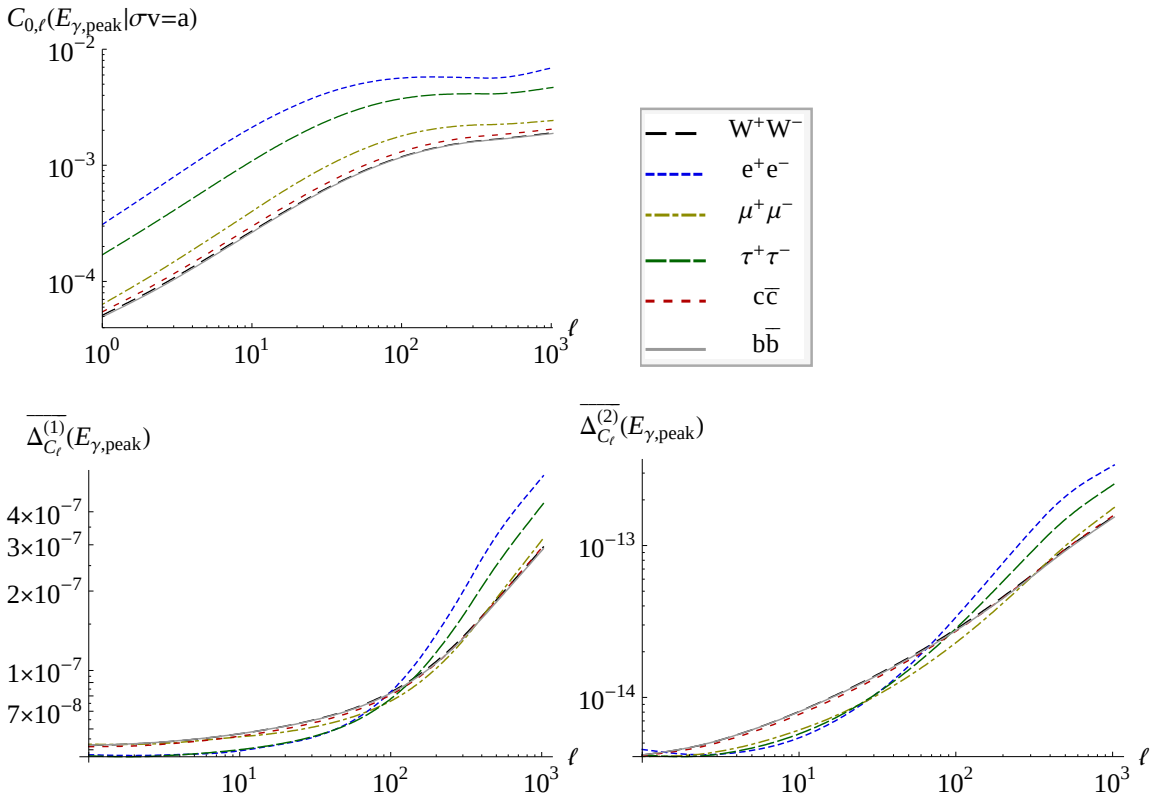


Figure 13: The components contributing to the p-wave angular power spectrum for different pure annihilation channels of a generic 150 GeV dark matter particle.

To see the variation in the angular power spectrum due to different annihilation products, the above calculations were carried out for the same annihilation cross section as the focus point model, but with different annihilation spectra. In Figure 13 are plotted the elements needed to determine the p-wave angular power spectrum (the s-wave angular power spectrum, and the $\overline{\Delta^{(1)}_{C_\ell}}$ and $\overline{\Delta^{(2)}_{C_\ell}}$ coefficients), along with the $\Delta_I$ coefficients in Figure 10b. The main result to note about the plots of the coefficients is that they depend only weakly on energy, and are very similar for different annihilation spectra into charged particles, particularly at the highest energies near the dark matter mass. In fact, the most variation is found in the pure s-wave angular power spectrum.

## 5.3 Mean Extragalactic Intensity for Sommerfeld-Enhanced Annihilation

Presented in this section are estimates of the effect of Sommerfeld enhancement of s-wave annihilation on the intensity spectrum of produced gamma-rays. Results will be shown for the four example cross sections that are displayed in Figure 4b, as expressed by Equation (3.10) with $[\sigma v]_0 = 3 \times 10^{-26}$ cm$^3$/s. For this initial calculation, the mean velocity-weighted cross section at each position in a halo is approximated using Equation (3.23) and $\lambda = 6$.

$$[\overline{\sigma v}]_h(r|M,z) \approx S\left(\left.\frac{\sqrt{\lambda}\sigma_{uh}(r|M,z)}{\alpha}\right|\epsilon_\phi\right)[\sigma v]_0 \tag{5.5}$$

Figure 14 shows the results for the extragalactic gamma-ray intensity due to annihilations for theories with these cross sections. Again for simplicity, we consider theories that annihilate exclusively into lepton anti-lepton pairs. The photon radiation spectra per annihilation for these processes were also simulated with Pythia. In these examples, the dark matter mass is taken to be $m_{\rm DM} = 200$ GeV. Higher masses were explored; they simply gave the same results, scaled up in energy. Annihilation into $\mu^+\mu^-$ is visually indistinguishable from the electron case, with a slightly higher intensity.

The ratio of each enhanced intensity to its respective unenhanced s-wave annihilation intensity $\langle I_\gamma \rangle_0$, where $S = 1$, is shown in Figure 15. Here it is found that, for $\alpha = 0.01$, the intensity enhancement is nearly uniform over most of the Sommerfeld parameter space. This follows from the fact that, as is seen in Figure 4b, the cross section has already saturated at the relative velocities important today, less than $10^{-3}$, unless one is extremely close to a resonance value of $\epsilon_\phi$. However, for smaller values of $\alpha$, the graph in Figure 4b shifts to the left and the cross section may not necessarily be completely saturated today for larger enhancements. This results in a smaller cross section at high energies and has the effect of widening the intensity peak and shifting the maximum to smaller energy. This is what is observed with the resonance cases: $\epsilon_\phi = 0$ (an example of a $v^{-1}$ resonance), and $\epsilon_\phi = \epsilon_\phi^{(n)}$ ($v^{-2}$ resonances).

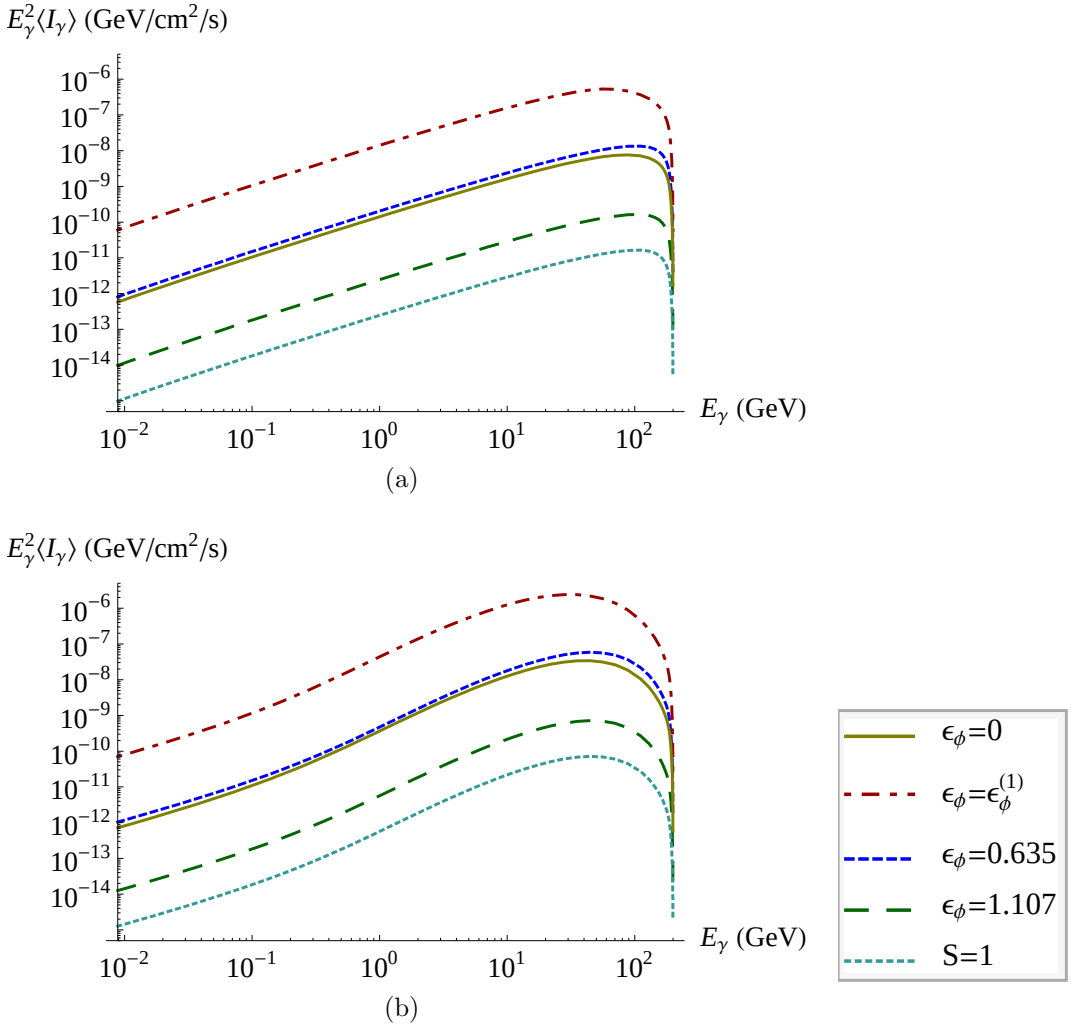


Figure 14: Extragalactic gamma-ray intensities from dark matter with a sample of annihilation theories including s-wave, Sommerfeld-enhanced s-wave, and Sommerfeld s-wave resonances. For these models, $\alpha = 0.01$ and $m_{\rm DM} = 200\,{\rm GeV}$. The bottom dotted curves show the intensity for no Sommerfeld enhancement, the solid lines show the Coulomb-Sommerfeld resonance, the top dot-dashed curves show the first Sommerfeld resonance, and the long (short) dashed curves show the Sommerfeld enhanced intensity where the enhancement saturates at 10 (1000). (a) Primary photon radiation from annihilation into electron-positron pairs. (b) Annihilation into $\tau^+\tau^-$.

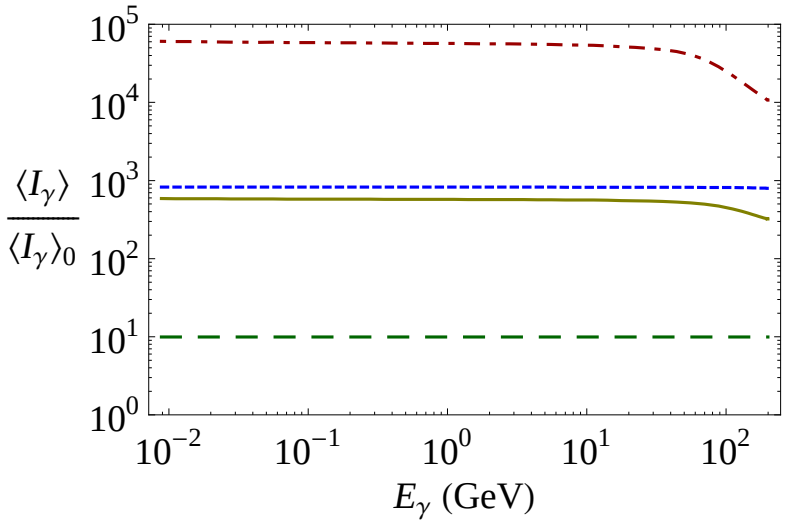


(a)

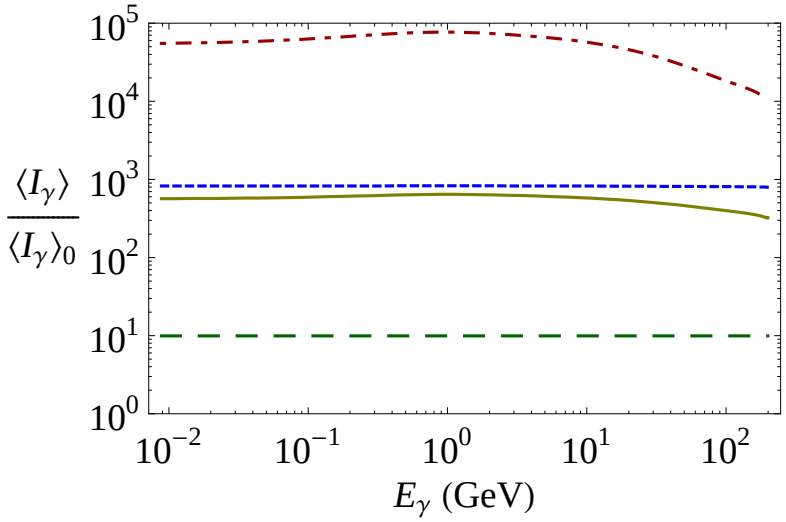


(b)

Figure 15: Ratios of the predicted Sommerfeld enhanced intensities to the unenhanced intensity. (a) Primary photon production from annihilation exclusively into electron-positron pairs. (b) Annihilation into $\tau^+\tau^-$.

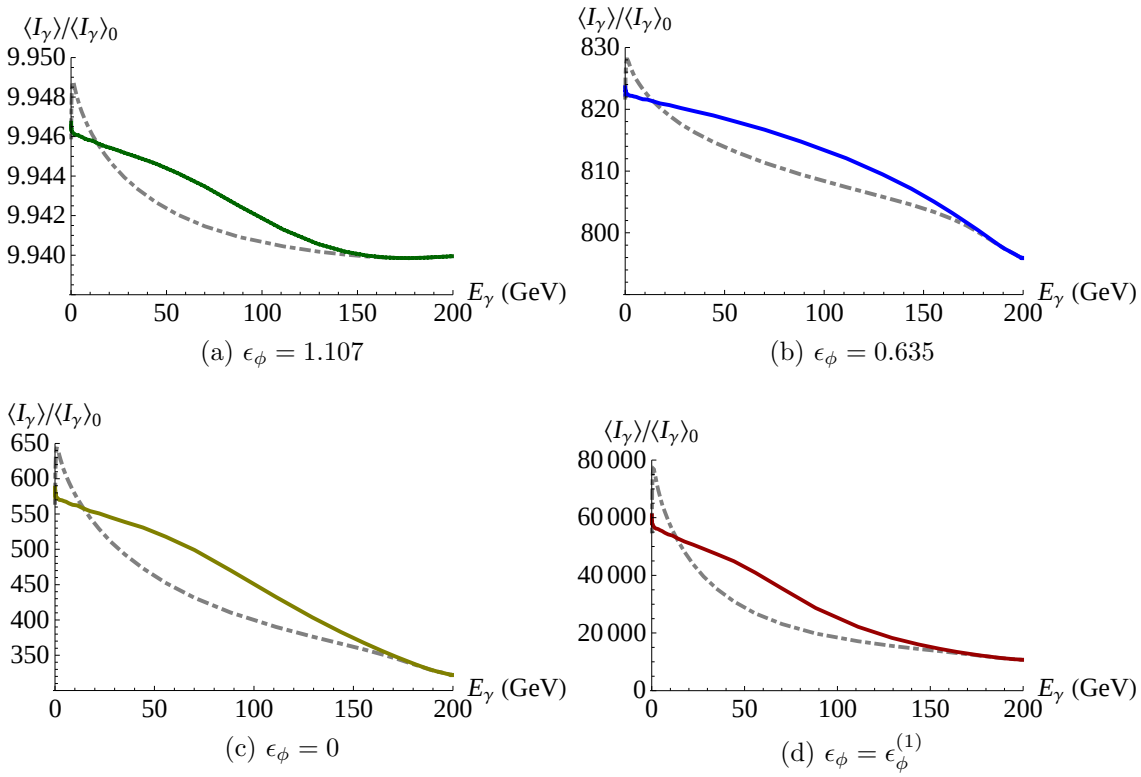


Figure 16: The intensity ratios in Figure 15. The solid curves are for annihilation into $e^+e^-$, and the dot-dashed curves show the results for $\tau$ pair production.

To see the detail of the variation of $\langle I_\gamma \rangle / \langle I_\gamma \rangle_0$ at peak intensities, plots of each ratio on a linear scale, focused only on the appropriate range of the ratio for each cross section, are shown in Figure 16. For comparison, the enhancement at saturation for $\epsilon_\phi = 1.107$ was 10.00, and for $\epsilon_\phi = 0.635$ it was 1004. The intensity ratio for annihilation into taus in the saturated examples was very similar to the electron-production results. However, it can be seen that differences in the spectrum per annihilation become important at the resonances.

# 6 COMPARISON OF GALACTIC AND EXTRAGALACTIC GAMMA-RAY ANNIHILATION SIGNALS TO NEUTRINO ANNIHILATION SIGNALS*

With the tools developed to do the calculations presented in Section 5, it is possible to do many different analyses involving extragalactic dark matter annihilation signals. The calculation of the intensity of gamma-rays from dark matter annihilations in our dark matter halo is a relatively simple when compared to the extragalactic calculation. An important question is whether it can be determined conclusively which source of annihilation radiation dominates. If both components contribute significantly, then the net intensity is of interest.

It is worth calculating the neutrino flux from extragalactic and galactic dark matter annihilations because neutrinos are also produced in the annihilations of dark matter in the particle models described in this document.

By the date of this research, the WMAP7 results were released [12], and the updated cosmological parameters were applied to the calculations in this section: $\Omega_\Lambda = 0.725$, $\Omega_b = 0.0458$, $h = 0.702$, $\sigma_8 = 0.816$, and $n_s = 0.968$. Again, neutrino streaming effects are neglected in the linear power spectrum, and $\Omega_c = 1 - \Omega_\Lambda - \Omega_b$ is set.

## 6.1 Diffuse Intensity Due To Galactic Dark Matter Annihilation

If our own Milky Way Galaxy dark matter halo is taken to be a typical halo of our large scale structure model at mass $M_{\rm G} = 2 \times 10^{12} M_\odot$, then it has scale radius $r_{s,{\rm G}} = 38.0$ kpc, virial radius $R_{\rm vir,G} = 412$ kpc, and concentration $c_{\rm G} = 10.8$. The important parameter here for this calculation is the scale radius, since the contribution to the annihilation signal due to dark matter outside this radius is very small; therefore, the virial radius definition (and hence the value of

*Parts of this section are reprinted with permission from "*Extragalactic and Galactic Gamma Rays and Neutrinos From Annihilating Dark Matter*" by R. Allahverdi, S. Campbell, and B. Dutta, Phys. Rev. D **85**, 035004 (2012), Copyright 2012 by The American Physical Society.

concentration) does not significantly affect the prediction of the galactic annihilation signal. The solar system's position in the halo is estimated to be $R_\odot = 8.0$ kpc from the galactic center.

For the work in this section, it is assumed that velocity-dependence of the dark matter annihilation is negligible (ie. s-wave dominated annihilation). The intensity of gamma-rays, due to dark matter annihilation in the galactic halo in the direction of angle $\psi$ from the galactic center (assumed coincident with the halo center), is typically written as

$$I_{\gamma,\mathrm{G}}(E_\gamma, \psi) = \frac{\sigma v}{8\pi m_{\mathrm{DM}}^2} \frac{\mathrm{d}N_\gamma}{\mathrm{d}E_\gamma}(E_\gamma) J(\psi), \tag{6.1}$$

where the $J$-factor is the line of sight integration of the square dark matter density from the solar system out the halo[†]

$$J(\psi) \equiv \int_0^{r_{\max}(\psi)} \mathrm{d}r \left[ \rho_h \left( \sqrt{r^2 - 2rR_\odot \cos\psi + R_\odot^2} \middle| M_{\mathrm{G}}, 0 \right) \right]^2, \tag{6.2}$$

with

$$r_{\max}(\psi) = R_\odot \cos\psi + \sqrt{R_{\mathrm{vir,G}}^2 - R_\odot^2 \sin^2\psi}. \tag{6.3}$$

## 6.2 Comparison of Galactic and Extragalactic Gamma-ray Annihilation Signals

In this subsection, the galactic annihilation gamma-ray signal is compared to the extragalactic intensity for the halo model of dark matter distribution.

In Figure 17 are the contributions of the galactic and extragalactic components of annihilation to the gamma-ray intensity for different lines of sight in the halo. The particle physics model used in this example is the focus point model describe in Table 2.

[†] The $J$-factor is usually scaled to be in units of $R_\odot \rho_\odot^2$, where $\rho_\odot$ is the estimated local density. This is less convenient for comparison with the extragalactic signal, and therefore, the $J$-factor is given an unscaled definition here, with arbitrary units of square mass density times length.

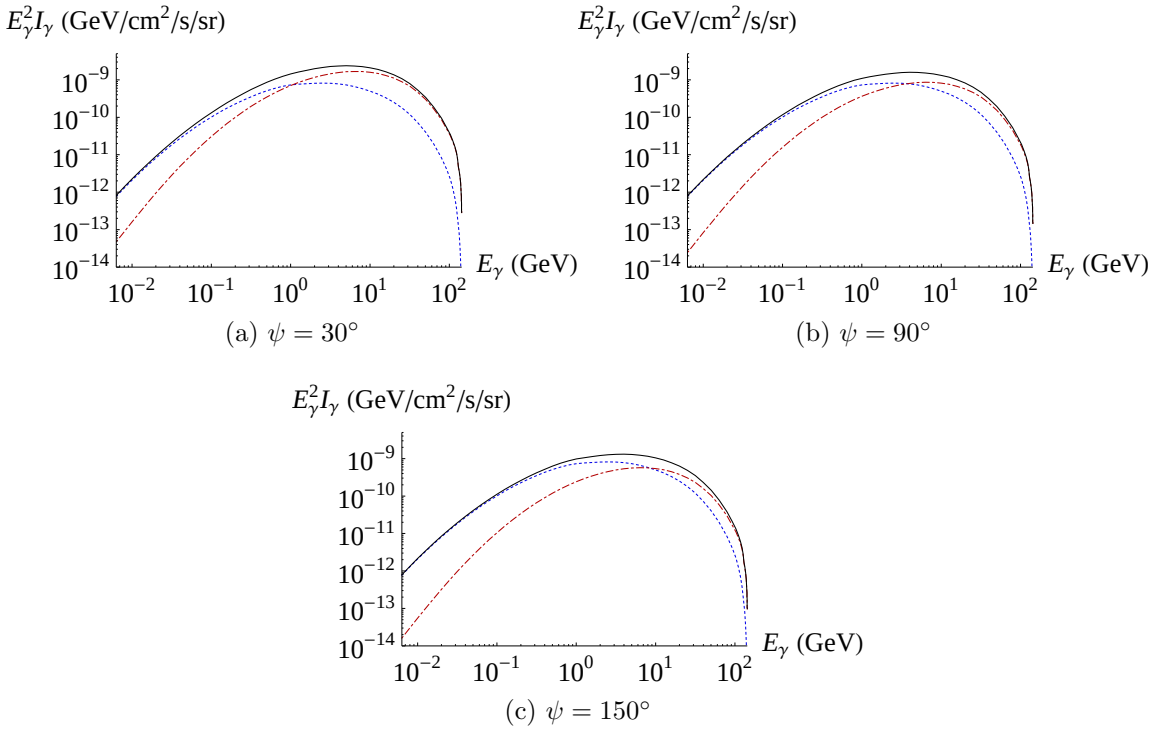


Figure 17: The gamma ray signal from annihilating dark matter in the directions of the indicated angle $\psi$ from the galactic center. The dark matter shown here is a 150 GeV neutralino in the focus point region of mSUGRA with $\tan\beta = 10$. The dotted blue line is the extragalactic component, the dot-dashed red line is the galactic component. The solid line is the net signal.

In the dark matter density distribution models, the galactic component is dominant at the intensity peak of the signal when looking toward the galactic center, but the contributions of the components are comparable when looking out of the galactic plane or away from the galactic center. It is conceivable that with slightly different choices of distribution parameters, the relative importance of each might be altered considerably. The relative strength of the galactic to extragalactic intensity at a given photon energy is

$$\frac{I_{\gamma,\mathrm{EG}}(E_\gamma)}{I_{\gamma,\mathrm{G}}(E_\gamma,\psi)} = \int \mathrm{d}z \left[\frac{\langle\rho^2\rangle(z)}{H(z)(1+z)^3\hat{J}(\psi)}\right] \left[\frac{\frac{\mathrm{d}N_\gamma}{\mathrm{d}E_\gamma}((1+z)E_\gamma)}{\frac{\mathrm{d}N_\gamma}{\mathrm{d}E_\gamma}(E_\gamma)}\right] e^{-\tau((1+z)E_\gamma,z)}.$$

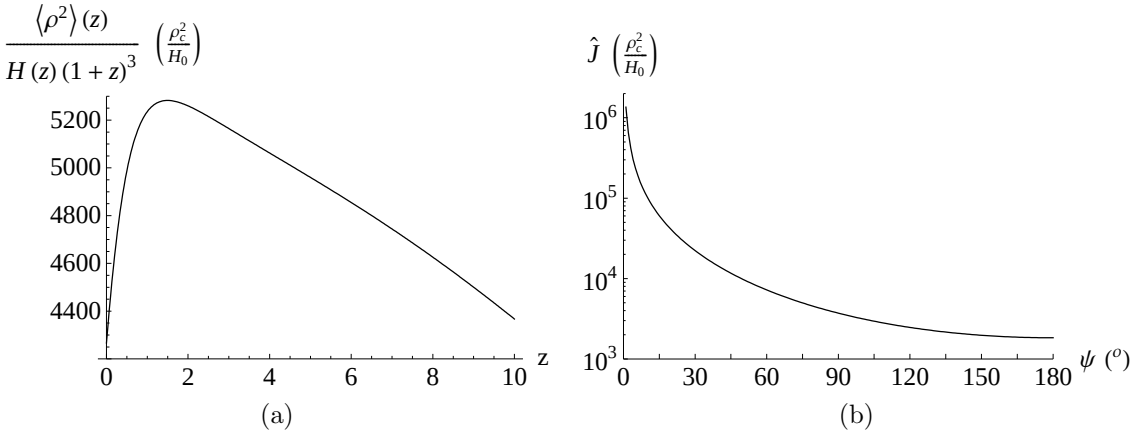


Figure 18: Contributions to the galactic and extragalactic annihilation intensities. (a) The magnitude of extragalactic intensity is approximately proportional to the area under this curve, around $48000\rho_c^2/H_0$. (b) The corresponding contribution to the galactic intensity.

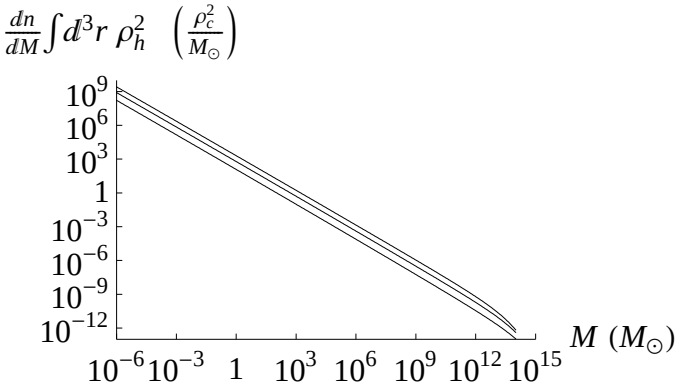


Figure 19: The mass integrand of the mean square density. It is shown for halos at redshift $z = 0$, 0.5, and 1 from bottom to top, respectively.

The important parameters then appear in the first factor of the integrand. Figure 18 plots the extragalactic and galactic contributions to this factor in units of $\rho_c^2/H_0$, where $\rho_c$ is the cosmological critical density to collapse and $H_0$ is the Hubble constant. The extragalactic part is relatively flat in scale, with an area under the curve of around $48000\rho_c^2/H_0$. The convolution with the annihilation spectrum and opacity could modify the importance of this factor, depending on the

details of those functions. One may wonder what mass scale of halos most contributes to the mean square density $\langle \rho^2 \rangle$. In Figure 19, it is apparent that the mass integrand scales essentially like $M^{-1}$, nearly all the way to the maximum mass scale, suggesting that all mass scales practically contribute equally to the intensity. If the mass dependence of the Sheth-Tormen mass function correctly describes the halo distribution down to low scales, and those low-mass halos have density profiles well described by NFW, with concentrations described by the model specified, then all mass scales are important contributors to annihilations.

However, consider for the moment the effect of the neglected substructure. At Milky Way size halos, it is expected that substructure will increase the annihilation rate by a factor on the order of 100, depending on the minimum halo mass scale [102]. By definition, the smallest halos will not have any subhalos, and larger halos will have more and more substructure. Thus, one would expect the largest halos to contribute the most to intensity purely based on their substructure.

For the galactic contribution, if the galactic halo is well described by an NFW (or similar) profile, then the value of scale radius $r_s$ has a significant effect on how concentrated the dark matter is to the galactic core. Based on observations of stellar velocities, it is generally estimated that the galactic halo has a somewhat smaller scale radius than the typical radius we used [137]. This would result in an increase in the predicted galactic intensity.

The scaling of the density at the core is also important. On the right plot of Figure 18, it can be seen how the intensity formally diverges as the line of sight approaches the galactic center for the NFW profile. Observing a signal from toward the galactic center would help to better understand how the density is distributed there in our halo, and would allow us to test various ideas about the effects that the central black hole and baryonic cooling have on the profile.

It is expected that the substructure observed in the simulations would increase the galactic signal by a factor of a few—not as significantly as for the extragalactic intensity [102]. Therefore, it is not unreasonable to suppose that the extragalactic

annihilation could dominate over the galactic signal for most lines-of-sight that are not too close to the galactic center.

In summary, an estimation of the most crucial elements in these calculations, which have the greatest effects on the result, is:

- the halo scale radius, the galactic value of which has an important effect on the galactic signal component, and the halo distribution of which affects the extragalactic signal; and
- the inclusion of subhalos, not yet taken into account, will also increase the predicted signal, and will depend on the scale of minimum halo mass.

Thus, it can be concluded from this discussion that the galactic and extragalactic annihilation signals in Figure 17 are of comparable intensity, due to the value of $r_{s,G}$ that was used, and the lack of substructure effects.

While being mindful of these uncertainties, it is still interesting to compare these calculations to the experimental measurements. The extragalactic signal for this model peaks at $E_\gamma^2 I_\gamma \approx 10^{-9}$ GeV/cm$^2$/s/sr while the extracted extragalactic $\gamma$-rays reported by the Fermi Gamma-ray Space Telescope is
$E_\gamma^2 I_\gamma \approx 5 \times 10^{-7}$ GeV/cm$^2$/s/sr at that energy [138]. At higher dark matter particle masses $m_{\rm DM}$ with the same annihilation operators, the $\gamma$-ray peak energy increases proportional to $m_{\rm DM}$, but the intensity $I$ decreases like $m_{\rm DM}^{-3}$, according to Equation 3.8. However, the extragalactic background intensity is measured to drop more slowly, consistent with a power law scaling $E_\gamma^{-2.41}$.

Unless the annihilation at the galactic core is very bright, it will be difficult to observe those dark matter annihilation gamma-rays originating from the core because there are so many other bright sources of astrophysical gamma-rays in that region, which have theoretical uncertainties associated with them. A less contaminated signal, for example, would be the consideration of the mean annihilation signal away from the core. The galactic and extragalactic components

for this are shown in Figure 20 for the same focus point model. For comparison, also shown are the total signals for dark matter of the same mass, that annihilates to $W^+W^-$, $b\bar{b}$, or $\tau^+\tau^-$, at the same annihilation cross section as the focus point model. The sources of photons in those models are from decaying pions or radiating charged fermions. The W and b spectra are dispersed to lower energies because they are more likely to decay to hadronic showers where each photon-emitting product is at lower energy. At 150 GeV dark matter annihilation, the photons from annihilation to $W^+W^-$ are indistinguishable from annihilation to $b\bar{b}$. These pure branching ratio intensities can be used to construct the intensity profile for any theory that annihilates to these states, with known branching ratios. For larger dark matter masses, the $W$ and $b$ signals become distinguishable from one another to a greater extent.

## 6.3 Galactic and Extragalactic Neutrino Signals

The models discussed in the previous sections also contribute a neutrino annihilation spectrum $\frac{\mathrm{d}N_\nu}{\mathrm{d}E_\nu}$, therefore, it is interesting to consider this component of the signal as well. Since the neutrino is electrically neutral and weakly interacting, it also propagates relatively freely through the cosmos, and the annihilation signal will have both galactic and extragalactic contributions. This calculation is completely analogous to that for the gamma-ray signal. Cosmic opacity for the neutrinos is neglected in the sample calculations that follow.

Figure 21 shows the galactic, extragalactic, and net intensity of cosmic neutrinos from annihilations of the same 150 GeV focus point neutralino dark matter considered in the previous section. In the galactic signal, one can clearly see the peaks from primarily and secondarily produced neutrinos from the W decays. However, those features are washed out in the redshift-modulated extragalactic signal. Both galactic and extragalactic components contribute significantly to the total signal in all of the shown lines of sight. Again, reasonable adjustments of dark matter distribution parameters and consideration of halo substructures could significantly alter this balance in either direction.

Although the prediction of the annihilation neutrino signal from the galactic center still contains uncertainties from the galactic core density profile, it does not suffer from the same astrophysical contamination as do gamma-rays. Therefore, there is no reason to exclude the galactic center in these experiments. In fact, if a neutrino detector with high angular resolution can be developed, it is a good strategy to focus on the galactic center.

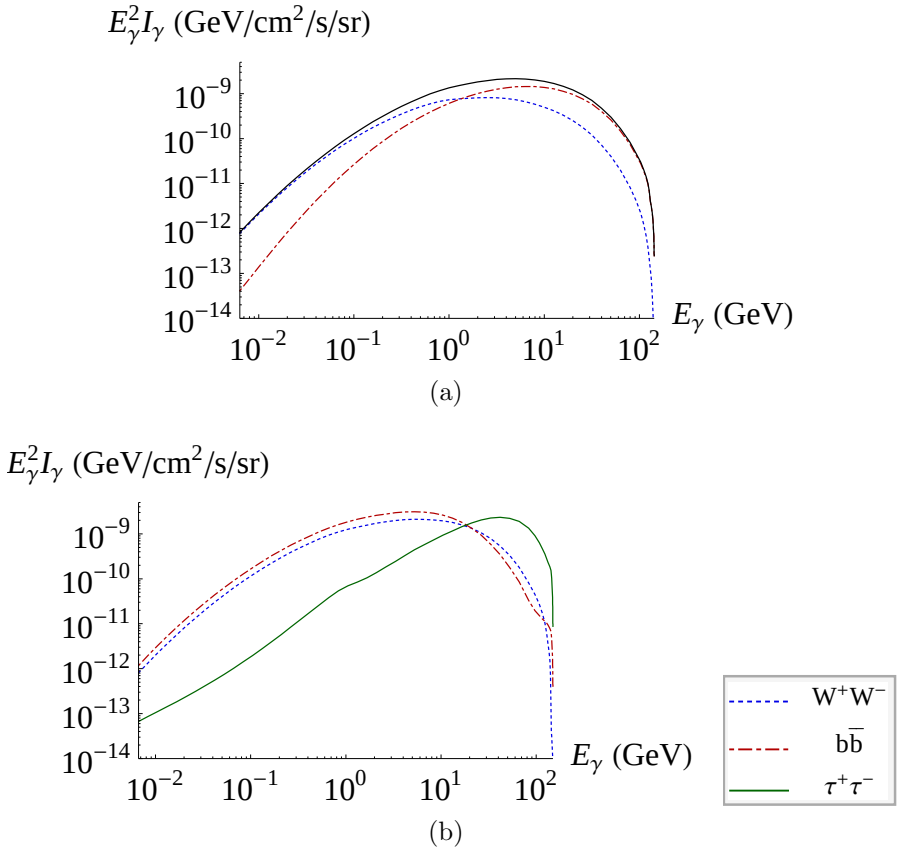


Figure 20: The mean intensity of gamma-rays from annihilating dark matter, averaged over all directions an angle $\psi > 18^\circ$ away from the galactic center. (a) Shown for the focus point model. The plot format is the same as for Figure 17. (b) Shown for a 150 GeV dark matter particle that annihilates purely to $W^+W^-$, $b\bar{b}$, or $\tau^+\tau^-$.

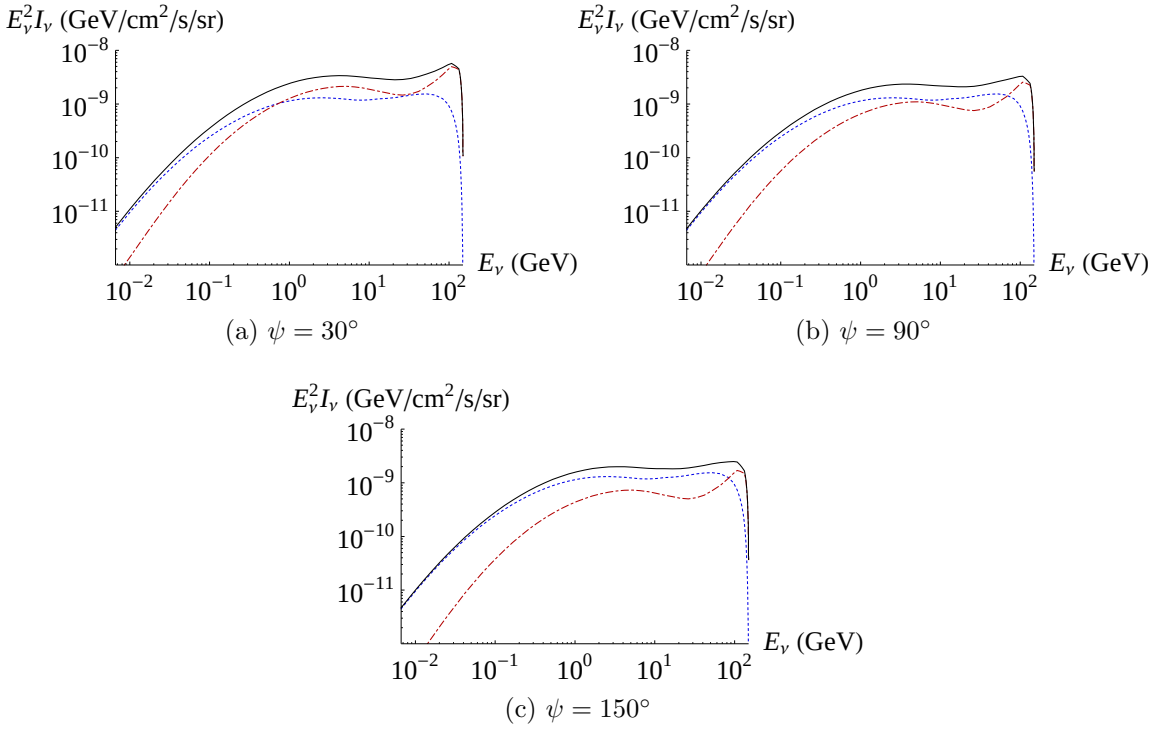


Figure 21: The neutrino signal from annihilating dark matter in the indicated angle $\psi$ from the galactic center. The same particle model and plot format as in Figure 17 is used.

Figure 22 shows the neutrino signal for the focus point model averaged over the whole sky, directions away from the core, and directions focused on the core, respectively. The galactic annihilations are seen to dominate the signal at the galactic core in the model of particle distribution where the NFW profile holds to the center, and halo substructures are neglected. The same dominance of the galactic core occurs with annihilation gamma-rays, but it is very difficult to see those photons from the noisy center of the galaxy. Further work, with more realistic distributions, should better elucidate the situation at the galactic core, and provide an understanding of the information about the dark matter distribution uncertainties that may be available in an observed neutrino signal.

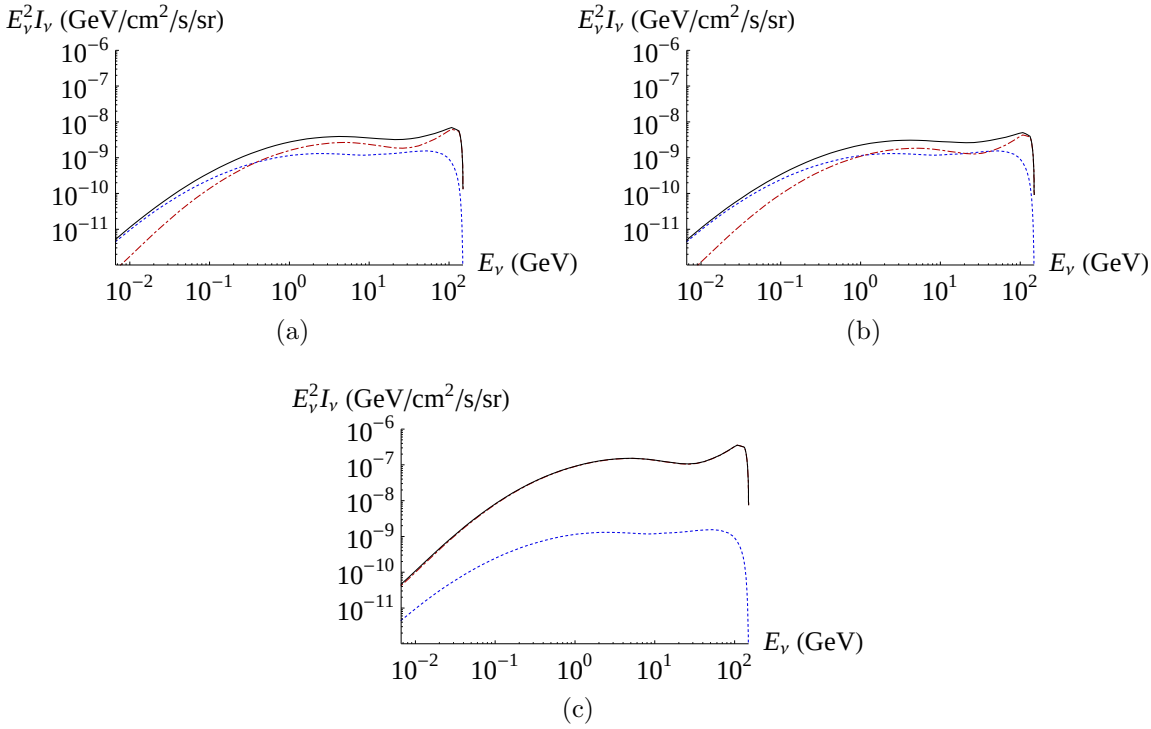


Figure 22: The mean neutrino intensity for the focus point model. (a) The all-sky intensity, $0° < \psi < 180°$. (b) The anticore intensity, $\psi > 18°$. (c) The core intensity, $\psi < 5°$. The plot format is the same as in Figure 17.

It is common in the literature to express neutrino signals as binned detector event rates per detector mass. If $\langle I_\nu \rangle_\Omega$ is the mean annihilation intensity in a solid angle $\Omega$ of observation, the event rate for a neutrino $\nu_f$ of flavor $f = e$, $\mu$, or $\tau$ in an energy bin $E_i < E_\nu < E_{i+1}$ is

$$R_{\nu_f,i} = \frac{N_A \Omega}{n_m} \int_{E_i}^{E_{i+1}} \mathrm{d}E_\nu \, \sigma_{\nu_f N}(E_\nu) \, \langle I_\nu \rangle_\Omega(E_\nu)$$

where $N_A$ is Avogadro's number, $n_m$ is the molar mass of the detector material, and $\sigma_{\nu_f N}$ is the neutrino-nucleon charged current scattering cross section [139]. Note that $N_A/n_m$ is simply the nucleon number per detector mass. To ease conversion of the results for different detector materials, the results are shown for $n_m = 1$ g/mol.

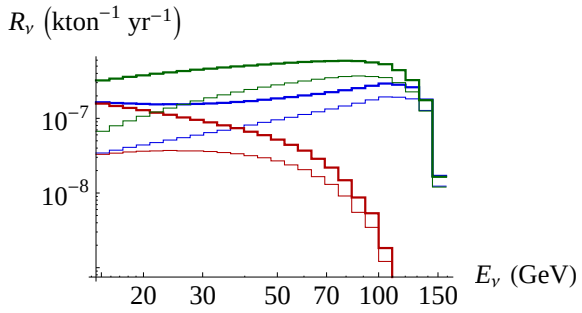


Figure 23: All-sky neutrino plus antineutrino detection rates for 150 GeV dark matter annihilation. The thick lines are for electron or muon flavor, and the thin lines show the tau flavor rate. At 70 Gev, the top two green lines are for annihilation to $\tau^+\tau^-$ leptons, the middle two blue lines show annihilation to $W^+W^-$ bosons, and the bottom two red lines are for annihilation to $b\bar{b}$ quarks.

Figure 23 shows the neutrino event rates for annihilation into $W$ bosons, $b$ quarks, or $\tau$ leptons. The logarithmic GeV energy bin size used is $\Delta = \log_{10}\left(\frac{E_{i+1}}{E_i}\right) = 0.04$. At these neutrino energies, the electron and muon neutrinos have indistinguishable nucleon scattering cross sections, which are larger than that for the tau neutrinos. Hence, the tau neutrino event rates are a little smaller. Since $\tau$ leptons always decay to a primary neutrino, while $W$ bosons only decay directly to leptons some of the time, the $\nu$ production from $\tau$'s is more intense. The $b$ quarks do not produce primary neutrinos, and only have a lower energy neutrino spectrum from secondary chains. Thus, the flux of neutrinos from annihilations breaks the degeneracy between annihilation into $W^+W^-$ and $b\bar{b}$ that occured in the gamma-ray signal.

Another class of models that results in interesting phenomenology for dark-matter-annihilation neutrinos is the $U(1)_{B-L}$ extension of the MSSM, described in Sec. 5.1.2. The particular model considered here is a parameter space where the sneutrino $\tilde{N}$ is the dark matter particle, and has a mass of 150 GeV. In this case, the dominant annihilation channels are the s-wave processes $\tilde{N}\tilde{N} \longrightarrow N^c N^c$ and $\tilde{N}^*\tilde{N}^* \longrightarrow N^{c*}N^{c*}$ via t-channel exchange of $B-L$ neutralinos through its coupling with the gaugino $\tilde{Z}'$. The $N^c$, taken to have mass 135 GeV, then decay exclusively to $\nu$ and standard model Higgs $h$, considered here to have mass $m_h = 120$ GeV. At this mass, the Higgs boson decays mostly to

$WW^*$ bosons, and to $b\bar{b}$ quarks, each of which produce secondary photons and neutrinos. The neutrino detector rates for this model are shown in Figure 24. The $\tilde{N}$ annihilation in this model does have a slight p-wave component, and the s-wave cross section is $\sigma v = 1.1 \times 10^{-26}$ cm$^3$/s, giving the correct thermal dark matter relic density. The particle mass spectra, annihilation cross sections, and relic density calculations were carried out using a program written by Bhaskar Dutta. The neutrinos spectrum per annihilation was calculated using Pythia.

The secondary neutrinos produced from the Higgs decay result in a broad, soft spectrum, whereas the neutrinos produced directly from $N^c$ decays produce a narrower peak at lower energies on the order of the mass difference between the $N^c$ and the Higgs. Due to the Higgs decays, there is also a gamma-ray component to the signal.

In the case where the $\tilde{N}$ dark matter is heavier (larger than twice the Higgs mass), and the $N^c$ mass is still slightly smaller than the $\tilde{N}$ particle, then the physical neutrino peak occurs closer to the dark matter mass energy. This will produce a hard spectrum with narrow peak from the primary neutrinos, and a broad low-energy tail produced by the Higgs decays.

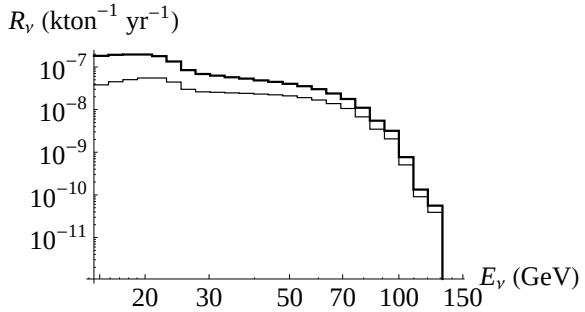


Figure 24: All-sky neutrino plus antineutrino event rates for 150 GeV sneutrino dark matter that annihilates to two 135 GeV right-handed neutrinos (each flavor equally represented), each of which decays to a light neutrino and 120 GeV standard model Higgs particle.

Another intriguing scenario occurs when the dark matter annihilates solely to two light neutrinos $\nu$. In the context of the $B - L$ model previously described, this corresponds to the limit where the Higgs mass is small—negligible compared to the $\tilde{N}$ mass—and the mass difference between $\tilde{N}$ and $N^c$ is also very small. Then the spectrum of the produced light neutrinos is at the energy of the $\tilde{N}$, and the width of the spectrum is very small. This simple scenario results in a prominent neutrino line feature with no corresponding gamma-ray observations. At this energy scale of neutrino energies, the dominant astrophysical source is atmospheric neutrinos.

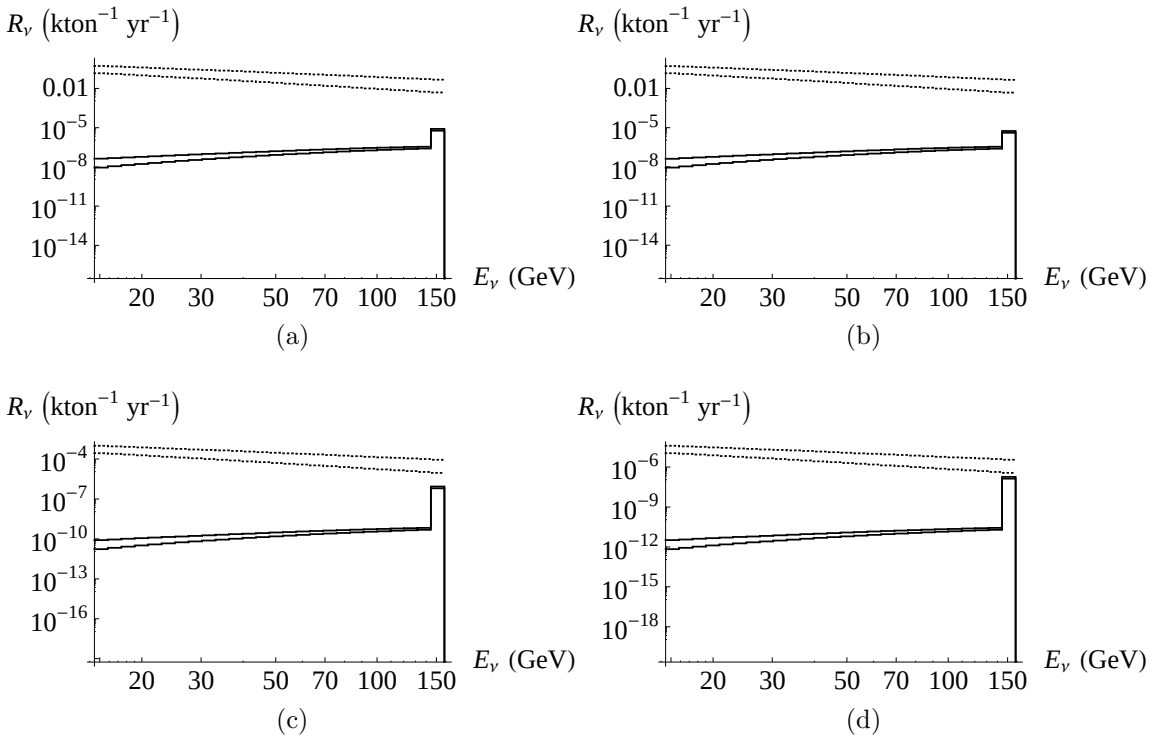


Figure 25: Neutrino plus antineutrino event rates for 150 GeV dark matter annihilating to 2 prompt neutrinos $\nu$. The annihilation is taken to occur with cross section $\sigma v = 1.1 \times 10^{-26}$ cm$^3$/s (solid lines), shown with the mean atmospheric neutrino plus antineutrino rates at the Kamioka site during low solar activity (dotted lines). For the atmospheric neutrinos, the upper line is the muon flavor, and the lower line is the electron flavor. For the annihilation neutrinos, the upper line shows the rate for electron flavor, as well as the rate for muon flavor. The lower line shows the rates for $\nu_\tau + \overline{\nu}_\tau$. (a) The mean neutrino rates from the whole sky. (b) Rates when excluding the galactic core, $\psi > 18°$. (c) Rates when focused on the galactic core, $\psi < 5°$. (d) Rates when focused on the inner galactic core, $\psi < 1°$.

The solid lines in Figure 25 show the detector rates for annihilation of 150 GeV dark matter particles into prompt neutrinos, to each flavor equally, with a cross section of $\sigma v = 1.1 \times 10^{-26}$ cm$^3$/s with the modeled dark matter distribution. The upper line shows the electron flavor rates and muon flavor rates. The lower line is the tau flavor detection rate. Shown is the mean all-sky signal ($0° < \psi < 180°$), an anticore signal ($\psi > 18°$), a core signal ($\psi < 5°$), and an inner core signal ($\psi < 1°$). The width of the spectral line feature is due to the velocity distribution of dark matter in the galactic halo, which is negligible compared to the energy resolution of viable detectors. Therefore, it is completely contained in the energy bin at the dark matter mass. The diffuse component is due to the redshifted extragalactic neutrinos. The dotted lines in the figure are the predicted mean atmospheric neutrino rates, as would be seen at the Kamioka site during minimum solar activity [140]. The upper line shows the $\nu_\mu + \overline{\nu}_\mu$ rates, and the lower line shows the $\nu_e + \overline{\nu}_e$ rates.

By comparing them with the previous neutrino rate plots, it is seen that the typical diffuse signals are well below the current measured atmospheric neutrino rates. Again, the situation likely improves with the consideration of halo substructure, and the background can also be reduced with respect to the signal by focusing on a nearby dark-matter-dense region of space, as shall be discussed for the prompt neutrino production example.

The prominence of the peak at the galactic core shows how a neutrino detector with high angular resolution might extract a spectral line feature by focusing on a dense region of space. Although the signal to background ratio improves with small solid angles of observation, the detection rates become forbiddingly small. With better energy resolution, an experiment can also gain a stronger signal in the spectral line scenario. Thinner energy bins have a higher spectral line height.

For the energy bin at the energy of the dark matter mass $E_\nu = m$, the width that is required for the bin height to be at the corresponding atmospheric neutrino rate

when observing in solid angle $\Omega$ is approximately

$$\Delta E(m, \Omega) \approx \frac{1}{\Omega} \frac{\phi_G(m, \Omega)}{I_{\rm atm}(m) - I_{\rm EG}(m)},$$

where $\phi_G(m, \Omega)$ is the flux of galactic annihilation neutrinos of energy at the dark matter particle mass $m$ originating within the solid angle $\Omega$, $I_{\rm atm}(m)$ is the mean intensity of atmospheric neutrinos of energy $m$, and $I_{\rm EG}(m)$ is the mean extragalactic annihilation neutrino intensity. The corresponding required logarithmic bin width is (assuming $\Delta E \ll m$)

$$\Delta \approx \frac{\Delta E}{m \ln 10}.$$

This approximate logarithmic energy bin size is shown in Figure 26 for ranges of the dark matter mass, and for different solid angles centered on the galactic center.

For comparison, Figure 25 used $\Delta = 0.04$. The energy scales that require the smallest bin widths occur where the spectral line is most hindered by the atmospheric neutrinos. At high dark matter mass, the electron neutrinos are a great deal easier to see, since the electron atmospheric neutrinos are much less abundant than the muon atmospheric neutrinos.

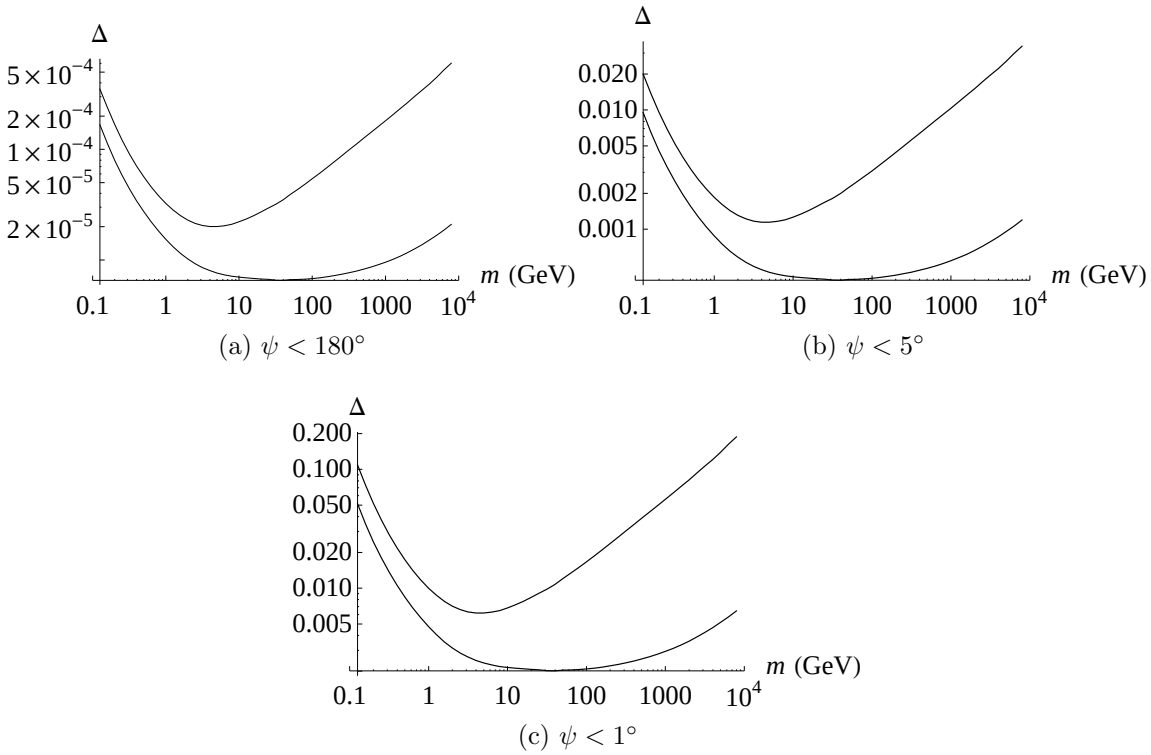


(a) $\psi < 180°$ (b) $\psi < 5°$

(c) $\psi < 1°$

Figure 26: The approximate logarithmic bin size required for the spectral line detector rate bin to reach the atmospheric neutrino rate. The upper line is for $\nu_e + \overline{\nu}_e$ and the lower line is for $\nu_\mu + \overline{\nu}_\mu$.

# 7 CONCLUSIONS

For this dissertation, a calculational tool was developed and implemented to analyze predictions of extragalactic gamma-ray or neutrino signals from annihilating dark matter, predominantly from the cores of halos. The formalism of these signals was extended from previous works, in order to be able to account for effects due to the relative motions of the annihilating particles.

To accomplish this, a new theory of universal halo velocity variance profiles $\sigma^2_{uh}(r)$ was developed, based on the observed approximate power-law stratification of the pseudo-phase-space-density profile within N-body computer simulations of dark matter halos. A velocity variance profile for the NFW density profile was proposed to be

$$\sigma^2_{uh}(r) = \sigma^2_s \left(\frac{r}{r_s}\right)^{\beta} \left(1 + \frac{r}{r_s}\right)^{-4/3}$$

with scale variance related to the scale density $\rho_s$ and scale radius $r_s$ by

$$\sigma^2_s = 12^{2/3} \pi G \kappa^{-1} (\beta - 1/3)^{\beta - 1/3} (1 - \beta)^{1-\beta} \rho_s r_s^2,$$

and critical values $\beta = 17/27$ and $\kappa = 100/81$. The mean velocity variance evolution of the Universe was presented for the NFW profile of Sheth-Tormen-distributed halos, illustrating the increase in particle relative motions due to structure growth, and eventual washing out of phase space from dark energy domination. Results of the annihilation calculations were consistent with significant dark matter populations having relative velocity $v < \sim 10^{-3}$ in the model.

Other new universal halo profiles necessarily introduced are the mean square relative particle velocity profile, denoted $v^2_h(r)$, and the mean relative-velocity-weighted annihilation cross section profile for dark matter $[\overline{\sigma v}]_h(r)$. Velocity-dependence of the annihilation cross section can occur at the energies of cosmic dark matter for theories with p-wave annihilation, Sommerfeld-enhanced annihilation, or for annihilation through a Breit-Wigner resonance. Sample cross section halo profiles were considered for annihilation with a p-wave component in

halos with locally isotropic velocity distributions, and for Sommerfeld-enhanced annihilation in halos with local relative velocity density distributions approximated as a Dirac delta function.

A new formalism was derived for calculating the mean intensity spectrum and angular power spectrum of gamma-rays or neutrinos from extragalactic annihilating dark matter in smooth halos. This formalism is justified if the most dark-matter-dense regions of space occur at the nearly-spherical cores of halos. However, simulations predict that halos also contain significant populations of dense subhalos. If true, they will have a significant impact on the predicted annihilation signals and need to be accounted for. The formalism for smooth halos that is presented here can be extended to halos with substructure using existing methods for modifying the density distribution, since the pseudo-phase-space power law profile holds very well, even in the presence of substructure, and therefore the proposed method for determining the velocity variance distribution within the halo is still expected to be accurate with substructure. The gamma-ray intensity from annihilations at a region of space scales with $\rho^2\overline{\sigma v}$ at that position, where $\rho$ is the density and $\overline{\sigma v}$ is the mean velocity-weighted annihilation cross section.

An analysis of the effects of p-wave annihilation, where the velocity-weighted annihilation cross section is $\sigma v = a + bv^2$, on the annihilation signal of extragalactic gamma-rays was carried out. When the local velocity distribution at each point in the halo is isotropic, then $[\overline{\sigma v}]_h(r) = a + 6b\sigma^2_{uh}(r)$. The mean intensities of different supersymmetric models considered had variations due to different s-wave annihilation components $a$, p-wave strengths $b/a$, gamma-ray spectra per annihilation, and particle masses. Since the models considered produced thermal dark matter relics, the s-wave annihilation cross section $a$ is p-wave suppressed. This generates an associated suppression of the extragalactic gamma-ray intensity, and expressions that accurately approximate the amount of p-wave intensity suppression were presented. The coupling of the p-wave to the large-scale velocity distribution modifies the intensity by a factor of $1 + (6b/a)\Delta_I(E_\gamma)$, where the coefficient $\Delta_I$ depends predominantly on the model of cosmic dark matter phase space, but also has some dependence on the gamma-ray spectrum per annihilation.

This coefficient was presented for a variety of annihilation spectra. The order of magnitude of $\Delta_I$ is $10^{-8}$, and therefore, it is only significant to the signal if $b/a \gtrsim 10^6$. Also, since $\Delta_I$ increases with $E_\gamma$, significant p-wave strengths harden the annihilation intensity spectrum. It is found that the p-wave suppression effect can be significant in the minimal supersymmetric standard model (MSSM), where p-wave strengths as high as $10^4$ were discovered. In the extension of the MSSM with a gauged baryon number minus lepton number symmetry, p-wave dominated theories with $b/a \gg 10^6$ were found to exist.

The p-wave was also shown to increase the angular power spectrum of the extragalactic annihilation gamma-rays by a factor of

$$1 + \frac{\frac{6b}{a}\overline{\Delta^{(1)}_{C_\ell}}(E_\gamma) + \left(\frac{6b}{a}\right)^2 \overline{\Delta^{(2)}_{C_\ell}}(E_\gamma)}{\left[1 + \left(\frac{6b}{a}\right)\Delta_I(E_\gamma)\right]^2}.$$

Again, the coefficients $\overline{\Delta^{(1)}_{C_\ell}}$ and $\overline{\Delta^{(2)}_{C_\ell}}$ were presented for various annihilation products. As before, none of the coefficients contributes significantly to the factor unless $b/a \gtrsim 10^6$, at which point all of the coefficients contribute. However, in the case where $b/a$ is so large that the theory is p-wave dominated, the contribution from $\overline{\Delta^{(1)}_{C_\ell}}$ becomes negligible. However, in thermally-produced models of dark matter, a large p-wave would suppress the intensity so as to make it unobservable. Therefore, the observation of an angular power spectrum from annihilations that is best interpreted as being produced by a dark matter theory with strong p-wave annihilation would necessarily have to be a non-thermally produced relic.

In order to calculate the angular power spectrum and its p-wave coefficients, the Fourier transform of $\rho_h^2(r)\sigma_{uh}^2(r)$ needs to be evaluated for any halo mass and halo redshift. Development of an efficient algorithm to evaluate this function for NFW profiles was carried out and is presented in Appendix A.

An initial exploration of extragalactic signals produced by a Sommerfeld-enhanced theory of dark matter with $\sigma v = [\sigma v]_0 S(v^2)$ was carried out by approximating $[\overline{\sigma v}]_h(r) \approx [\sigma v]_0 S(6\sigma_{uh}^2(r))$. Deviations from a constant boost were quantified in detail, and seen to be relatively small. The case of Sommerfeld resonances were

observed to soften somewhat the intensity spectrum.

When considering annihilation to bottom anti-bottom quarks, or to $W^+W^-$ bosons for 150 GeV dark matter, it was found that they result in indistinguishable gamma-ray spectra. However, when considering their neutrino spectra, the models are very different, since W's can decay to prompt neutrinos, whereas the quarks cannot.

When comparing the extragalactic signals to annihilation signals produced from the galactic dark matter halo, it was found that the magnitude of peak $E_\gamma^2 I$ is nearly the same for both theories when observed out from the galactic plane, but the intensities are offset with the extragalactic signal's being redshifted to lower energies. This suggests that both components may contribute significantly to the cosmic signal. However, with uncertainties of the contribution of substructure to the extragalactic signal, and the value of parameters such as the concentration of our own halo, the problem as to which component contributes most to a cosmic indirect detection signal deserves further study. Since GeV energy neutrinos have few known backgrounds near the galactic center, and the center is expected to be a dense volume of dark matter, searching for neutrinos from the center of the galaxy may be an interesting source to detect annihilation radiation producing neutrinos.

# REFERENCES


[1] M. Mateo, in *Proceedings of an ESO/OHP Workshop on Dwarf Galaxies*, edited by G. Meylan and P. Prugniel, ESO Conference and Workshop Proceedings (European Southern Observatory, Garching, 1994), Vol. 49, p. 309; M. Mateo, in *The Nature of Elliptical Galaxies; 2nd Stromlo Symposium*, edited by M. Arnaboldi, G. S. Da Costa, and P. Saha, ASP Conference Series (Astronomical Society of the Pacific, San Francisco, 1997), Vol. 116, p. 259; M. Mateo, Ann. Rev. Astron. Astrophys. **36**, 435 (1998); M. G. Walker, M. Mateo, E. W. Olszewski, O. Y. Gnedin, X. Wang *et al.*, Astrophys. J. **667**, L53 (2007); J. Peñarrubia, A. McConnachie, and J. F. Navarro, *ibid.* **672**, 904 (2008); M. G. Walker, M. Mateo, E. W. Olszewski, J. Peñarrubia, N. W. Evans *et al.*, *ibid.* **704**, 1274 (2009); **710**, 886 (2010); N. C. Amorisco and N. W. Evans, Mon. Not. R. Astron. Soc. **411**, 2118 (2011).

[2] J. H. Oort, Astrophys. J. **91**, 273 (1940); M. S. Roberts, *ibid.* **144**, 639 (1966); V. C. Rubin and W. K. J. Ford, *ibid.* **159**, 379 (1970); M. S. Roberts and A. H. Rots, Astron. Astrophys., **26**, 483 (1973); M. Persic, P. Salucci, and F. Stel, Mon. Not. R. Astron. Soc. **281**, 27 (1996); **283**, 1102 (1996); P. Salucci, A. Lapi, C. Tonini, G. Gentile, I. Yegorova *et al.*, *ibid.* **378**, 41 (2007); I. A. Yegorova, A. Pizzella, and P. Salucci, Astron. Astrophys., **532**, A105 (2011).

[3] O. Gerhard, A. Kronawitter, R. P. Saglia, and R. Bender, Astron. J. **121**, 1936 (2001); A. Dekel, F. Stoehr, G. A. Mamon, T. J. Cox, G. S. Novak *et al.*, Nature (London) **437**, 707 (2005); M. Cappellari, R. Bacon, M. Bureau, M. C. Damen, R. L. Davies *et al.*, Mon. Not. R. Astron. Soc. **366**, 1126 (2006).

[4] F. Zwicky, Helvetica Phys. Acta **6**, 110 (1933); S. Smith, Astrophys. J. **83**, 23 (1936); F. Zwicky, *ibid.* **86**, 217 (1937); F. Zwicky, Phys. Rev. **51**, 290 (1937); J. Einasto, A. Kaasik, and E. Saar, Nature (London) **250**, 309 (1974); R. G. Carlberg, H. K. C. Yee, E. Ellingson, S. L. Morris, R. Abraham *et al.*, Astrophys. J. **485**, L13 (1997); J. P. Ostriker, *ibid.* **525C**, 297 (1999).

[5] D. Rusin, C. S. Kochanek, and C. R. Keeton, Astrophys. J. **595**, 29 (2003); L. V. E. Koopmans, A. Bolton, T. Treu, O. Czoske, M. W. Auger *et al.*, *ibid.* **703**, L51 (2009); M. Barnabè, O. Czoske, L. V. E. Koopmans, T. Treu, and A. S. Bolton, Mon. Not. R. Astron. Soc. **415**, 2215 (2011).

[6] J.-P. Kneib, P. Hudelot, R. S. Ellis, T. Treu, G. P. Smith *et al.*, Astrophys. J. **598**, 804 (2003).

[7] M. Markevitch, A. H. Gonzalez, L. David, A. Vikhlinin, S. Murray *et al.*, Astrophys. J. **567**, L27 (2002); D. Clowe, A. Gonzalez, and M. Markevitch,

*ibid.* **604**, 596 (2004); M. Markevitch, A. H. Gonzalez, D. Clowe, A. Vikhlinin, L. David *et al.*, *ibid.* **606**, 819 (2004); D. Clowe, M. Bradač, A. H. Gonzalez, M. Markevitch, S. W. Randall *et al.*, *ibid.* **648**, L109 (2006).

[8] R. Massey, J. Rhodes, R. Ellis, N. Scoville, A. Leauthaud *et al.*, Nature (London) **445**, 286 (2007).

[9] C. S. Frenk, S. D. M. White, and M. Davis, Astrophys. J. **271**, 417 (1983); S. D. M. White, C. S. Frenk, M. Davis, and G. Efstathiou, *ibid.* **313**, 505 (1987).

[10] N. Vittorio and J. Silk, Astrophys. J. Lett. **285**, 39 (1984);

[11] E. Komatsu, J. Dunkley, M. R. Nolta, C. L. Bennett, B. Gold *et al.*(WMAP Collaboration), Astrophys. J. Suppl. Ser. **180**, 330 (2009).

[12] E. Komatsu, K. M. Smith, J. Dunkley, C. L. Bennett, B. Gold *et al.*(WMAP Collaboration), Astrophys. J. Suppl. Ser. **192**, 18 (2011).

[13] W. J. Percival, S. Cole, D. J. Eisenstein, R. C. Nichol, J. A. Peacock *et al.*, Mon. Not. R. Astron. Soc. **381**, 1053 (2007); W. J. Percival, B. A. Reid, D. J. Eisenstein, N. A. Bahcall, T. Budavari *et al.*, *ibid.* **401**, 2148 (2010).

[14] A. G. Riess, A. V. Filippenko, P. Challis, A. Clocchiatti, A. Diercks *et al.*, Astron. J. **116**, 1009 (1998); S. Perlmutter, G. Aldering, G. Goldhaber, R. A. Knop, P. Nugent *et al.*, Astrophys. J. **517**, 565 (1999).

[15] A. Coc, E. Vangioni-Flam, P. Descouvemont, A. Adahchour, and C. Angulo, Astrophys. J. **600**, 544 (2004); AIP Conf. Proc. **704**, 341 (2004); A. Coc and E. Vangioni, J. Phys. Conf. Ser. **202**, 012001 (2010); A. Coc, S. Goriely, Y. Xu, M. Saimpert, and E. Vangioni, Astrophys. J. **744**, 158 (2012).

[16] B. D. Fields, Annu. Rev. Nucl. Part. Sci. **61**, 47 (2011).

[17] H. Pagels and J. R. Primack, Phys. Rev. Lett. **48**, 223 (1982); P. J. E. Peebles, Astrophys. J. Lett. **263**, L1 (1982); G. R. Blumenthal, S. M. Faber, J. R. Primack, and M. J. Rees, Nature (London) **311**, 517 (1984); M. Davis, G. Efstathiou, C. S. Frenk, and S. D. M. White, Astrophys. J. **292**, 371 (1985).

[18] P. McDonald, J. Miralda-Escudé, M. Rauch, W. L. W. Sargent, T. A. Barlow *et al.*, Astrophys. J. **562**, 52 (2001); **598**, 712 (2003).

[19] J. N. Bahcall and C. L. Sarazin, Astrophys. J. **213**, L99 (1977); W. G. Mathews, *ibid.* **219**, 413 (1978); E. Rasia, S. Ettori, L. Moscardini, P. Mazzotta, S. Borgani *et al.*, Mon. Not. R. Astron. Soc. **369**, 2013 (2006).

[20] P. Tisserand, L. Le Guillou, C. Afonso, J. N. Albert, J. Andersen *et al.*, Astron. Astrophys. **469**, 387 (2007).

[21] K. N. Abazajian, E. Calabrese, A. Cooray, F. de Bernardis, S. Dodelson *et al.*, Astropart. Phys. **35**, 177 (2011).

[22] J. R. Bond, J. Centrella, A. S. Szalay, and J. R. Wilson, Mon. Not. R. Astron. Soc. **210**, 515 (1984).

[23] E. Aprile, K. Arisaka, F. Arneodo, A. Askin, L. Baudis *et al.*(XENON100 Collaboration), Phys. Rev. Lett. **107**, 131302 (2011).

[24] Z. Ahmed, D. S. Akerib, S. Arrenberg, C. N. Bailey, D. Balakishiyeva *et al.*(CDMS-II Collaboration), Science **327**, 1619 (2010); Phys. Rev. Lett. **106**, 131302 (2011).

[25] G. Angloher, M. Bauer, I. Bavykina, A. Bento, C. Bucci *et al.*, arXiv:1109.0702.

[26] R. Bernabei, P. Belli, F. Cappella, R. Cerulli, C. J. Dai *et al.*(DAMA Collaboration), Eur. Phys. J. C **56**, 333 (2008); **67**, 39 (2010); R. Bernabei, P. Belli, A. di Marco, F. Montecchia, F. Cappella *et al.*, AIP Conf. Proc. **1417**, 12 (2011).

[27] C. E. Aalseth, P. S. Barbeau, J. Colaresi, J. I. Collar, J. Diaz Leon *et al.*(CoGeNT Collaboration), Phys. Rev. Lett. **107**, 141301 (2011).

[28] P. Belli, R. Bernabei, A. Bottino, F. Cappella, R. Cerulli *et al.*, Phys. Rev. D **84**, 055014 (2011).

[29] G. Gelmini and P. Gondolo, Phys. Rev. D **64**, 023504 (2001).

[30] W. B. Atwood, A. A. Abdo, M. Ackermann, W. Althouse, B. Anderson *et al.*(Fermi-LAT Collaboration), Astrophys. J. **697**, 1071 (2009); A. A. Abdo, M. Ackermann, M. Ajello, L. Baldini, J. Ballet *et al.*(Fermi-LAT Collaboration), J. Cosmol. Astropart. Phys. 04 (2010) 014.

[31] A. Abramowski, F. Acero, F. Aharonian, A. G. Akhperjanian, G. Anton *et al.*(HESS Collaboration), Astropart. Phys. **34**, 608 (2011); Phys. Rev. Lett. **106**, 161301 (2011); Astrophys. J. **735**, 12 (2011); **750**, 123 (2012).

[32] F. Krennrich, M. Bautista, M. Beilicke, W. Benbow, D. Boltuch *et al.*, Nucl. Instrum. Meth. A **630**, 16 (2011).

[33] R. Abbasi, Y. Abdou, T. Abu-Zayyad, M. Ackermann, J. Adams *et al.*(IceCube Collaboration), arXiv:1111.2738.

[34] M. Ackermann, J. Ahrens, X. Bai, M. Bartelt, S. W. Barwick *et al.*(AMANDA Collaboration), Astropart. Phys. **24**, 459 (2006).

[35] G. Lim, arXiv:0905.2316; J. Zornoza, Nucl. Instrum. Meth. A, In Press.

[36] R. Battiston, Nucl. Instrum. Meth. A **588**, 227 (2008).

[37] O. Adriani, G. C. Barbarino, G. A. Bazilevskaya, R. Bellotti, M. Boezio *et al.*(PAMELA Collaboration), Nature (London) **458**, 607 (2009).

[38] J. Chang, J. H. Adams, H. S. Ahn, G. L. Bashindzhagyan, M. Christi *et al.*, Nature (London) **456**, 362 (2008).

[39] A. A. Abdo, M. Ackermann, M. Ajello, W. B. Atwood, M. Axelsson *et al.*(Fermi-LAT Collaboration), Phys. Rev. Lett. **102**, 181101 (2009); M. Ackermann, M. Ajello, W. B. Atwood, L. Baldini, J. Ballet *et al.*(Fermi-LAT Collaboration), Phys. Rev. D **82**, 092004 (2010); M. Ackermann, M. Ajello, A. Allafort, L. Baldini, G. Barbiellini *et al.*(Fermi-LAT Collaboration), Phys. Rev. Lett **108**, 011103 (2012).

[40] R. Abbasi, Y. Abdou, T. Abu-Zayyad, M. Ackermann, J. Adams *et al.*(IceCube Collaboration), Phys. Rev. D **85**, 042002 (2012).

[41] M. Ackermann, M. Ajello, A. Albert, W. B. Atwood, L. Baldini *et al.*(Fermi-LAT Collaboration), Phys. Rev. Lett. **107**, 241302 (2011).

[42] S.-H. Lee, T. Kamae, L. Baldini, F. Giordano, M.-H. Grondin *et al.*, Astropart. Phys. **35**, 211 (2011).

[43] S. H. Margolis, D. N. Schramm, and R. Silberberg, Astrophys. J. **221**, 990 (1978).

[44] C. Cálcáneo-Roldan and B. Moore, Phys. Rev. D **62**, 123005 (2000).

[45] J. M. Siegal-Gaskins, J. Cosmol. Astropart. Phys. 10 (2008) 040.

[46] A. A. Klypin, A. V. Kravtsov, O. Valenzuela, and F. Prada, Astrophys. J. **522**, 82 (1999); B. Moore, S. Ghigna, F. Governato, G. Lake, T. R. Quinn *et al.*, *ibid.* **524**, L19 (1999); L. E. Strigari, J. S. Bullock, M. Kaplinghat, J. Diemand, M. Kuhlen *et al.*, *ibid.* **669**, 676 (2007); M. Kuhlen, J. Diemand, P. Madau, and M. Zemp, J. Phys. Conf. Ser. **125**, 012008 (2008).

[47] K. Heitmann, Z. Lukić, P. Fasel, S. Habib, M. S. Warren *et al.*, Comput. Sci. Disc. **1**, 015003 (2008).

[48] S. Trujillo-Gomez, A. Klypin, J. Primack, and A. J. Romanowsky, Astrophys. J. **742**, 16 (2011).

[49] J. F. Navarro, C. S. Frenk, and S. D. M. White, Astrophys. J. **490**, 493 (1997).

[50] J. F. Navarro, A. Ludlow, V. Springel, J. Wang, M. Vogelsberger *et al.*, Mon. Not. R. Astron. Soc. **402**, 21 (2010).

[51] S. Ando and E. Komatsu, Phys. Rev. D **73**, 023521 (2006).

[52] D. Elsässer and K. Mannheim, Astropart. Phys. **22**, 65 (2004); A. Cuoco, J. Brandbyge, S. Hannestad, T. Haugboelle, and G. Miele, Phys. Rev. D **77**, 123518 (2008).

[53] A. Cooray and R. K. Sheth, Phys. Rept. **372**, 1 (2002).

[54] J. Zavala, V. Springel, and M. Boylan-Kolchin, in *2009 Fermi Symposium*, eConf Proceedings C09-11-02.2, arXiv:1001.3307.

[55] M. Zemp, J. Diemand, M. Kuhlen, P. Madau, B. Moore *et al.*, Mon. Not. R. Astron. Soc. **394**, 641 (2009).

[56] V. Springel, J. Wang, M. Vogelsberger, A. Ludlow, A. Jenkins *et al.*, Mon. Not. R. Astron. Soc. **391**, 1685 (2008).

[57] A. Friedmann, Z. Phys. **10**, 377 (1922); G. Lemaître, Ann. Soc. Sci. Bruxelles **A47**, 49 (1927); Mon. Not. R. Astron. Soc. **91**, 483 (1931); **91**, 490 (1931); H. P. Robertson, Rev. Mod. Phys. **5**, 62 (1933); Astrophys. J. **82**, 284 (1935); **83**, 187 (1936); **83**, 257 (1936); A. G. Walker, Proc. London Math. Soc. **42**, 90 (1937).

[58] S. Weinberg, *Gravitation and Cosmology: Principles and Applications of the General Theory of Relativity* (John Wiley and Sons, Inc., New York, NY, 1972); M. Trodden and S. M. Carroll, arXiv:astro-ph/0401547.

[59] E. W. Kolb and M. S. Turner, *The Early Universe* (Addison-Wesley, Reading, MA 1990).

[60] P. J. E. Peebles, *The Large-Scale Structure of the Universe* (Princeton University Press, Princeton, NJ, 1980).

[61] D. J. Heath, Mon. Not. R. Astron. Soc. **179**, 351 (1977).

[62] G. B. Arfken and H. J. Weber, *Mathematical Methods for Physicists* (Academic Press, Waitham, MA, 1995), 4th ed.

[63] S. M. Carroll, W. H. Press, and E. L. Turner, Annu. Rev. Astron. Astrophys. **30**, 499 (1992).

[64] A. A. Klypin, S. Trujillo-Gomez, and J. Primack, Astrophys. J. **740**, 102 (2011).

[65] V. R. Eke, S. Cole, and C. S. Frenk, Mon. Not. R. Astron. Soc. **282**, 263 (1996).

[66] A. Gabrielli, F. Labini, M. Joyce, and L. Pietronero, *Statistical Physics for Cosmic Structures* (Springer-Verlag, Berlin, Germany, 2005).

[67] D. J. Eisenstein and W. Hu, Astrophys. J. **511**, 5 (1999).

[68] J. E. Gunn and J. R. Gott, III, Astrophys. J. **176**, 1 (1972).

[69] A. R. Liddle and D. H. Lyth, *Cosmological Inflation and Large-Scale Structure* (Cambridge University Press, Cambridge, UK, 2000).

[70] G. D. Birkhoff, *Relativity and Modern Physics* (Harvard University Press, Cambridge, MA, 1923).

[71] P. J. E. Peebles, Astrophys. J. **284**, 439 (1984).

[72] O. Lahav, P. B. Lilje, J. R. Primack and M. J. Rees, Mon. Not. R. Astron. Soc. **251**, 128 (1991).

[73] A. L. Fetter and J. D. Walecka, *Theoretical Mechanics for Particles and Continua* (McGraw-Hill, New York, NY, 1980).

[74] S. Cole and C. Lacey, Mon. Not. R. Astron. Soc. **281**, 716 (1996).

[75] A. R. Zentner, Int. J. Mod. Phys. **16**, 763 (2007).

[76] W. H. Press and P. Schechter, Astrophys. J. **187**, 425 (1974).

[77] J. R. Bond, S. Cole, G. Efstathiou, and N. Kaiser, Astrophys. J. **379**, 440 (1991).

[78] R. K. Sheth and G. Tormen, Mon. Not. R. Astron. Soc. **308**, 119 (1999).

[79] R. K. Sheth and G. Tormen, Mon. Not. R. Astron. Soc. **329**, 61 (2002).

[80] G. L. Bryan and M. L. Norman, Astrophys. J. **495**, 80 (1998).

[81] H. J. Mo and S. D. M. White, Mon. Not. R. Astron. Soc. **282**, 347 (1996).

[82] R. K. Sheth, H. J. Mo, and G. Tormen, Mon. Not. R. Astron. Soc. **323**, 1 (2001).

[83] J. L. Tinker, B. E. Robertson, A. V. Kravtsov, A. Klypin, M. S. Warren *et al.*, Astrophys. J. **724**, 878 (2010).

[84] V. Springel, S. D. M. White, A. Jenkins, C. S. Frenk, N. Yoshida *et al.*, Nature (London) **435**, 629 (2005).

[85] M. Boylan-Kolchin, V. Springel, S. D. M. White, A. Jenkins, and G. Lemson, Mon. Not. R. Astron. Soc. **398**, 1150 (2009).

[86] K. Riebe, A. M. Partl, H. Enke, J. Forero-Romero, S. Gottloeber *et al.*, arXiv:1109.0003.

[87] R. E. Angulo, V. Springel, S. D. M. White, A. Jenkins, C. M. Baugh *et al.*, arXiv:1203.3216.

[88] J. Diemand, M. Kuhlen, and P. Madau, Astrophys. J. **657**, 262 (2007); **667**, 859 (2007); **679**, 1680 (2008).

[89] J. Stadel, D. Potter, B. Moore, J. Diemand, P. Madau *et al.*, Mon. Not. R. Astron. Soc. Lett. **398**, L21 (2009).

[90] J. E. Taylor and J. F. Navarro, Astrophys. J. **563**, 483 (2001).

[91] J. Binney and S. Tremaine, *Galactic Dynamics* (Princeton University Press, Princeton, NJ, 2008), 2nd ed., Ch. 4.8.1.

[92] W. Dehnen and D. McLaughlin, Mon. Not. R. Astron. Soc. **363**, 1057 (2005).

[93] R. J. Scherrer, private communication.

[94] M. White, Astrophys. J. Suppl. **143**, 241 (2002).

[95] J. S. Bullock, T. S. Kolatt, Y. Sigad, R. S. Somerville, A. V. Kravtsov *et al.*, Mon. Not. R. Astron. Soc. **321**, 559 (2001).

[96] A. F. Neto, L. Gao, P. Bett, S. Cole, J. F. Navarro *et al.*, Mon. Not. R. Astron. Soc. **381**, 1450 (2007).

[97] F. Prada, A. A. Klypin, A. J. Cuesta, J. E. Betancort-Rijo, and J. Primack, arXiv:1104.5130, submitted to Mon. Not. R. Astron. Soc.

[98] E. Bertschinger, Phys. Rev. D **74**, 063509 (2006); T. Bringmann, New J. Phys. **11**, 105027 (2009); J. Kasahara, Ph.D. thesis, University of Utah, 2009.

[99] D. Tseliakhovich and C. Hirata, Phys. Rev. D **82**, 083520 (2010).

[100] A. L. Erickcek and K. Sigurdson, Phys. Rev. D **84**, 083503 (2011).

[101] C. Giocoli, L. Pieri and G. Tormen, Mon. Not. R. Astron. Soc. **387**, 689 (2008); G. D. Martinez, J. S. Bullock, M. Kaplinghat, L. E. Strigari, and R. Trotta, J. Cosmol. Astropart. Phys. 06 (2009) 014; S. K. Lee, S. Ando, and M. Kamionkowski, *ibid.* 07 (2009) 007.

[102] N. Afshordi, R. Mohayaee, and E. Bertschinger, Phys. Rev. D **81**, 101301 (2010).

[103] U. Seljak, Mon. Not. R. Astron. Soc. **318**, 203 (2000).

[104] F. W. Stecker, M. A. Malkan, and S. T. Scully, Astrophys. J. **648**, 774 (2006); **658**, 1392 (2007).

[105] J. Hisano, S. Matsumoto, M. M. Nojiri, and O. Saito, Phys. Rev. D **71**, 063528 (2005); N. Arkani-Hamed, D. P. Finkbeiner, T. R. Slatyer, and N. Weiner, *ibid.* **79**, 015014 (2009); M. Lattanzi and J. I. Silk, *ibid.* **79**, 083523 (2009); J. D. March-Russell and S. M. West, Phys. Lett. B **676**, 133 (2009).

[106] R. Iengo, J. High Energy Phys. 05 (2009) 024.

[107] R. Iengo, arXiv:0903.0317; S. Cassel, J. Phys. G **37**, 105009 (2010).

[108] J. B. Dent, S. Dutta, and R. J. Scherrer, Phys. Lett. B **687**, 275 (2010); J. Zavala, M. Vogelsberger, and S. D. M. White, Phys. Rev. D **81**, 083502 (2010); J. L. Feng, M. Kaplinghat, and H.-B. Yu, *ibid.* **82**, 083525 (2010); A. Hryczuk, R. Iengo, and P. Ullio, J. High Energy Phys. 03 (2011) 069.

[109] M. Backovic and J. P. Ralston, Phys. Rev. D **81**, 056002 (2010).

[110] L. Hui, Phys. Rev. Lett. **86**, 3467 (2001).

[111] J. J. Sakurai, *Advanced Quantum Mechanics* (Addison-Wesley, Reading, MA, 1994), Ch. 7.8, rev. ed.; M. E. Peskin and D. V. Schroeder, *An Introduction to Quantum Field Theory* (Westview Press, Boulder, CO, 1995), pp. 101, 237; M. Ibe, H. Murayama, and T. T. Yanagida, Phys. Rev. D **79**, 095009 (2009).

[112] S. Kazantzidis, J. Magorrian, and B. Moore, Astrophys. J. **601**, 37 (2004); R. Wojtak, E. L. Lokas, S. Gottloeber, and G. A. Mamon, Mon. Not. R. Astron. Soc. **361**, L1 (2005); S. H. Hansen, B. Moore, M. Zemp, and J. Stadel, J. Cosmol. Astropart. Phys. 01 (2006) 014; M. Kuhlen, N. Weiner, J. Diemand, P. Madau, B. Moore *et al.*, *ibid.* 02 (2010) 030.

[113] J. A. Peacock, *Cosmological Physics* (Cambridge University Press, Cambridge, 1999).

[114] H. P. Nilles, Phys. Rept. **110**, 1 (1984).

[115] E. Witten, Nucl. Phys. **B188**, 513 (1981); S. Dimopoulos and H. Georgi, *ibid.* **193**, 150 (1981); N. Sakai, Z. Phys. C **11**, 153 (1981).

[116] U. Amaldi, W. de Boer, and H. Fürstenau, Phys. Lett. B **260**, 447 (1991); W. de Boer and C. Sander, *ibid.* **585**, 276 (2004).

[117] P. Fayet, Nucl. Phys. **B90**, 104 (1975).

[118] P. Gondolo and G. Gelmini, Nucl. Phys. **B360**, 145 (1991).

[119] A. H. Chamseddine, R. L. Arnowitt, and P. Nath, Phys. Rev. Lett. **49**, 970 (1982); R. Barbieri, S. Ferrara, and C. A. Savoy, Phys. Lett. B **119**, 343 (1982); L. J. Hall, J. D. Lykken, and S. Weinberg, Phys. Rev. D **27**, 2359 (1983); P. Nath, R. L. Arnowitt, and A. H. Chamseddine, Nucl. Phys. **B227**, 121 (1983).

[120] G. Aad, B. Abbott, J. Abdallah, A. A. Abdelalim, A. Abdesselam *et al.*(ATLAS Collaboration), J. High Energy Phys. 11 (2011) 099; Phys. Rev. D **85**, 012006 (2012).

[121] S. Chatrchyan, V. Khachatryan, A. M. Sirunyan, A. Tumasyan, W. Adam *et al.*(CMS Collaboration), J. High Energy Phys. 08 (2011) 156; Phys. Rev. Lett. **107**, 221804 (2011).

[122] S. Chatrchyan, V. Khachatryan, A. M. Sirunyan, A. Tumasyan, W. Adam *et al.*(CMS Collaboration), Phys. Lett. B **710**, 26 (2012); G. Aad, B. Abbott, J. Abdallah, S. Abdel Khalek, A. A. Abdelalim *et al.*(ATLAS Collaboration), *ibid.* **710**, 49 (2012); TEVNPH Working Group (CDF and D0 Collaborations), arXiv:1203.3774.

[123] K. Griest and D. Seckel, Phys. Rev. D **43**, 3191 (1991).

[124] K. L. Chan, U. Chattopadhyay, and P. Nath, Phys. Rev. D **58**, 096004 (1998); J. L. Feng, K. T. Matchev, and T. Moroi, Phys. Rev. Lett. **84**, 2322 (2000); Phys. Rev. D **61**, 075005 (2000); H. Baer, C. Chen, F. Paige, and X. Tata, *ibid.* **52**, 2746 (1995); **53**, 6241 (1996); H. Baer, C. Chen, M. Drees, F. Paige, and X. Tata, *ibid.* **59**, 055014 (1999).

[125] J. R. Ellis, T. Falk, and K. A. Olive, Phys. Lett. B **444**, 367 (1998); J. R. Ellis, T. Falk, K. A. Olive, and M. Srednicki, Astropart. Phys. **13**, 181 (2000); **15**, 413 (2001); M. E. Gomez, G. Lazarides, and C. Pallis, Phys. Rev. D **61**, 123512 (2000); Phys. Lett. B **487**, 313 (2000); A. B. Lahanas, D. V. Nanopoulos, and V. C. Spanos, Phys. Rev. D **62**, 023515 (2000); R. L. Arnowitt, B. Dutta, and Y. Santoso, Nucl. Phys. **B606**, 59 (2001).

[126] J. R. Ellis, K. A. Olive, and Y. Santoso, Astropart. Phys. **18**, 395 (2003).

[127] M. Drees and M. M. Nojiri, Phys. Rev. D **47**, 376 (1993); N. F. Bell, J. B. Dent, T. D. Jacques, and T. J. Weiler, Phys. Rev. D **83**, 013001 (2011).

[128] H. Baer and M. Brhlik, Phys. Rev. D **57**, 567 (1998); H. Baer, M. Brhlik, M. A. Diaz, J. Ferrandis, P. Mercadante *et al.*, *ibid.* **63**, 015007 (2000); J. R. Ellis, T. Falk, G. Ganis, K. A. Olive, and M. Srednicki, Phys. Lett. B **510**, 236 (2001); L. Roszkowski, R. Ruiz de Austri, and T. Nihei, J. High Energy Phys. 08 (2001) 024; A. Djouadi, M. Drees, and J. L. Kneur, *ibid.* 08 (2001) 055; A. B. Lahanas and V. C. Spanos, Eur. Phys. J. C **23**, 185 (2002).

[129] R. N. Mohapatra and R. Marshak, Phys. Rev. Lett. **44**, 1316 (1980); **44**, 1644(E) (1980).

[130] P. Minkowski, Phys. Lett. B **67**, 421 (1977); T. Yanagida, in *Workshop on Unified Theories (1979)*, p. 95, KEK Report 79-18; M. Gell-Mann, P. Ramond, and R. Slansky, in *Supergravity*, edited by P. van Niewenhuizen and D. Freedman (North Holland, Amsterdam, 1979), p. 315; S. L. Glashow, in *1979 Cargese Summer Institute on Quarks and Leptons* (Plenum, New York, 1980), p. 687; R. N. Mohapatra and G. Senjanovic, Phys. Rev. Lett. **44**, 912 (1980).

[131] R. Allahverdi, B. Dutta, K. Richardson-McDaniel, and Y. Santoso, Phys. Lett. B **677**, 172 (2009); Phys. Rev. D **79**, 075005 (2009); R. Allahverdi, S. Bornhauser, B. Dutta, and K. Richardson-McDaniel, *ibid.* **80**, 055026 (2009).

[132] P. Gondolo, J. Edsjö, P. Ullio, L. Bergström, M. Schelke *et al.*, J. Cosmol. Astropart. Phys. 07 (2004) 008.

[133] F. E. Paige, S. D. Protopopescu, H. Baer, and X. Tata, arXiv:hep-ph/0312045.

[134] T. Hahn, S. Heinemeyer, W. Hollik, H. Rzehak, and G. Weiglein, Comput. Phys. Commun. **180**, 1426 (2009).

[135] L. Bergstrom and P. Ullio, Nucl. Phys. **B504**, 27 (1997).

[136] T. Sjostrand, S. Mrenna, and P. Z. Skands, Comput. Phys. Commun. **178**, 852 (2008).

[137] A. Klypin, H. Zhao, and R. S. Somerville, Astrophys. J. **573**, 597 (2002).

[138] A. A. Abdo, M. Ackermann, M. Ajello, W. B. Atwood, L. Baldini *et al.*(Fermi-LAT Collaboration), Phys. Rev. Lett. **104**, 101101 (2010).

[139] R. Gandhi, C. Quigg, M. H. Reno, and I. Sarcevic, Phys. Rev. D **58**, 093009 (1998); Y. S. Jeong and M. H. Reno, *ibid.* **82**, 033010 (2010).

[140] M. Honda, T. Kajita, K. Kasahara, S. Midorikawa, and T. Sanuki, Phys. Rev. D **75**, 043006 (2007); M. Honda, T. Kajita, K. Kasahara, and S. Midorikawa, *ibid.* **83**, 123001 (2011).

[141] R. Piessens, E. de Doncker-Kapenga, and C. W. Ueberhuber, *Quadpack: a subroutine package for automatic integration* (Springer-Verlag, Berlin, 1983).

[142] W. H. Press, S. A. Teukolsky, W. T. Vetterling, and B. P. Flannery, *Numerical Recipes: The Art of Scientific Computing* (Cambridge University Press, Cambridge, England, 2007), 3rd ed., Chap. 6.8.

# APPENDIX A
# ALGORITHMS FOR NUMERICAL EVALUATION OF NFW FOURIER TRANSFORMS*

Although there exist some very good general integrators for Fourier transforms [141], their use is not feasible in this calculation. The transforms appear in the integrand of the halo mass integration, and that result is then integrated over redshift. The number of evaluations required for precise calculation is very large, and takes too long to complete when using a general-purpose integrator. Since these functions are over a 3-dimensional space $(k|M, z)$ that stretches over a large range of scales, it is also not feasible to fill a data table for interpolation.

For the rigid NFW profile, a closed form solution is available for $\mathcal{FT}\{\rho_h^2\}$, which has allowed efficient calculation of s-wave angular power spectra in previous works. No such closed form is available for the non-analytic $\mathcal{FT}\{\rho_h^2\sigma_{uh}^2\}$. Nevertheless, I was successful in developing a numerical algorithm for efficient evaluation of this function, as described below. One of the challenges for calculations of angular power spectra of extragalactic dark matter annihilation products is the development of efficient numerical methods to evaluate $\mathcal{FT}\{\rho_h^2[\overline{\sigma v}]_h\}$ for a given model's halo profiles and annihilation cross section. This calculation would have taken weeks to complete using the quadpack general purpose Fourier transform integrator, qawf. With the algorithm described in this section, the results in this paper were evaluated within a few days of run time on a desktop computer.

---

## A.1 $\mathcal{FT}\{\rho_h^2\}(k|M,z)$

This Fourier transform can be expressed as

$$\begin{aligned}\mathcal{FT}\{\rho_h^2\}(k) = 4\pi\rho_s^2 r_s^3 \Bigg\{ & -\frac{2}{3} + \frac{4+3c}{6(1+c)^2}\cos(kr_s c) \\ & + \frac{11+15c+6c^2-[(1+c)kr_s]^2}{6kr_s(1+c)^3}\sin(kr_s c) + \frac{\mathrm{Si}(kr_s c)}{kr_s} \\ & - \begin{pmatrix} 1-\frac{(kr_s)^2}{6} & \frac{1}{kr_s}-\frac{kr_s}{2} \end{pmatrix} \begin{pmatrix} \cos(kr_s) & \sin(kr_s) \\ -\sin(kr_s) & \cos(kr_s) \end{pmatrix} \begin{pmatrix} \mathrm{Ci}\big(kr_s(1+c)\big) - \mathrm{Ci}(kr_s) \\ \mathrm{Si}\big(kr_s(1+c)\big) - \mathrm{Si}(kr_s) \end{pmatrix} \Bigg\}\end{aligned} \tag{A.1}$$

where Si and Ci are the sine integral and cosine integral, respectively, for which efficient numerical methods for evaluation already exist [142]. Evaluating the line-of-sight integrand for the angular power spectrum near $z = 0$ requires the Fourier transform to be evaluated in the $k \to \infty$ regime. One finds that for $kr_s \gg 1$,

$$\mathcal{FT}\{\rho_h^2\}(k) = 2\pi r_s^3 \rho_s^2 \left\{ \frac{\pi}{kr_s} - \frac{1}{(kr_s)^2}\left[8 + \frac{2}{c(1+c)^4}\cos(kr_s c)\right] + \mathcal{O}\left((kr_s)^{-3}\right)\right\}.$$

Unfortunately, in the Bullock, et al. model of halo concentrations, the mean halo concentration vanishes at a maximum halo mass scale. Staying true to the definition of the model requires evaluating the transform in the vanishing concentration regime. Here, one should use

$$\begin{aligned}(r_s\rho_s)^2 &= \left(\frac{\Delta_{\mathrm{vir}}\langle\rho\rangle R_{\mathrm{vir}}}{3}\right)^2 \frac{c^4}{\left[\ln(1+c) - \frac{c}{1+c}\right]^2} \\ &= \left(\frac{\Delta_{\mathrm{vir}}\langle\rho\rangle R_{\mathrm{vir}}}{3}\right)^2 \left[4 + \frac{32}{3}c + \frac{28}{3}c^2 + \mathcal{O}(c^3)\right].\end{aligned}$$

If $c \ll 1$ and $c \ll kR_{\mathrm{vir}}$ (equivalently, $kr_s \gg 1$), then

$$\begin{aligned}k\,\mathcal{FT}\{\rho_h^2\}(k) = 4\pi(r_s\rho_s)^2 \Bigg\{ & \mathrm{Si}(kR_{\mathrm{vir}}) - 2\Big[1-\cos(kR_{\mathrm{vir}})\Big]\frac{c}{kR_{\mathrm{vir}}} \\ & + 3\Big[\sin(kR_{\mathrm{vir}}) - kR_{\mathrm{vir}}\cos(kR_{\mathrm{vir}})\Big]\left(\frac{c}{kR_{\mathrm{vir}}}\right)^2 + \mathcal{O}(c^3) + \mathcal{O}\left(\left(\frac{c}{kR_{\mathrm{vir}}}\right)^3\right)\Bigg\}.\end{aligned}$$

In the case where $c \ll 1$ and $c \ll kR_{\rm vir}$, then it must be that $kR_{\rm vir} \ll 1$, and one can use

$$k\ \mathcal{FT}\{\rho_h^2\}(k) = 4\pi(r_s\rho_s)^2 \frac{kR_{\rm vir}}{c}\left[\frac{1}{3}\left(1-\frac{1}{(1+c)^3}\right) - \frac{c}{18(1+c)}\left(kR_{\rm vir}\right)^2 + \mathcal{O}\left(\left(kR_{\rm vir}\right)^4\right)\right].$$

## A.2 $\mathcal{FT}\{\rho_h^2\sigma_{uh}^2\}(k|M,z)$

This Fourier transform is simply expressed in the form

$$\mathcal{FT}\{\rho_h^2\sigma_{uh}^2\}(k) = \frac{4\pi r_s^2\rho_s^2\sigma_s^2}{k}\mathcal{S}(kR_{\rm vir}, c) \tag{A.2}$$

with the definition

$$\mathcal{S}(x,c) \equiv \int_0^c \frac{\sin\left(\frac{x}{c}t\right)}{t^{1-\beta}(1+t)^q}\mathrm{d}t, \tag{A.3}$$

where $\beta = 17/27$, as previously defined in (2.124), and $q = 16/3$ for the NFW profile. The important result that allows efficient evaluation of $\mathcal{S}(x,c)$ for a wide range of scales for $x$ and $c$ is the set of expansions (see Appendix A.3)

$$\mathcal{S}(x,c) = \begin{cases} \dfrac{c^\beta}{(1+c)^q}\displaystyle\sum_{p=0}^{\infty}\frac{(q)_p}{(\beta)_{p+1}}\Im\Big[{}_1F_1(\beta;\beta+p+1;ix)\Big]\left(\dfrac{c}{1+c}\right)^p, & c \le c_T \\ -\dfrac{c^\beta}{(1+c)^q}\displaystyle\sum_{p=0}^{\infty}(q)_p\Im\Big[e^{ix}U(p+1,\beta-q+1,-ix)\Big]\left(\dfrac{1}{1+c}\right)^p & \\ \quad +\Gamma(\beta)\Im\Big[U\Big(\beta,\beta-q+1,-i\dfrac{x}{c}\Big)\Big], & c > c_T \end{cases} \tag{A.4}$$

where $c_T$ is an appropriate transition concentration. The truncation errors of the two expressions were found to be of the same magnitude near $c = 0.8$, making it a reasonable value for $c_T$. Also in the expression appears the gamma function $\Gamma(x)$, the Pochhammer symbol

$$(q)_p \equiv \frac{\Gamma(q+p)}{\Gamma(q)} = q(q+1)(q+2)\cdots(q+p-1),$$

the confluent hypergeometric function of the first kind ${}_1F_1(a;b;z)$ (expressed in the notation of a generalized hypergeometric function), and the confluent hypergeometric function of the second kind $U(a,b,z)$.

For $c < c_T$, if $x$ is small, then the hypergeometric functions are most efficiently evaluated with their power series

$$\Im\Big[{}_1F_1(\beta;\beta+p+1;ix)\Big] = \sum_{n=0}^{\infty} \frac{(-1)^n(\beta)_{2n+1}}{(\beta+p+1)_{2n+1}} \frac{x^{2n+1}}{(2n+1)!}.$$

This is found to work for $x \lesssim 4$. For larger values of $x$, the functions are quickly determined from the recurrence relation

$$\begin{aligned} {}_1F_1(\beta;\beta+p+1;ix) =& \frac{\beta+p}{p}\left[\left(1 - i\frac{\beta+p-1}{x}\right){}_1F_1(\beta;\beta+p;ix)\right. \\ &\left. + i\frac{\beta+p-1}{x}{}_1F_1(\beta;\beta+p-1;ix)\right], \end{aligned}$$

or

$$\begin{aligned} \Re\Big[{}_1F_1(\beta;\beta+p+1;ix)\Big] =& \frac{\beta+p}{p}\left\{\Re\Big[{}_1F_1(\beta;\beta+p;ix)\Big]\right. \\ &\left. + \frac{\beta+p+1}{x}\Im\Big[{}_1F_1(\beta;\beta+p;ix) - {}_1F_1(\beta;\beta+p-1;ix)\Big]\right\}, \\ \Im\Big[{}_1F_1(\beta;\beta+p+1;ix)\Big] =& \frac{\beta+p}{p}\left\{\Im\Big[{}_1F_1(\beta;\beta+p;ix)\Big]\right. \\ &\left. - \frac{\beta+p+1}{x}\Re\Big[{}_1F_1(\beta;\beta+p;ix) - {}_1F_1(\beta;\beta+p-1;ix)\Big]\right\}. \end{aligned}$$

Since ${}_1F_1(\beta;\beta;ix) = e^{ix}$, then only the numerical evaluation of ${}_1F_1(\beta;\beta+1;ix)$ is needed to be able to determine the rest of the sum's hypergeometric functions using the recurrence relation. The power series is suitable for $x \lesssim 10$:

$${}_1F_1(\beta;\beta+1;ix) = \sum_{n=0}^{\infty} \frac{\beta}{\beta+n}\frac{(ix)^n}{n!}.$$

The asymptotic expansion converges appropriately for $x \gtrsim 27$:

$$ {}_1F_1(\beta;\beta{+}1;ix) \simeq \Gamma(\beta{+}1)\exp\left(i\frac{\beta\pi}{2}\right)x^{-\beta}{+}\beta\sum_{n=1,2,3,\ldots}(n{-}\beta)_{n-1}\exp\left[i\left(x-\frac{n\pi}{2}\right)\right]x^{-n}. $$

For $10 \lesssim x \lesssim 27$, these series' do not converge sufficiently with double machine precision arithmetic. For this short range of $x$, it is not too much of a burden to evaluate the function via numerical integration

$$ {}_1F_1(\beta;\beta+1;ix) = \beta\int_0^1 e^{ixt}t^{\beta-1}\mathrm{d}t. $$

For large concentrations $c > c_T$, there are two components. The first term depends only on the ratio $\bar{x} \equiv x/c$ and requires the evaluation of $\Im[U(\beta,\beta-q+1,-i\bar{x})]$. We can use the perturbative expansion for $\bar{x} \leq 5$, for which a convenient expression is

$$ \begin{aligned}\Im[U(\beta,\beta-q+1,-i\bar{x})] = &\sum_{n=0}^{\infty}\left[(-1)^{(n+1)/2}(n \bmod 2)\frac{\Gamma(q-\beta)}{\Gamma(q)}\frac{(\beta)_n}{(\beta-q+1)_n}\right.\\ &\left.+\frac{\pi}{2\Gamma(\beta)\Gamma(q-\beta+1)}\frac{(-1)^{\lfloor n/2\rfloor}}{\mathcal{CS}_n\left(\frac{\pi(q-\beta)}{2}\right)}\frac{(q)_n}{(q-\beta+1)_n}\bar{x}^{q-\beta}\right]\frac{\bar{x}^n}{n!},\end{aligned} $$

Introduced in this expansion is the modulo 2 operation

$$ n \bmod 2 = \begin{cases}0, & n \text{ even},\\ 1, & n \text{ odd},\end{cases} $$

the floor operation $\lfloor x \rfloor$ being the largest integer $\leq x$, and a trigonometric function defined as

$$ \mathcal{CS}_n(x) \equiv \begin{cases}\cos x, & n \text{ even},\\ \sin x, & n \text{ odd}.\end{cases} $$

The asymptotic expansion

$$ \Im[U(\beta,\beta-q+1,-i\bar{x})] \simeq \bar{x}^{-\beta}\sum_{n=0,1,2,\ldots}(-1)^{\lfloor 3n/2\rfloor}\mathcal{CS}_{n+1}\left(\frac{\beta\pi}{2}\right)(\beta)_n(q)_n\frac{\bar{x}^{-n}}{n!} $$

works sufficiently for $\bar{x} \geq 40$. For the little remaining range of $5 < \bar{x} < 40$, the integral representation was evaluated numerically.

$$\Gamma(\beta)\Im[U(\beta, \beta - q + 1, -i\bar{x})] = \int_0^\infty \frac{\sin(\bar{x}t)}{t^{1-\beta}(1+t)^q} \mathrm{d}t$$

To evaluate the functions

$$\begin{aligned}\Im\Big[e^{ix}U(p+1, \beta - q + 1, -ix)\Big] =& \sin x \ \Re\Big[U(p+1, \beta - q + 1, -ix)\Big] \\ &+ \cos x \ \Im\Big[U(p+1, \beta - q + 1, -ix)\Big]\end{aligned}$$

occuring in the sum, recursion relations can be used again.

$$\begin{aligned}\Re\Big[U(p+1, \beta - q + 1, -ix)\Big] &= \frac{1}{p(p+q-\beta)} \Big\{x\Im\Big[U(p, \beta - q + 1, -ix)\Big] \\ &\quad +(2p+q-\beta-1)\Re\Big[U(p, \beta - q + 1, -ix)\Big] - \Re\Big[U(p-1, \beta - q + 1, -ix)\Big]\Big\} \\ \Im\Big[U(p+1, \beta - q + 1, -ix)\Big] &= \frac{1}{p(p+q-\beta)} \Big\{-x\Re\Big[U(p, \beta - q + 1, -ix)\Big] \\ &\quad +(2p+q-\beta-1)\Im\Big[U(p, \beta - q + 1, -ix)\Big] - \Im\Big[U(p-1, \beta - q + 1, -ix)\Big]\Big\}\end{aligned}$$

Since $U(0, \cdot, \cdot) = 1$, we require only the evaluation of $U(1, \beta - q + 1, -ix)$. For $x \leq 4$,

$$\begin{aligned}&U(1, \beta - q + 1, -ix) \\ &\quad = \frac{1}{q-\beta} \sum_{n=0}^{\infty} \left[ \frac{(-1)^{n/2}(1 - n \bmod 2)}{(\beta - q + 1)_n} - \frac{\pi x^{q-\beta}}{2\Gamma(q-\beta)} \frac{(-1)^{\lfloor (n+1)/2 \rfloor}}{n! \mathcal{CS}_{n+1}\Big(\frac{\pi(q-\beta)}{2}\Big)} \right] x^n \\ &\qquad + \frac{i}{q-\beta} \sum_{n=0}^{\infty} \left[ \frac{(-1)^{(n+1)/2}(n \bmod 2)}{(\beta - q + 1)_n} - \frac{\pi x^{q-\beta}}{2\Gamma(q-\beta)} \frac{(-1)^{\lfloor n/2 \rfloor}}{n! \mathcal{CS}_{n}\Big(\frac{\pi(q-\beta)}{2}\Big)} \right] x^n\end{aligned}$$

was used, and for $x \geq 45$,

$$U(1, \beta - q + 1, -ix) \simeq - \sum_{n=0,1,2,\ldots} (q - \beta + 1)_n (ix)^{-(n+1)}$$

was evaluated. For the mid-values of $x$, the integral representation was numerically

calculated

$$U(1,\beta-q+1,-ix)=\int_0^\infty \frac{e^{ixt}}{(1+t)^{q-\beta+1}}\mathrm{d}t.$$

For very large values of $x$, the recursion relations will fail because of loss of precision, due to subtracted quantities being very near each other. In this regime, the hypergeometric function in each term of the sum can be evaluated from the asymptotic series

$$\Im\Big[e^{ix}U(p+1,\beta-q+1,-ix)\Big] \simeq \sum_{n=0,1,2,\ldots}(-1)^{\lfloor(n-p)/2\rfloor}\mathcal{CS}_{n+p}(x)(p+1)_n(q-\beta+p+1)_n\frac{x^{-(n+p+1)}}{n!}.$$

## A.3 Derivation of Equation (A.4)

Let's begin with the case of $c<c_T=0.8$ by expanding $(1+t)^{-q}$ in Equation (A.3) as a power series, and rescaling $t\longrightarrow xt/c$ to get

$$\mathcal{S}(x,c)=\sum_{m=0}^{\infty}(-1)^m\frac{\Gamma(q+m)}{\Gamma(q)m!}\frac{I_{\beta+m-1}(x)}{x^{\beta+m}}c^{\beta+m},$$

where

$$I_n(x)\equiv\int_0^x t^n\sin t\ \mathrm{d}t.$$

Letting $\kappa=c/(1+c)$, we can write the expression in the form

$$\mathcal{S}(x,c)=\frac{c^\beta}{(1+c)^q}\sum_{m=0}^{\infty}(-1)^m\frac{\Gamma(q+m)}{\Gamma(q)m!}\frac{I_{\beta+m-1}(x)}{x^{\beta+m}}\frac{\kappa^m}{(1-\kappa)^{q+m}},$$

and expand the $\kappa$ expression in a power series with shifted indices

$$(1-\kappa)^{-(q+m)}=\sum_{p=0}^{\infty}\frac{\Gamma(q+m+p)}{\Gamma(q+m)p!}\kappa^p=\sum_{p=m}^{\infty}\frac{\Gamma(q+p)}{\Gamma(q+m)(p-m)!}\kappa^{p-m}.$$

Swap the order of summation to find

$$\mathcal{S}(x,c) = \frac{c^\beta}{(1+c)^q} \sum_{p=0}^{\infty} \frac{\Gamma(q+p)}{\Gamma(q)} \left[ \sum_{m=0}^{p} \frac{(-1)^m}{m!(p-m)!} \frac{I_{\beta+m-1}(x)}{x^{\beta+m}} \right] \left( \frac{c}{1+c} \right)^p$$

after substituting $c$ back into $\kappa$. The quantity in the square brackets can be rewritten using the integral representation of the confluent hypergeometric function

$${}_1F_1(a;b;z) = \frac{\Gamma(b)}{\Gamma(a)\Gamma(b-a)} \int_0^1 e^{zt} t^{a-1} (1-t)^{b-a-1} \mathrm{d}t$$

(convergent for $\Re(b) > \Re(a) > 0$), giving

$$\begin{aligned}
\sum_{m=0}^{p} \frac{(-1)^m}{m!(p-m)!} \frac{I_{\beta+m-1}(x)}{x^{\beta+m}} &= \frac{1}{p!} \sum_{m=0}^{p} (-1)^m \binom{p}{m} x^{-(\beta+m)} \int_0^x t^{\beta+m-1} \sin t \; \mathrm{d}t \\
&= \frac{1}{p!} \int_0^1 t^{\beta-1} \left[ \sum_{m=0}^{p} \binom{p}{m} (-t)^m \right] \sin(xt) \; \mathrm{d}t \\
&= \frac{1}{p!} \Im \left[ \int_0^1 t^{\beta-1} (1-t)^p e^{ixt} \mathrm{d}t \right] \\
&= \frac{\Gamma(\beta)}{\Gamma(\beta+p+1)} \Im \Big[ {}_1F_1(\beta; \beta+p+1; ix) \Big]
\end{aligned}$$

where the second line rescaled $t \longrightarrow t/x$.

For the case of large concentrations $c > c_T$, split $\mathcal{S}$ into two terms

$$\mathcal{S}(x,c) = \mathcal{S}_1\Big(\frac{x}{c}\Big) - \mathcal{S}_2(x,c)$$

with

$$\begin{aligned}
\mathcal{S}_1(\bar{x}) &= \int_0^\infty \frac{\sin(\bar{x}t)}{t^{1-\beta}(1+t)^q} \mathrm{d}t, \\
\mathcal{S}_2(x,c) &= \int_c^\infty \frac{\sin\left(\frac{x}{c}t\right)}{t^{1-\beta}(1+t)^q} \mathrm{d}t.
\end{aligned}$$

The first term is

$$\mathcal{S}_1(\bar{x}) = \Im\left[\int_0^\infty \frac{e^{i\bar{x}t}}{t^{1-\beta}(1+t)^q}\mathrm{d}t\right] = \Gamma(\beta)\Im\Big[U(\beta,\beta-q+1,-i\bar{x})\Big],$$

given that the confluent hypergeometric function of the second kind has the integral representation

$$U(a,b,z) = \frac{1}{\Gamma(a)}\int_0^\infty e^{-zt}t^{a-1}(1+t)^{b-a-1}\mathrm{d}t$$

if $\Re(a) > 0$ and $\Re(z) > 0$. For the second term, first substitute $t \longrightarrow t - c$

$$\begin{aligned}\mathcal{S}_2(x,c) &= \int_0^\infty \frac{\sin\left(\frac{x}{c}(c+t)\right)}{(c+t)^{1-\beta}(1+c+t)^q}\mathrm{d}t \\ &= \frac{c^\beta}{(1+c)^q}\int_0^\infty \frac{\sin\left[x\left(1+\frac{t}{c}\right)\right]}{\left(1+\frac{t}{c}\right)^{1-\beta}\left(1+\frac{t}{1+c}\right)^q}\frac{\mathrm{d}t}{c},\end{aligned}$$

and then substitute $t \longrightarrow t/c$

$$\mathcal{S}_2(x,c) = \frac{c^\beta}{(1+c)^q}\,\Im\left[e^{ix}\int_0^\infty \frac{e^{ixt}}{(1+t)^{1-\beta}(1+\kappa t)^q}\mathrm{d}t\right]$$

with $\kappa = c/(1+c)$, as before. As is appropriate for large values of $c$, expand as a power series about $\kappa = 1$.

$$\begin{aligned}\mathcal{S}_2(x,c) &= \frac{c^\beta}{(1+c)^q}\sum_{p=0}^\infty \frac{\Gamma(q+p)}{\Gamma(q)}\Im\Big[e^{ix}\int_0^\infty e^{ixt}t^p(1+t)^{\beta-q-p-1}\mathrm{d}t\Big]\frac{(1-\kappa)^p}{p!} \\ &= \frac{c^\beta}{(1+c)^q}\sum_{p=0}^\infty \frac{\Gamma(q+p)}{\Gamma(q)}\Im\Big[e^{ix}U(p+1,\beta-q+1,-ix)\Big]\left(\frac{1}{1+c}\right)^p\end{aligned}$$

# APPENDIX B

# CALCULATING GALACTIC ANNIHILATIONS SIGNALS FROM AN NFW HALO CORE*

While the density cusp at the center of dark matter halos in the NFW model causes the observed dark matter annihilation intensity to be infinite in the direction toward the center of the halo, mean intensities over solid angles including the center are finite. Baryon cooling and, in larger halos, the presence of a supermassive black hole are some of the important effects that ultimately generate a more realistic core profile. To keep the dark matter distribution in the sample calculations relatively simple, no attempt was made to model these effects. The NFW profile was simply assumed throughout the halo.

In this appendix, I explain my method for accurate calculation of annihilation intensity averages $\overline{I}(\psi_M)$ from observations over solid angles centered on the galactic center, with angular radius $\psi_M$. Referring to Equations (6.1)–(6.3), the goal is to evaluate

$$\overline{I}(E_\gamma, \psi_M) = \frac{\sigma v}{8\pi m^2} \frac{\mathrm{d}N_\gamma}{\mathrm{d}E_\gamma}(E_\gamma)\overline{J}(\psi_M)$$

with

$$\overline{J}(\psi_M) = \frac{1}{1-\cos\psi_M} \int_0^{\psi_M} \mathrm{d}\psi \sin\psi J(\psi).$$

Let $x$ be the distance from the solar system, in units of the galactic halo scale radius $r_{s,G}$, along a line of sight at angle $\psi$ from the galactic center, and let $x_\odot$ be the distance of the solar system from the galactic center, also in units of $r_{s,G}$. Then

$$\frac{1-\cos\psi_M}{\rho_{s,G}^2 r_{s,G}} \overline{J}(\psi_M) = \int_0^{\psi_M} \mathrm{d}\psi \sin\psi \int_0^{x_{\max}(\psi)} \mathrm{d}x \left(x^2 - 2x_\odot x\cos\psi + x_\odot^2\right)^{-1} \times \left(1 + \sqrt{x^2 - 2x_\odot x\cos\psi + x_\odot^2}\right)^{-4},$$

*This appendix is reprinted with permission from "*Extragalactic and Galactic Gamma Rays and Neutrinos From Annihilating Dark Matter*" by R. Allahverdi, S. Campbell, and B. Dutta, Phys. Rev. D **85**, 035004 (2012), Copyright 2012 by The American Physical Society.

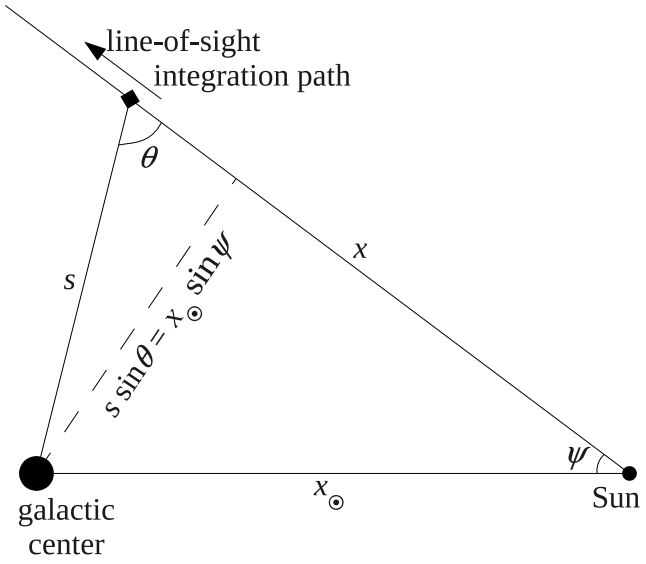


Figure 27: Galactic coordinates used for calculating the mean intensity due to dark matter annihilation in the smooth component of the galactic halo.

where

$$x_{\max}(\psi) = x_\odot \cos\psi + \sqrt{c_G^2 - (x_\odot \sin\psi)^2}$$

expresses the halo boundary and, as before, the halo concentration is $c_G = R_{\mathrm{vir},G}/r_{s,G}$. The integrand of $\overline{J}$ in these coordinates is irregular in the neighborhood of $\psi = 0$ and $x = x_\odot$, precisely where the modeled density diverges at the halo center.

The accurate evaluation of this expression is more easily attained when $x$ is replaced in favor of $\theta$, as pictured in Fig. 27.

$$\sin\theta = \frac{x_\odot \sin\psi}{s} = \frac{x_\odot \sin\psi}{\sqrt{(x - x_\odot\cos\psi)^2 + x_\odot^2 \sin^2\psi}}$$

In these coordinates,

$$\frac{1-\cos\psi_M}{\rho_{s,G}^2 r_{s,G}}\overline{J}(\psi_M) = \frac{1}{x_\odot}\int_0^{\psi_M} \mathrm{d}\psi \int_{\theta_M(\psi)}^{\pi-\psi} \mathrm{d}\theta \left(\frac{\sin\theta}{\sin\theta + x_\odot \sin\psi}\right)^4,$$

where

$$\theta_M(\psi) = \sin^{-1}\left(\frac{x_\odot}{c_G}\sin\psi\right).$$

The inner $\theta$ integration is now well defined and easy to evaluate numerically, except for when $\psi = 0$, where the $\theta$ path of integration becomes degenerate, initially at the Sun having the value of $\pi$, and instantaneously becoming 0 when crossing the galactic center. Since this degenerate point is an end of the $\psi$ integration, it is sufficient for numerical evaluation to consider the value of the inner integration in the limit as $\psi$ approaches 0.

For $\psi \longrightarrow 0$, we have $\theta_M \longrightarrow x_\odot\psi/c_G \longrightarrow 0$, and the inner integral approaches

$$\int_{\theta_M(\psi)}^{\pi-\psi} \mathrm{d}\theta \left(\frac{\sin\theta}{\sin\theta + x_\odot\psi}\right)^4 \longrightarrow \int_0^{\pi} \mathrm{d}\theta = \pi.$$

For $\psi = \pi$, the $\theta$ integration path is simply of zero measure with $\theta = 0$ constant along the path. Therefore, the inner integration vanishes for this value of $\psi$.

# VITA

Name: Sheldon Scott Campbell

Address:
c/o Bhaskar Dutta
Department of Physics
Texas A&M University
4242 TAMU
College Station, TX 77843-4242

Education:
B.S. with Honors, Mathematical Physics,
University of Alberta, 2001
M.S., Physics, University of Alberta, 2003
Ph.D., Physics, Texas A&M University, 2012